

University of Tokyo
Graduate School of Science
Department of Physics

**Impact of Reionization History on
Constraining Primordial Gravitational Waves
with Cosmic Microwave Background B-modes
(宇宙マイクロ波背景放射のBモード偏光を用いた
原始重力波の制限における宇宙再電離の影響)**

Hanchun Jiang

A thesis submitted to
the graduate school of science,
the University of Tokyo
in partial fulfillment of
the requirements for the degree
of
Master of Science in Physics

July 2024

Abstract

Primordial gravitational waves (PGWs) predicted by cosmic inflation remain unconfirmed by observations. Detecting B-modes from PGWs is a primary objective of current and future cosmic microwave background (CMB) experiments. The B-mode power spectrum from PGWs depends not only on the tensor-to-scalar ratio (r) but also on the reionization history. Reionization, the epoch when the first stars and galaxies ionized the intergalactic medium (IGM), significantly influences the CMB polarization. During reionization, the scattering of CMB photons by free electrons generates the reionization bump in both EE and BB power spectra, which is focused on by the next-generation observation. The precise modeling of reionization history is crucial for accurately constraining r , which decides the amplitude of B mode and is related to the energy scale of inflation. Variations in reionization models affect the amplitude and shape of the CMB power spectra, introducing uncertainties in the measurement of r . Understanding these impacts is essential for refining cosmological models and improving the detection of PGWs.

In this study, To assess the impact of reionization history on r , we employed various fiducial reionization models: exponential reionization model (characterized by a smooth, gradual increase in ionization), double reionization model (involves two distinct phases of ionization, leading to a more complex reionization history), and random reionization models (Generated by varying parameters randomly to simulate a range of possible reionization scenarios). We calculated the resulting CMB E- and B-mode signals for each model, analyzing how deviations from the true reionization history affect the constraints on r . We use the tanh reionization model (characterized by a smooth but fast increase in ionization) as a theory model to calculate the posterior distribution of r and the reionization parameter.

Our analysis reveals that inaccuracies in the reionization model can lead to a non-negligible bias in the estimated value of r . Specifically, random reionization histories tend to introduce more considerable uncertainties when r is small and the optical depth is high. This effect complicates the detection of PGWs, as it becomes more challenging to distinguish the primordial B-mode signal from the noise introduced by incorrect reionization modeling.

Acknowledgements

This thesis would not have been possible without the support and guidance of many individuals, to whom I am deeply grateful.

I would like to first express my sincere gratitude to my supervisor, Prof. Naoki Yoshida, for your continuous guidance and support during the whole course of my Master's program. Your unwavering support, insightful feedback, and patience have been instrumental in shaping this research. Your mentorship has been a source of inspiration, and I am deeply grateful for the opportunities you have provided me. Dr. Toshiya Namikawa, my primary collaborator, has tolerated my stupid questions and naive thoughts for a long time and taught me almost everything about my current research topic both from the side of theory and calculation. Your constant assistance has been invaluable.

I am also indebted to the members of my dissertation committee: Prof. Naoki Yoshida, Prof. Masahiro Kawasaki, and Prof. Tomotake Matsumura. Your critical insights, constructive criticisms, and encouragement have significantly contributed to the quality and direction of this work. Thank you for your time, expertise, and for pushing me to achieve my best.

Special thanks to my colleagues and friends at UTAP and RESCEU. Your camaraderie, collaborative spirit, and intellectual discussions have enriched my academic experience. I would like to particularly acknowledge Dr. Tilman Hartwig for your invaluable support and guidance in academia and life. Words alone cannot convey my gratitude for your support. I also want to thank Prof. Kazumi Kashiyama, Dr. Masataka Aizawa, and Dr. Kana Moriwaki, for patiently teaching me scientific and technical knowledge. I am grateful to Yuka Yamada, for the fruitful discussion in Zemi on cosmology and the enjoyment you bring; Ruilan Zhang, for patiently teaching me sports and encouraging me to join activities; Yurina Nakazato, for deeply discussing various topics and sharing the same interest with the anime characters; Yici Zhong, for providing me invaluable information; Bartosz Dzieciol and Hiroki Kawai, for telling me interesting stories; Soichiro Yamazaki, for greatly helping me about the life in Tokyo as my tutor; Yuting Liu, for the delicious food you cook; Yuting Lu, for the tours together with you. Thanks to all (ex-)UTAP members for the unforgettable lunches and parties, without you, I could not have improved my poor English so quickly or gotten used to life here.

I am profoundly grateful to my family for their unconditional love and support. To my parents,

thank you for your sacrifices, encouragement, and for believing in me. I also want to thank my friends here (Xinyi Xiao, Yuxiang Mao, etc.) and friends in IPMU and ICRR for lots of dinners together. Especially, I want to thank my boyfriend for the companionship online, and my friend Ruolin Wang for being with me in person.

Lastly, I wish to thank all those who have indirectly contributed to this thesis. Your support, whether big or small, has been deeply appreciated.

This work is supported by the International Graduate Program for Excellence in Earth-Space Science (IGPEES) at the University of Tokyo.

Contents

Abstract	i
Acknowledgements	iii
1 Introduction	1
1.1 Status of cosmology	1
1.2 Status of r constraint	2
1.3 Status of reionization constraint	4
1.4 Problem of r constraint on large scale	5
2 Review of CMB and reionization	8
2.1 Basis of cosmology	8
2.1.1 Einstein equations	8
2.1.2 Friedmann equations	10
2.1.3 The components in the universe	11
2.1.4 Important parameters and quantities	12
2.2 Boltzmann equation and CMB temperature anisotropy	13
2.2.1 Distribution function	13
2.2.2 Boltzmann equation for photon	14
2.2.3 CMB anisotropy	19
2.3 Polarization	21
2.3.1 CMB E mode and B mode	21
2.3.2 Generation of CMB polarization	24

2.3.3	Inflationary gravitational waves	27
2.4	Reionization	32
3	Forecasting method and reionization models	35
3.1	Forecast method	35
3.1.1	χ^2	35
3.1.2	Fisher	35
3.2	Experimental model	36
3.2.1	Noise	36
3.3	Reionization model	37
3.3.1	Exponential model	37
3.3.2	Double reionization model	39
3.3.3	Random x_e model	39
4	Results	40
4.1	Fisher analysis results	40
4.2	χ^2 results	40
4.2.1	The exponential model	40
4.2.2	The double reionization model	42
4.2.3	Random x_e model	43
5	Discussion	51
5.1	Compare the role of different angular scales in constraining the tensor-to-scalar ratio	51
5.1.1	Exponential model	51
5.2	Summary	54
5.3	Future Work	55
A	Full power spectra analysis results	59
A.1	The exponential model	59
A.2	The double reionization model	59

B Large-scale power spectra analysis results **64**

 B.1 The exponential model 64

 B.2 The double reionization model 64

C Summary of random x_e models **73**

Bibliography **73**

List of Tables

3.1	Free parameters in the analysis	36
4.1	The prediction of the 1σ uncertainties on r and z_{reio} from the Fisher matrix using the full power spectra.	41
4.2	Summary of the best-fit parameters and uncertainties for the exponential model.	41
4.3	Same as Table 4.2 but for the double reionization model.	41
4.4	Same as Table 4.2 but for the random x_e model which introduces a non-negligible bias.	41
5.1	The prediction of σ_r from the Fisher matrix using only the large-scale power spectra.	51
5.2	The prediction of $\sigma_{z_{\text{reio}}}$ from the Fisher matrix using only the large-scale power spectra.	52
5.3	Summary of best-fit parameters and uncertainties ($\ell < 10$) for the exponential model.	52
5.4	Summary of best-fit parameters and uncertainties when cutting only BB power spectrum for the double reionization model.	52
5.5	Summary of best-fit parameters and uncertainties ($\ell < 10$) for the double reionization model.	52

List of Figures

1.1	Current status of measurements of B -mode power spectrum (Ade et al., 2021). The solid red line shows the theory prediction of the lensing B-modes and the dashed red lines show the theory prediction of the primordial B-modes. Triangles are the upper limits (Bennett et al., 2013; Adachi et al., 2020; Leitch et al., 2005; Montroy et al., 2006; Sievers et al., 2007; Bischoff et al., 2008; Brown et al., 2009; Araujo et al., 2012; Barkats et al., 2014; Kusaka et al., 2018; Tristram et al., 2021; Ade et al., 2022) and the circles (Ade et al., 2021) and squares (Sayre et al., 2020; Choi et al., 2020; Ade et al., 2017) are the detection, respectively.	3
1.2	Repost from figure 15 in Nakane et al. (2024). x_{HI} is the fraction of the neutral hydrogen. The purple solid, blue-dotted, and orange-dashed lines represent three different reionization history models, suggested by Naidu et al. (2020), Ishigaki et al. (2018) and Finkelstein et al. (2019), respectively. The black squares, circles, and diamonds are from Ly α damping wing absorption of gamma-ray bursts (GRBs) (Totani et al., 2006, 2014), QSOs (Schroeder et al., 2013; Davies et al., 2018; Greig et al., 2019; Wang et al., 2020), and Lyman-break galaxies (LBGs) (Curtis-Lake et al., 2023; Hsiao et al., 2023; Umeda et al., 2023), respectively. The gray triangles and circles are from an LAE clustering analysis (Ouchi et al., 2018; Umeda et al., 2023) and Ly α luminosity function (Ouchi et al., 2010; Konno et al., 2014; Inoue et al., 2018; Morales et al., 2021; Goto et al., 2021; Ning et al., 2022; Umeda et al., 2023), respectively. The gray diamonds are from the Ly α equivalent width (EW) distribution of LBGs (Hoag et al., 2019; Mason et al., 2019; Jung et al., 2020; Whitler et al., 2020; Bruton et al., 2023; Morishita et al., 2023). The white triangles and circles are from the Gunn-Peterson trough of QSOs (Fan et al., 2006b), and Ly α and Ly β forest dark fractions of QSOs (McGreer et al., 2015; Zhu et al., 2022; Jin et al., 2023), respectively. The white pentagon is from the CMB observations under the assumption of instantaneous reionization (Aghanim et al., 2020a)	6
2.1	One example of C_l	21
2.2	Examples of C_l^{EE} , C_l^{TE} (left) and C_l^{BB} (right). Here we set $r = 0.01$	23
2.3	One example of the polarization generated by the scalar perturbation. The scalar perturbation only generates the E-mode polarization.	25
2.4	One example of the polarization generated by the tensor perturbation. Here we assume $r = 0.01$	27

2.5	One example of the visibility function. The first peak is at the recombination epoch and the second peak is at the reionization epoch.	33
2.6	The dependence of reionization bump height on τ . The left figure is EE power spectra and the right figure is BB power spectra (assuming $r = 0.01$).	34
3.1	Noise power spectrum. We also plot the EE and BB power spectra here. The noise power spectrum increases quickly on a small scale and becomes much larger than the EE and BB power spectra.	37
3.2	Free electron fraction (x_e) as the function of redshift (z), for the tanh model (blue line), exponential model (orange line), and double reionization model (green line). We set $z_{\text{reio}} = 7.6711$ for the tanh model and $z_{\text{reio}} = 7.29$ for the exponential model to keep the optical depth (τ) as 0.054 matching the result from the Planck collaboration. For the double reionization model, we set three points $(z, x_e) = \{(6, 1.08), (8, 0.13), (9.6, 0.845)\}$ to make $\tau = 0.054$	38
3.3	The process to generate random x_e model. We generate three random redshift points within $5 \sim 22$, among them z_1 is the end of the reionization and $x_e(z_1)$ is 1.08 which corresponds to the Helium reionization. We also generate two random numbers $x_e(z_2)$ and $x_e(z_3)$ within $0 \sim 1$. After that, we use the tanh function to connect them. We consider two cases: $\tau_0 = 0.054$ and $\tau_0 = 0.08$. To generate a reionization history with $\tau = 0.08$, we will accept these numbers if $ \tau - \tau_0 < 0.001$. For $\tau = 0.054$, we will also verify this model consistent with Planck's result (Tristram et al., 2024).	39
4.1	The posterior distribution of r and z_{reio} for the exponential model with $r = 0.01$ and $\tau = 0.054$. The blue lines represent the posterior distribution, while the orange lines represent the Gaussian fit. In the contour plot, yellow indicates high probability and blue indicates low probability.	42
4.2	Same as Fig. 4.1 but with $r = 0.001$	43
4.3	Same as Fig. 4.1 but with $\tau = 0.08$	44
4.4	The free electron fraction x_e for the exponential model with $\tau = 0.054$ (left) and $\tau = 0.08$ (right). The blue lines represent x_e for the fiducial models, the orange lines represent x_e for the best-fit model with $r = 0.01$, and the green lines represent x_e with $r = 0.001$. The orange lines and green lines are almost overlapping.	45
4.5	EE and BB power spectra with $\tau = 0.054$ for the exponential model. The blue line is the fiducial EE power spectrum, the red line is the fiducial BB power spectrum with $r = 0.01$ and the brown line is the fiducial BB power spectrum with $r = 0.001$. The orange line and the green line are the best-fit EE power spectra, and they are almost overlapping. The purple and pink lines are the best-fit BB power spectra with $r = 0.01$ and $r = 0.001$, respectively.	45

4.6	EE and BB power spectra with $\tau = 0.08$ and $r = 0.01$ for the exponential model. Blue and green lines are the fiducial EE and BB power spectra, while orange and red lines are the best-fit power spectra.	46
4.7	Same as Fig. 4.1 but for the double reionization model.	46
4.8	Same as Fig. 4.1 but for the double reionization model.	47
4.9	Same as Fig. 4.6 but for the double reionization model and $\tau = 0.054$	47
4.10	This box plot illustrates the distribution of Euclidean distance between random x_e models and the tanh model with $\tau = 0.054$ (left) and $\tau = 0.08$ (right). The orange line within each box represents the median Euclidean distance. The boxes represent the interquartile range (IQR), which contains the middle 50% of the data. The whiskers extend to the minimum and maximum values within 1.5 times the IQR from the first and third quartiles, respectively.	48
4.11	This box plot illustrates the distribution of the normalized absolute biases $ \Delta r/\sigma_r $ for different combinations of the parameters τ and r . The four groups on the x-axis represent the parameter settings: $\tau = 0.054, r = 0.01$, $\tau = 0.054, r = 0.001$, $\tau = 0.08, r = 0.01$, and $\tau = 0.08, r = 0.001$	48
4.12	The free electron fraction x_e for the random x_e model which introduces a non-negligible bias with $r = 0.001$ and $\tau = 0.08$. The blue lines represent x_e for the fiducial models, the orange lines represent x_e for the best-fit model.	49
4.13	Same as Fig. 4.4 but for the random x_e model which introduces a non-negligible bias with $r = 0.001$ and $\tau = 0.08$	49
4.14	EE and BB power spectra with $\tau = 0.08$ and $r = 0.001$ for the random x_e model which introduces a non-negligible bias. Blue and green lines are the fiducial EE and BB power spectra, while orange and red lines are the best-fit power spectra.	50
5.1	Same as Fig. 4.1 but only using very large scales ($\ell < 10$).	53
5.2	Same as Fig. 4.6 but only using very large scales ($\ell < 10$) and $\tau = 0.054$	54
5.3	Same as Fig. 4.1 but for the double reionization model and cutting only BB power spectrum.	55
5.4	Same as Fig. 5.1 but for the double reionization model.	56
5.5	Same as Fig. 5.2 but for the double reionization model and cutting only BB power spectrum.	57
5.6	Same as Fig. 5.2 but for the double reionization model.	57
5.7	The very large-scale EE power spectra for $\tau = 0.054$ (left) and $\tau = 0.08$ (right).	58
5.8	The very large-scale power spectra for $\tau = 0.054$ (left) and $\tau = 0.08$ (right) for $r = 0.01$	58

5.9	The very large-scale power spectra for $\tau = 0.054$ (left) and $\tau = 0.08$ (right) for $r = 0.001$	58
A.1	Same as Fig. 4.1 but with $r = 0.001$ and $\tau = 0.08$	60
A.2	Same as Fig. 4.6 but with $r = 0.001$	60
A.3	Same as Fig. 4.7 but with $r = 0.001$	61
A.4	Same as Fig. 4.7 but with $\tau = 0.08$	61
A.5	Same as Fig. 4.7 but with $r = 0.001$ and $\tau = 0.08$	62
A.6	Same as Fig. 4.9 but with $r = 0.001$	62
A.7	Same as Fig. 4.9 but with $\tau = 0.08$	63
B.1	Same as Fig. 5.1 but with $r = 0.001$	65
B.2	Same as Fig. 5.1 but with $\tau = 0.08$	65
B.3	Same as Fig. 5.1 but with $r = 0.001$ and $\tau = 0.08$	66
B.4	Same as Fig. 5.2 but with $r = 0.001$	66
B.5	Same as Fig. 4.5 but with $\tau = 0.08$ and only using very large scales ($\ell < 10$). . .	67
B.6	Same as Fig. 5.3 but with $r = 0.001$	67
B.7	Same as Fig. 5.3 but with $\tau = 0.08$	68
B.8	Same as Fig. 5.3 but with $r = 0.001$ and $\tau = 0.08$	68
B.9	Same as Fig. 5.5 but with $r = 0.001$	69
B.10	Same as Fig. 5.5 but with $\tau = 0.08$	69
B.11	Same as Fig. 5.4 but with $r = 0.001$	70
B.12	Same as Fig. 5.4 but with $\tau = 0.08$	70
B.13	Same as Fig. 5.4 but with $r = 0.001$ and $\tau = 0.08$	71
B.14	Same as Fig. 5.6 but with $r = 0.001$	71
B.15	Same as Fig. 5.6 but with $\tau = 0.08$	72
C.1	The free electron fraction x_e for random x_e models with $\tau = 0.054$ (left) and $\tau = 0.08$ (right).	74
C.2	EE and BB power spectra with $\tau = 0.054$ (top) and $\tau = 0.08$ (bottom) for random x_e model.	75

Chapter 1

Introduction

1.1 Status of cosmology

In recent years, cosmology has made remarkable strides, particularly through observations of the cosmic microwave background (CMB), large-scale structure (LSS), and supernovae. These observations have led to a standard model of cosmology, known as the flat Λ Cold Dark Matter (Λ CDM) model (Peebles, 1984; Carroll, 2001; Peebles & Ratra, 2003; Komatsu et al., 2011; Aghanim et al., 2020b). The model describes a universe dominated by dark energy (Λ , $\sim 70\%$) and cold dark matter (CDM, $\sim 25\%$), with baryons contributing the remaining 5% (Guo et al., 2016; Ade et al., 2016; Bullock & Boylan-Kolchin, 2017; Perivolaropoulos & Skara, 2022).

Key observational evidence supporting the Λ CDM model comes from a variety of independent sources, each reinforcing the robustness and accuracy of the model. CMB provides a snapshot of the early universe, revealing the temperature fluctuations that correspond to the density variations from which galaxies and large-scale structures eventually formed. The composition and geometry of the universe predicted by the Λ CDM have been confirmed by the precise measurements of the CMB anisotropies from the Planck satellite (Aghanim et al., 2020a). In addition, LSS surveys map the distribution of galaxies and clusters, which follow the patterns of the gravitational influence of dark matter. Observations from the Sloan Digital Sky Survey (SDSS) (Eisenstein et al., 2005) and the Baryon Oscillation Spectroscopic Survey (BOSS) (Alam et al., 2017) have provided detailed maps of the structure, consistent with the growth of cosmic structures over time predicted by the Λ CDM model. Moreover, Type Ia supernovae have been crucial in establishing the accelerating expansion of the universe, a phenomenon attributed to dark energy (Weinberg et al., 2013; Riess et al., 1998; Perlmutter et al., 1999). The latest constraints on cosmological parameters are (Aghanim et al., 2020a): $h = H_0/(100\text{km s}^{-1}\text{Mpc}^{-1}) = 0.6732$ (but from the observation of supernovae (Riess et al., 2021) $h = 0.732$), $\Omega_m h^2 = 0.14314$, $\Omega_\Lambda = 0.6842$, $\Omega_b h^2 = 0.22383$, $\sigma_8 = 0.8120$, and $n_s = 0.96605$.

Although Λ CDM successfully matches with many observation results, it also faces significant challenges, such as the Hubble tension, which highlights a discrepancy between the Hubble constant values measured from the CMB by Planck (Aghanim et al., 2020a) and local measurements using Cepheids and Type Ia supernovae (Riess et al., 2021), suggesting potential new physics beyond the model. Besides, the exact nature and interactions of cold dark matter remain unknown, prompting ongoing searches through direct detection experiments and

astrophysical observations. Additionally, while dark energy drives the universe's accelerating expansion, its fundamental nature is still mysterious, with various theories like quintessence and modifications to general relativity being explored to understand its properties (Peebles & Ratra, 2003).

1.2 Status of r constraint

The origin of the universe remains an open question and is subject to intense research. The cosmic inflation (Brout et al., 1978; Kazanas, 1980; Starobinsky, 1980; Guth, 1981; Sato, 1981; Albrecht & Steinhardt, 1982; Linde, 1982a), which is thought to drive rapid exponential expansion in the early universe, not only solves the flatness problem and horizon problem related to the CMB temperature but also generates the primordial density fluctuations by quantum fluctuations in the spacetime metric during inflation (Mukhanov & Chibisov, 1981; Guth & Pi, 1982; Hawking, 1982; Linde, 1982b; Starobinsky, 1982; Bardeen et al., 1983) that will eventually become the structure of the universe such as galaxies (Achúcarro et al., 2022). While the primordial density fluctuations predicted by cosmic inflation have already been extensively verified, inflation also predicts the gravitational waves produced in the very early universe (primordial gravitational waves, PGWs) (Starobinskii, 1979; Rubakov et al., 1982; Fabbri & Pollock, 1983; Abbott & Wise, 1984), which remains unconfirmed (LiteBIRD Collaboration et al., 2023).

The most effective method currently for detecting PGWs is to observe a curl pattern in the CMB polarization map (B-mode) since the density fluctuations at linear order do not generate the B-mode and are sensitive to the PGWs (Kamionkowski et al., 1997a,b; Seljak, 1997; Seljak & Zaldarriaga, 1997; Zaldarriaga & Seljak, 1997). The tensor spectrum amplitude, parameterized by the tensor-to-scalar ratio (r) (Davis et al., 1992), is directly linked to the expansion rate during inflation and can provide insights into the energy scale of inflation in the simplest models (Kamionkowski & Kovetz, 2016; Achúcarro et al., 2022).

The CMB observations set upper limits on the PGWs, and provide crucial constraints on inflationary models. The best current constraints on r come from combined CMB observations by the BICEP/Keck Array, Planck, and WMAP, yielding $r < 0.036$ at 95% confidence (Ade et al., 2021), shown in figure 1.1, significantly refining our understanding of the inflationary epoch. These results rule out several high-energy inflation models, pushing the exploration towards lower energy scales and alternative scenarios within the inflationary framework.

Prospects for future measurements and improvements in r and other inflationary parameters are promising, driven by advancements in both technology and observational strategies. Within the next five years, the ground-based Simons Observatory (SO) is expected to achieve a highly precise measurement of the tensor-to-scalar ratio, with an anticipated sensitivity of $\sigma(r) = 0.002$ (Namikawa et al., 2022). Looking further ahead to the 2030s, the LiteBIRD mission, a Japanese-led space-based CMB experiment, aims to push the sensitivity even further, targeting $\sigma(r) < 0.001$ (LiteBIRD Collaboration et al., 2023). By operating above the atmosphere of Earth, LiteBIRD will avoid noise and distortions from the atmosphere, allowing for cleaner and more precise measurements of the CMB polarization. In addition to these efforts, the CMB-S4 project, a comprehensive ground-based initiative, is projected to achieve a sensitivity in the range of $\sigma(r)$ between 5×10^{-4} and 8×10^{-4} (Abazajian et al., 2019). The combined

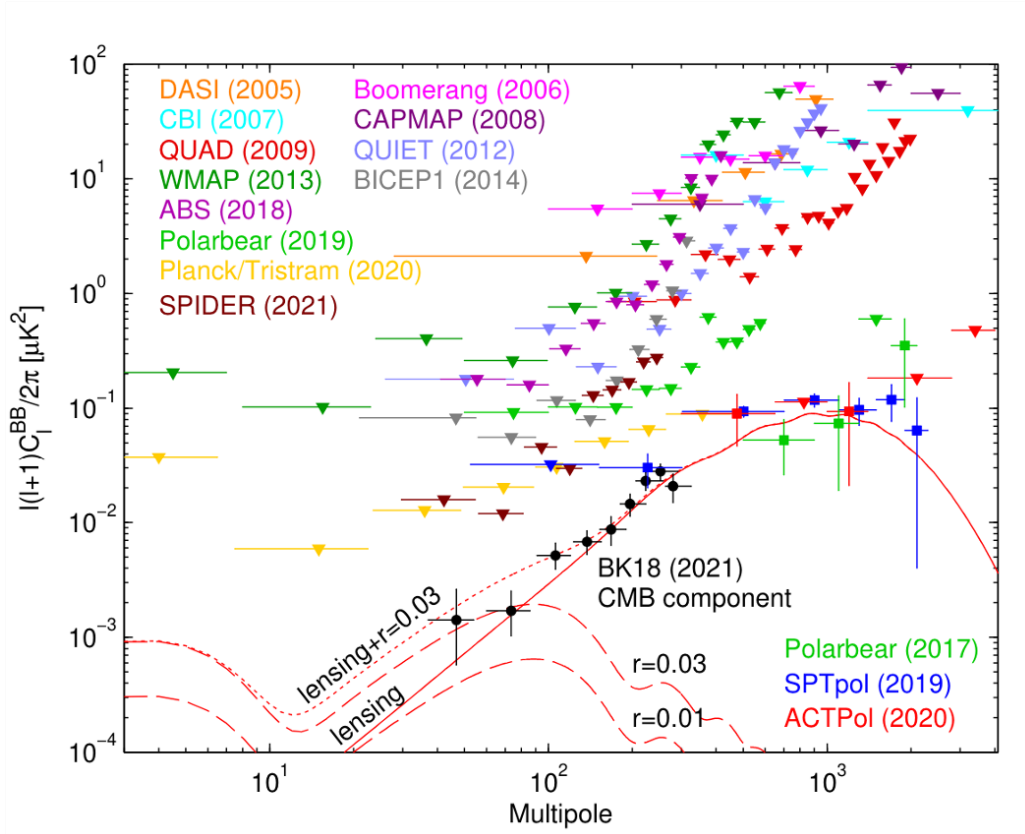


Figure 1.1: Current status of measurements of B -mode power spectrum (Ade et al., 2021). The solid red line shows the theory prediction of the lensing B -modes and the dashed red lines show the theory prediction of the primordial B -modes. Triangles are the upper limits (Bennett et al., 2013; Adachi et al., 2020; Leitch et al., 2005; Montroy et al., 2006; Sievers et al., 2007; Bischoff et al., 2008; Brown et al., 2009; Araujo et al., 2012; Barkats et al., 2014; Kusaka et al., 2018; Tristram et al., 2021; Ade et al., 2022) and the circles (Ade et al., 2021) and squares (Sayre et al., 2020; Choi et al., 2020; Ade et al., 2017) are the detection, respectively.

efforts of these next-generation experiments will significantly enhance our ability to detect or constrain primordial gravitational waves. If future measurements can place an upper limit on $r \sim 0.002$, it would rule out many single-field inflation models with characteristic energy scales larger than the Planck scale (LiteBIRD Collaboration et al., 2023), providing critical insights into the mechanisms driving inflation. These advancements will help to resolve key questions about the inflationary epoch and the fundamental properties of the early universe, marking a new era in precision cosmology.

1.3 Status of reionization constraint

The reionization epoch represents a critical phase in the history of the universe, marking the transition from the dark ages to a universe filled with light and complex structures. This period saw the formation of the first stars and galaxies that ionized the neutral hydrogen in the intergalactic medium roughly between $z \simeq 12$ and $z \simeq 6$, and the quasars that ionized the helium from $z \simeq 6$ to $z \simeq 2$ (Adam et al., 2016). The ultraviolet light from these early stars and galaxies ionized the neutral hydrogen in the intergalactic medium, leading to the formation of large ionized bubbles that eventually overlapped and reionized the entire universe (Fan et al., 2006a). This reionization process significantly influenced the thermal history and structure formation of the universe by providing feedback mechanisms, such as evaporation by photoionization heating, increasing the pressure support in galaxies, and suppressing star formation in low-mass galaxies (Barkana & Loeb, 2001). Moreover, the reionization epoch leaves an imprint on CMB, particularly in the polarization patterns. It damps the primary CMB temperature anisotropies on small scales (Adam et al., 2016), and produces a bump in the polarization power spectrum at large angular scales, which corresponds to the horizon at the time of reionization (Hu & Dodelson, 2002). Additionally, temperature anisotropies can also be generated by the kinetic Sunyaev-Zeldovich (kSZ) effect (Sunyaev & Zeldovich, 1980), which arises from Doppler shifts caused by scattering electrons. Understanding the timing and progression of reionization is thus essential for constructing accurate models of the universe's evolution and for interpreting observations from current and future cosmological surveys.

Current constraints on the reionization epoch from CMB measurements provide critical insights into the timing and duration of this transformative period in the history of the universe. By assuming a simple tanh model of the reionization history, the latest result from the Planck satellite's 2018 data release has significantly refined our understanding by providing a precise measurement of the optical depth due to reionization, which is constrained to $\tau = 0.054 \pm 0.007$, and it corresponds to the reionization redshift mid-point z_{re} at 7.67 ± 0.73 (Aghanim et al., 2020a). However, recently, without relying on large-scale CMB polarization, the constraint on τ becomes 0.080 ± 0.012 (Giarè et al., 2024). This huge difference shows that obtaining precise measurements of τ is still significantly challenging.

In addition to the CMB observation giving the integration measurement of the reionization epoch, observational evidence of reionization history comes significantly from studies of high-redshift quasars and galaxies, which provide insights into the ionization state of the intergalactic medium (IGM). The measurements of Gunn-Peterson troughs (Gunn & Peterson, 1965) in the spectra of quasars (QSOs), shows the reionization is completed by $z \sim 6$ (Fan et al., 2006b), while the observations of the fluctuations of the Lyman- α optical depth in high-redshift quasar

spectra (Bosman et al., 2022) and the inferred low mean free path of ionizing photons (Gaikwad et al., 2023) suggest that reionization may complete late around $z \sim 5.2$.

Despite the precise observation of τ and the time (z_{re} and z_{end}) of the reionization, the detailed history of reionization remains poorly understood. Especially the timeline and spatial variation of the reionization process at higher redshifts ($z > 6$) are still highly uncertain. The Ly α emission line, due to its sensitivity to neutral hydrogen fraction, serves as a significant probe for studying reionization history (Ouchi et al., 2020). Yet, Ly α emitters (LAEs) at high redshifts ($z > 7$) are exceedingly rare, making it challenging to use these emitters to constrain the reionization history (Nakane et al., 2024). The advent of the James Webb Space Telescope (JWST) has enabled deeper observations at higher redshifts, providing new constraints, but our understanding of the reionization history remains limited. Figure 1.2 shows the latest constraint on the reionization history (Nakane et al., 2024), illustrating that a wide range of models remains viable under current constraints. This highlights the significant uncertainties in our understanding of reionization. One of the primary motivations for this project is to examine how these uncertainties, stemming from the unknown specifics of the reionization history, impact the detection of PGWs.

1.4 Problem of r constraint on large scale

Detecting PGWs through B-mode polarization presents significant challenges, both in terms of theoretical uncertainties and observational difficulties. In the simplest single-field slow-roll inflation models, PGWs arise from quantum vacuum fluctuations in spacetime. However, alternative scenarios involving additional fields, such as an SU(2) gauge field, can produce strongly scale-dependent gravitational waves (Maleknejad & Sheikh-Jabbari, 2011, 2013; Dimastrogiovanni et al., 2017), resulting in larger amplitude B-mode power spectra on large scales (e.g., $l \sim 4$) (Campeti et al., 2024), which correspond to the reionization bump. The reionization bump is influenced by the history of the reionization epoch, introducing further uncertainties and complicating the differentiation of inflationary models. Additionally, cosmic variance, which arises from the limited number of large-scale modes available for measurement, imposes fundamental limits on the precision of r measurements.

Foreground contamination from astronomical phenomena, including emissions from the Milky Way and gravitational lensing by large-scale structure, also poses significant challenges. Galactic foreground emissions include thermal emission from interstellar dust aligned with the Galactic magnetic field and synchrotron emission from electrons spiraling in the Galactic magnetic field (LiteBIRD Collaboration et al., 2023). To mitigate these challenges, various methods have been developed for foreground cleaning. These methods can be broadly categorized into parametric and blind approaches (Carones et al., 2023). Parametric methods, such as Commander (Eriksen et al., 2008) and FGBuster (Stompor et al., 2009) involve modeling and subtracting the foregrounds, but they may introduce biases if the models are inaccurate. Blind methods, which do not rely on specific foreground models, such as ILC (Bennett et al., 2003; Tegmark et al., 2003) and NILC (Delabrouille et al., 2009), can avoid such biases but often struggle with the complexity of galactic foregrounds. Additionally, gravitational lensing modifies the pattern of the CMB polarization map, producing B-modes even in the absence of original B-modes at the CMB last scattering since CMB photons are deflected by the gravitational potentials (LiteBIRD Collaboration et al., 2023). Delensing techniques are being developed to remove

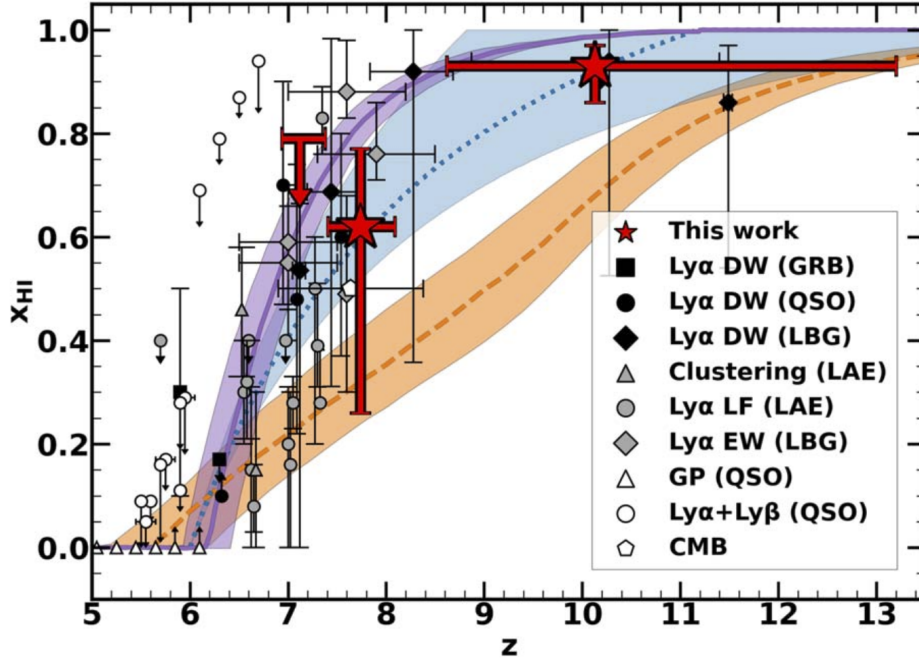


Figure 1.2: Repost from figure 15 in Nakane et al. (2024). x_{HI} is the fraction of the neutral hydrogen. The purple solid, blue-dotted, and orange-dashed lines represent three different reionization history models, suggested by Naidu et al. (2020), Ishigaki et al. (2018) and Finkelstein et al. (2019), respectively. The black squares, circles, and diamonds are from Ly α damping wing absorption of gamma-ray bursts (GRBs) (Totani et al., 2006, 2014), QSOs (Schroeder et al., 2013; Davies et al., 2018; Greig et al., 2019; Wang et al., 2020), and Lyman-break galaxies (LBGs) (Curtis-Lake et al., 2023; Hsiao et al., 2023; Umeda et al., 2023), respectively. The gray triangles and circles are from an LAE clustering analysis (Ouchi et al., 2018; Umeda et al., 2023) and Ly α luminosity function (Ouchi et al., 2010; Konno et al., 2014; Inoue et al., 2018; Morales et al., 2021; Goto et al., 2021; Ning et al., 2022; Umeda et al., 2023), respectively. The gray diamonds are from the Ly α equivalent width (EW) distribution of LBGs (Hoag et al., 2019; Mason et al., 2019; Jung et al., 2020; Whitler et al., 2020; Bruton et al., 2023; Morishita et al., 2023). The white triangles and circles are from the Gunn-Peterson trough of QSOs (Fan et al., 2006b), and Ly α and Ly β forest dark fractions of QSOs (McGreer et al., 2015; Zhu et al., 2022; Jin et al., 2023), respectively. The white pentagon is from the CMB observations under the assumption of instantaneous reionization (Aghanim et al., 2020a)

this lensing signal, including utilizing internal CMB lensing maps and external mass-tracer maps (Lizancos et al., 2021; Smith et al., 2012; Carron, 2019), such as the cosmic infrared background (CIB) (Sherwin & Schmittfull, 2015; Simard et al., 2015) and intensity mapping signals (Sigurdson & Cooray, 2005; Karkare, 2019), but their effectiveness in realistic scenarios remains to be fully demonstrated.

This thesis focuses on the theory of uncertainty brought by the poor understanding of reionization history. The thesis is organized as follows. We review the basic knowledge of cosmology, CMB, and reionization in section 2. We introduce our method in section 3. We show the uncertainty and bias when we assume different fiducial reionization models in section 4. Finally, we discuss the contribution of different angular scale in section 5.

Chapter 2

Review of CMB and reionization

In this chapter, we first summarize the background evolution of the universe and define important quantities in cosmology. We then review the Boltzmann equation, CMB temperature and polarization anisotropies, inflationary gravitational waves, and CMB angular power spectrum. We also review cosmic reionization. This chapter is based on the textbook of Dodelson & Schmidt (2020). We assume $c = 1$ for the whole chapter.

2.1 Basis of cosmology

In this section, we start with the Einstein equation to derive equations describing the background evolution of the universe.

2.1.1 Einstein equations

The Einstein equation is given by

$$G_{\mu\nu} + \Lambda g_{\mu\nu} = 8\pi G T_{\mu\nu}, \quad (2.1)$$

where $G_{\mu\nu}$ is defined as

$$G_{\mu\nu} \equiv R_{\mu\nu} - \frac{1}{2}g_{\mu\nu}R. \quad (2.2)$$

Λ is the cosmological constant, $g_{\mu\nu}$ is the metric, $R_{\mu\nu}$ is the Ricci tensor, R is the Ricci scalar, and $T_{\mu\nu}$ is the energy-momentum tensor. We will explain these symbols in the following texts.

Metric

The invariant interval in four spacetime, which is not changed by coordinate change, is shown as

$$ds^2 = \sum_{\mu,\nu=0}^3 g_{\mu\nu} dx^\mu dx^\nu, \quad (2.3)$$

where x^0 is time, t , and x^i are the spatial coordinates. The metric used for calculating the invariant interval in a smooth (isotropic and homogeneous) and expanding universe is the Friedmann–Lemaître–Robertson–Walker (FLRW) metric:

$$g_{\mu\nu} = \begin{bmatrix} -1 & 0 & 0 & 0 \\ 0 & a^2(t) & 0 & 0 \\ 0 & 0 & a^2(t) & 0 \\ 0 & 0 & 0 & a^2(t) \end{bmatrix}. \quad (2.4)$$

Here, a is a scale factor, introduced for describing expansion. We set a at present as 1, and less than 1 at the previous time.

Geodesic and Christoffel symbol

The geodesic is the curve that parallel-transport its tangent vector (Schutz, 2022). If we use λ to parameterize this line, the tangent to the curve is $d\vec{x}/d\lambda$. The vector \vec{V} parallel-transporting the line is:

$$\frac{d\vec{V}}{d\lambda} = 0. \quad (2.5)$$

The left-hand side of it is expanded as:

$$\begin{aligned} \frac{d\vec{V}}{d\lambda} &= \frac{dV^\alpha}{d\lambda} \vec{e}_\alpha + V^\alpha \frac{d\vec{e}_\alpha}{d\lambda} \\ &= \frac{dV^\alpha}{d\lambda} \vec{e}_\alpha + V^\alpha \frac{dx^\beta}{d\lambda} \frac{\partial \vec{e}_\alpha}{\partial x^\beta}, \end{aligned} \quad (2.6)$$

where \vec{e}_α is the basis vector. The $\partial \vec{e}_\alpha / \partial x^\beta$ can also be expanded as a linear combination of the basis vectors:

$$\frac{\partial \vec{e}_\alpha}{\partial x^\beta} = \Gamma_{\alpha\beta}^\mu \vec{e}_\mu, \quad (2.7)$$

where the $\Gamma_{\alpha\beta}^\mu$ is called the Christoffel symbol. The vector \vec{V} is the tangent $d\vec{x}/d\lambda$ for the geodesic. Substituting Eq. (2.7) into Eq. (2.6), we obtain

$$\begin{aligned} \frac{d}{d\lambda} \left(\frac{d\vec{x}}{d\lambda} \right) &= \frac{d}{d\lambda} \left(\frac{dx^\alpha}{d\lambda} \right) \vec{e}_\alpha + \frac{dx^\alpha}{d\lambda} \frac{dx^\beta}{d\lambda} \Gamma_{\alpha\beta}^\mu \vec{e}_\mu \\ &= \frac{d}{d\lambda} \left(\frac{dx^\mu}{d\lambda} \right) \vec{e}_\mu + \frac{dx^\alpha}{d\lambda} \frac{dx^\beta}{d\lambda} \Gamma_{\alpha\beta}^\mu \vec{e}_\mu = 0. \end{aligned} \quad (2.8)$$

Therefore, the geodesic equation is:

$$\frac{d^2 x^\mu}{d\lambda^2} = -\Gamma_{\alpha\beta}^\mu \frac{dx^\alpha}{d\lambda} \frac{dx^\beta}{d\lambda} \quad (2.9)$$

In addition, the relationship between the Christoffel symbol and metric is:

$$\Gamma_{\alpha\beta}^\mu = \frac{g^{\mu\nu}}{2} \left(\frac{\partial g_{\alpha\nu}}{\partial x^\beta} + \frac{\partial g_{\mu\nu}}{\partial x^\alpha} - \frac{\partial g_{\alpha\beta}}{\partial x^\nu} \right). \quad (2.10)$$

Ricci tensor and Ricci scalar

The Ricci tensor is expressed by the Christoffel symbols:

$$R_{\mu\nu} = \Gamma_{\mu\nu,\alpha}^{\alpha} - \Gamma_{\mu\alpha,\nu}^{\alpha} + \Gamma_{\beta\alpha}^{\alpha}\Gamma_{\mu\nu}^{\beta} - \Gamma_{\beta\nu}^{\alpha}\Gamma_{\mu\alpha}^{\beta}, \quad (2.11)$$

where $,\alpha$ means $\partial/\partial x^{\alpha}$. The Ricci scalar is the contraction of the Ricci tensor:

$$R \equiv g^{\mu\nu}R_{\mu\nu} \quad (2.12)$$

By putting the FLRW metric into the Christoffel symbol, we can get the following non-vanishing values:

$$\begin{aligned} \Gamma_{ij}^0 &= \delta_{ij}\dot{a}a \\ \Gamma_{0j}^i &= \Gamma_{j0}^i = \delta_{ij}\frac{\dot{a}}{a}, \end{aligned} \quad (2.13)$$

where \dot{a} means $da/dx^0 = da/dt$.

Energy-momentum tensor

The energy-momentum tensor in the smooth universe is:

$$T_{\nu}^{\mu} = \begin{bmatrix} -\rho & 0 & 0 & 0 \\ 0 & P & 0 & 0 \\ 0 & 0 & P & 0 \\ 0 & 0 & 0 & P \end{bmatrix} \quad (2.14)$$

where ρ is the energy density and P is the pressure. The photon, neutrino, baryon, dark matter, and dark energy contribute to the energy density.

2.1.2 Friedmann equations

The Einstein equation is a tensor equation, so we can write several equations for the components. For the smooth universe, the Ricci tensor does not vanish only when $\mu = \nu$. First, we consider the time-time component ($\mu = \nu = 0$). From Eqs. (2.11) and (2.13), we obtain:

$$\begin{aligned} R_{00} &= \Gamma_{00,\alpha}^{\alpha} - \Gamma_{0\alpha,0}^{\alpha} + \Gamma_{\beta\alpha}^{\alpha}\Gamma_{00}^{\beta} - \Gamma_{\beta 0}^{\alpha}\Gamma_{0\alpha}^{\beta} \\ &= -\delta_{ii}\frac{\partial}{\partial x^0}\left(\frac{\dot{a}}{a}\right) - \left(\frac{\dot{a}}{a}\right)^2\delta_{ij}\delta^{ij} \\ &= -3\frac{\ddot{a}}{a}. \end{aligned} \quad (2.15)$$

Next, we consider the spatial-spatial components:

$$\begin{aligned}
R_{ij} &= \Gamma_{ij,\alpha}^\alpha - \Gamma_{i\alpha,j}^\alpha + \Gamma_{\beta\alpha}^\alpha \Gamma_{ij}^\beta - \Gamma_{\beta j}^\alpha \Gamma_{i\alpha}^\beta \\
&= \delta_{ij}(\ddot{a}a + \dot{a}^2) + 3\delta_{ij}\dot{a}^2 - \delta_{ij}\dot{a}^2 - \delta_{ij}\dot{a}^2 \\
&= \delta_{ij}(2\dot{a}^2 + a\ddot{a}).
\end{aligned} \tag{2.16}$$

Therefore, the Ricci scalar is

$$\begin{aligned}
R &= g^{\mu\nu} R_{\mu\nu} \\
&= -R_{00} + \frac{1}{a^2} R_{ii} \\
&= 6 \left[\frac{\ddot{a}}{a} + \left(\frac{\dot{a}}{a} \right)^2 \right].
\end{aligned} \tag{2.17}$$

Then the time-time component in the Einstein equation is:

$$\begin{aligned}
R_{00} - \frac{1}{2}g_{00}R + \Lambda g_{00} &= 8\pi G T_{00}, \\
\left(\frac{\dot{a}}{a} \right)^2 - \frac{1}{3}\Lambda &= \frac{8\pi G}{3}\rho.
\end{aligned} \tag{2.18}$$

If we define the energy-momentum tensor for cosmological constant as

$$T_{(\Lambda)\nu}^\mu = -\frac{\Lambda}{8\pi G}\delta_\nu^\mu, \tag{2.19}$$

the second line of Eq. (2.18) becomes

$$\left(\frac{\dot{a}}{a} \right)^2 = \frac{8\pi G}{3}\rho. \tag{2.20}$$

The spatial-spatial component in the Einstein equation is:

$$\begin{aligned}
R_{ij} - \frac{1}{2}g_{ij}R &= 8\pi G T_{ij}, \\
\frac{\ddot{a}}{a} + \frac{1}{2}\left(\frac{\dot{a}}{a} \right)^2 &= -4\pi G P, \\
\frac{\ddot{a}}{a} &= -\frac{4\pi G}{3}(\rho + 3P).
\end{aligned} \tag{2.21}$$

Eq. (2.20) and the third line in Eq. (2.21) are called Friedmann equations.

2.1.3 The components in the universe

By taking the derivative of both sides of Eq. (2.20), we obtain:

$$2\dot{a}\ddot{a} = \frac{8\pi G}{3}(\dot{\rho}a^2 + 2\dot{a}a\dot{\rho}) \tag{2.22}$$

Substituting Eq. (2.21) into the above equation, we obtain:

$$\frac{d}{dt}(a^3\rho) = -P\frac{da^3}{dt}, \quad (2.23)$$

which is called the conservation law. The equation of state of cosmic inventory is:

$$P = w\rho. \quad (2.24)$$

By substituting the above equation into Eq. (2.23), we obtain the evolution of the density (assuming w is a constant):

$$\rho \propto a^{-3(1+w)}. \quad (2.25)$$

For matter (including the dark matter and the baryon), $w = 0$, and

$$\rho_m \propto a^{-3}. \quad (2.26)$$

For radiation (including the photon and the neutrino), $w = 1/3$, and

$$\rho_r \propto a^{-4}. \quad (2.27)$$

The dark energy drives the accelerated cosmic expansion:

$$\ddot{a} = -\frac{4\pi G}{3}(\rho + 3P) > 0, \quad (2.28)$$

i.e. $w < -1/3$. Specifically, when $w = -1$ ($P = -\rho$), the energy density is constant which matches Eq. (2.19). This type of dark energy is called the cosmological constant.

2.1.4 Important parameters and quantities

Hubble parameter

If a galaxy does not have a peculiar velocity but flows with the universe expanding, the velocity is:

$$r = \frac{d}{dt}(ax) = \dot{a}x = \frac{\dot{a}}{a}(ax) = \frac{\dot{a}}{a}d \equiv Hd. \quad (2.29)$$

Equation (2.29) is called the Hubble-Lemaître law, and H is the Hubble parameter. The present Hubble parameter is H_0 , which is also called the Hubble constant.

Redshift

The wavelength of light increases as the universe expands:

$$\frac{\lambda'}{\lambda} = \frac{p}{p'} = \frac{a(t')}{a(t)}, \quad (2.30)$$

where p is the momentum. We define redshift as:

$$z \equiv \frac{\lambda_0 - \lambda}{\lambda} = \frac{a(t_0)}{a(t)} - 1 \quad (2.31)$$

where subscript 0 means the quantity at present.

Comoving horizon

The comoving horizon, also known as the conformal time, is defined by:

$$\eta(t) \equiv \int_0^t \frac{dt'}{a(t')}. \quad (2.32)$$

It describes the comoving distance that light traveled for the Big Bang, which means no information can propagate further than η . It increases as time passes by and we use it as a time variable.

Comoving Hubble radius

We change the integration variables from t' to $\ln a'$ in Eq. (2.32):

$$\eta = \int_0^a d \ln a' \frac{1}{a' H(a')}, \quad (2.33)$$

where we define $(aH)^{-1}$ as comoving Hubble radius.

2.2 Boltzmann equation and CMB temperature anisotropy

In this section, we discuss how the metric perturbation and the Thomson scattering by electrons affect photon distribution in the phase space, and we derive the CMB temperature anisotropy.

2.2.1 Distribution function

The distribution function $f(\vec{x}, \vec{p}, t)$ describes the number of particles near position \vec{x} and momentum \vec{p} . The energy density is described by

$$\rho_i(\vec{x}, t) = g_i \int \frac{d^3 p}{(2\pi)^3} f_i(\vec{x}, \vec{p}, t) E_i(p), \quad (2.34)$$

where $E_i(p) = \sqrt{p^2 + m_i^2}$, g_i is the degeneracy of the species, and $(2\pi)^3$ is from the Heisenberg's principle, i means different species. For the bosons whose temperature is T in equilibrium, they follow the Bose-Einstein distributions:

$$f_{\text{BE}}(E) = \frac{1}{e^{(E-\mu)/T} - 1}, \quad (2.35)$$

where μ is the chemical potential. The fermions follow the Fermi-Dirac distributions:

$$f_{\text{FD}}(E) = \frac{1}{e^{(E-\mu)/T} + 1}. \quad (2.36)$$

By these equations, we can use temperature to describe the energy density.

2.2.2 Boltzmann equation for photon

The Boltzmann equation describes the evolution of the distribution function which is given by

$$\frac{df}{dt} = C[f], \quad (2.37)$$

where $C[f]$ is the collision term. Here, we are particularly interested in the evolution of the distribution function of photons. In the following text, we include the metric perturbation and the Thomson scattering by electrons to see how they affect the distribution function of photons.

The total derivative in the left-hand side of Eq. (2.37) can be expanded as:

$$\frac{\partial f}{\partial t} + \frac{\partial f}{\partial x} \frac{dx}{dt} + \frac{\partial f}{\partial p} \frac{dp}{dt} + \frac{\partial f}{\partial \hat{p}^i} \frac{d\hat{p}^i}{dt} = C[f]. \quad (2.38)$$

The effect from the metric perturbation is introduced when we calculate dx/dt , dp/dt , and $d\hat{p}^i/dt$, where \hat{p}^i is the direction of the photon satisfying $\delta_{ij}\hat{p}^i\hat{p}^j = 1$. The scattering from the electron is in the collision term, $C[f]$.

Metric perturbation

Let us first discuss the metric perturbation. The scalar metric perturbation in the conformal Newtonian gauge is:

$$g_{\mu\nu}(\vec{x}, t) = \begin{bmatrix} -1 - 2\Psi(\vec{x}, t) & 0 & 0 & 0 \\ 0 & a^2(t)(1 + 2\Phi(\vec{x}, t)) & 0 & 0 \\ 0 & 0 & a^2(t)(1 + 2\Phi(\vec{x}, t)) & 0 \\ 0 & 0 & 0 & a^2(t)(1 + 2\Phi(\vec{x}, t)) \end{bmatrix}, \quad (2.39)$$

where Ψ corresponds to the Newtonian potential, and Φ is the perturbation to the spatial curvature.

We first consider dx^i/dt :

$$\frac{dx^i}{dt} = \frac{dx^i}{d\lambda} \frac{d\lambda}{dt} \quad (2.40)$$

We define the four-momentum vector as

$$P^\mu \equiv \frac{dx^\mu}{d\lambda} \quad (2.41)$$

Then, Eq. (2.40) becomes:

$$\frac{dx^i}{dt} = \frac{P^i}{P^0} \quad (2.42)$$

For massless photons, we have

$$P^2 = g_{\mu\nu} P^\mu P^\nu = -(1 + 2\Psi)(P^0)^2 + p^2 = 0, \quad (2.43)$$

where p^2 is defined by

$$p^2 \equiv g_{ij} P^i P^j \quad (2.44)$$

Therefore, the P^0 is

$$\begin{aligned} P^0 &= \frac{p}{\sqrt{1 + 2\Psi}} \\ &\simeq p(1 - \Psi) \end{aligned} \quad (2.45)$$

Since P^i is proportional to the \hat{p}^i , we assume $P^i = C\hat{p}^i$. Substituting P^i into Eq. (2.44), we obtain

$$\begin{aligned} p^2 &= g_{ij} \hat{p}^i \hat{p}^j C^2 \\ &= a^2(1 + 2\Phi)C^2, \end{aligned} \quad (2.46)$$

and find

$$\begin{aligned} P^i &= \frac{p}{a\sqrt{1 + 2\Phi}} \hat{p}^i \\ &\simeq p\hat{p}^i \frac{1 - \Phi}{a} \end{aligned} \quad (2.47)$$

Substituting Eqs (2.45) and (2.47) into Eq. (2.40), we obtain:

$$\begin{aligned} \frac{dx^i}{dt} &= \frac{p\hat{p}^i(1 - \Phi)}{ap(1 - \Psi)} \\ &\simeq \frac{\hat{p}^i}{a}(1 + \Psi - \Phi) \end{aligned} \quad (2.48)$$

Note that the calculations above all keep only the first order.

Next, we consider dp/dt . According to Eq. (2.45), P^0 contains the momentum, and we start from dP^0/dt :

$$\frac{dP^0}{dt} = \frac{dP^0}{d\lambda} \frac{d\lambda}{dt} \quad (2.49)$$

According to Eq. (2.41), $d\lambda/dt = 1/P^0$. Using the geodesic equation (2.9), we know:

$$\begin{aligned} \frac{dP^0}{d\lambda} &= -\Gamma_{\alpha\beta}^0 P^\alpha P^\beta \\ &= -\frac{g^{00}}{2} \left(\frac{\partial g_{\alpha 0}}{\partial x^\beta} + \frac{\partial g_{\beta 0}}{\partial x^\alpha} - \frac{\partial g_{\alpha\beta}}{\partial x^0} \right) P^\alpha P^\beta \\ &\simeq \frac{1 - 2\Psi}{2} \left(-2 \frac{\partial \Psi}{\partial t} p^2 (1 - \Psi)^2 - 4 \frac{\partial \Psi}{\partial x^i} p^2 (1 - \Psi) \hat{p}^i \frac{1 - \Phi}{a} - \delta_{ij} \frac{\partial}{\partial t} (a^2(1 + 2\Phi)) P^i P^j \right). \end{aligned} \quad (2.50)$$

We keep only the zeroth and first order:

$$\frac{dP^0}{d\lambda} \simeq p^2 \left(-\frac{\partial\Psi}{\partial t} - 2\frac{\partial\Psi}{\partial x^i} \frac{\hat{p}^i}{a} - H - \frac{\partial\Phi}{\partial t} \right). \quad (2.51)$$

Using Eq. (2.45), we rewrite the left-hand side of Eq. (2.49):

$$\frac{dP^0}{dt} = \frac{dp}{dt}(1 - \Psi) - p \left(\frac{\partial\Psi}{\partial t} + \frac{\partial\Psi}{\partial x^i} \frac{dx^i}{dt} \right). \quad (2.52)$$

Substituting Eqs (2.51) and (2.52) into Eq. (2.49), we obtain

$$\frac{dp}{dt}(1 - \Psi) - p \left(\frac{\partial\Psi}{\partial t} + \frac{\partial\Psi}{\partial x^i} \frac{\hat{p}^i}{a} (1 + \Psi - \Phi) \right) = \frac{p}{1 - \Psi} \left(-\frac{\partial\Psi}{\partial t} - 2\frac{\partial\Psi}{\partial x^i} \frac{\hat{p}^i}{a} - H - \frac{\partial\Phi}{\partial t} \right) \quad (2.53)$$

After keeping only the zeroth and first order, we obtain

$$\frac{dp}{dt} \simeq -p \left(\frac{\partial\Psi}{\partial x^i} \frac{\hat{p}^i}{a} + H + \frac{\partial\Phi}{\partial t} \right). \quad (2.54)$$

Therefore, the left-hand side of the Boltzmann equation is written in terms of the metric perturbations as

$$\frac{df}{dt} = \frac{\partial f}{\partial t} + \frac{\hat{p}^i}{a} \frac{\partial f}{\partial x^i} - p \frac{\partial f}{\partial p} \left(H + \frac{\partial\Phi}{\partial t} + \frac{\hat{p}^i}{a} \frac{\partial\Psi}{\partial x^i} \right). \quad (2.55)$$

Distribution function perturbation

Photons follow the Bose-Einstein distribution, where we assume $\mu = 0$:

$$f(p, T) = \frac{1}{\exp(p/T) - 1}, \quad (2.56)$$

We expand it around T :

$$\begin{aligned} f(p, T + \delta T) &\simeq f(p, T) + \frac{\partial f(p, T)}{\partial T} \delta T \\ &= f(p, T) - p \frac{\partial f(p, T)}{\partial p} \delta T / T. \end{aligned} \quad (2.57)$$

Here, $T(t)$ is only the function of time, but the perturbation δT is also the function of the position and the momentum. We define $\Theta(\vec{x}, \hat{p}, t) \equiv \delta T / T$. We substitute Eq. (2.57) into

Eq. (2.55) and only keep the zeroth and the first order:

$$\begin{aligned} \frac{df}{dt} &\simeq \frac{\partial(f(p, T) - p \frac{\partial f}{\partial p} \Theta)}{\partial t} + \frac{\hat{p}^i \partial(f(p, T) - p \frac{\partial f}{\partial p} \Theta)}{a \partial x^i} - \frac{\partial(f(p, T) - p \frac{\partial f}{\partial p} \Theta)}{\partial p} p \left(H + \frac{\partial \Phi}{\partial t} + \frac{\hat{p}^i \partial \Psi}{a \partial x^i} \right) \\ &\simeq \left(\frac{\partial f}{\partial T} \frac{dT}{dt} - p \frac{\partial f}{\partial p} H \right) + p \left(- \frac{\partial}{\partial p} \left(p \frac{\partial f}{\partial p} \right) \frac{\Theta}{T} \frac{dT}{dt} - \frac{\partial f}{\partial p} \frac{\partial \Theta}{\partial t} \right. \\ &\quad \left. - \frac{\hat{p}^i \partial f}{a \partial p \partial x^i} \frac{\partial \Theta}{\partial t} - \frac{\partial f}{\partial p} \Theta H - \frac{\partial f}{\partial p} \frac{\partial \Phi}{\partial t} - \frac{\partial f}{\partial p} \frac{\hat{p}^i \partial \Psi}{a \partial x^i} \right). \end{aligned} \quad (2.58)$$

The first bracket in Eq. (2.58) is the zeroth order term and it should be equal to 0 since in the equilibrium state there is no collision. Then, the Boltzmann equation becomes:

$$\begin{aligned} C[f] &= p \left(- \frac{\partial f}{\partial p} \frac{\Theta}{T} \frac{dT}{dt} - \frac{\partial f}{\partial p} \frac{\partial \Theta}{\partial t} - \frac{\hat{p}^i \partial f}{a \partial p \partial x^i} \frac{\partial \Theta}{\partial t} - \frac{\partial f}{\partial p} \Theta H - \frac{\partial f}{\partial p} \frac{\partial \Phi}{\partial t} - \frac{\partial f}{\partial p} \frac{\hat{p}^i \partial \Psi}{a \partial x^i} \right) \\ &= -p \frac{\partial f}{\partial p} \left(\frac{\partial \Theta}{\partial t} + \frac{\hat{p}^i \partial \Theta}{a \partial x^i} + \frac{\partial \Phi}{\partial t} + \frac{\hat{p}^i \partial \Psi}{a \partial x^i} \right). \end{aligned} \quad (2.59)$$

Collision term

Photons interact with electrons via the Compton scattering:

$$e^-(\vec{q}) + \gamma(\vec{p}) \leftrightarrow e^-(\vec{q}') + \gamma(\vec{p}') \quad (2.60)$$

The collision term due to the Compton scattering is given by (Dodelson & Schmidt, 2020)

$$\begin{aligned} C[f(\vec{p})] &= \frac{1}{2E(p)} \int \frac{d^3 q}{(2\pi)^3 2E_e(q)} \int \frac{d^3 q'}{(2\pi)^3 2E_e(q')} \int \frac{d^3 p'}{(2\pi)^3 2E(p')} \sum_{\text{spins}} |\mathcal{M}|^2 \\ &\quad \times (2\pi)^4 \delta_D^{(3)}(\vec{p} + \vec{q} - \vec{p}' - \vec{q}') \delta_D^{(1)}(E(p) + E_e(q) - E(p') - E_e(q')) \\ &\quad \times (f_e(\vec{q}') f(\vec{p}') - f_e(\vec{q}) f(\vec{p})), \end{aligned} \quad (2.61)$$

where \mathcal{M} is the scattering amplitude, $\delta_D^{(n)}$ is the n -dimensional Dirac delta function, E is the photon's energy, E_e is the electron's energy, and f_e is the electron's distribution function. Since $E^2 = p^2 + m^2$, $E(p) = p$ and $E_e(q) \simeq m_e$ after electron becoming non-relativistic. By integrating over \vec{q}' , the collision term becomes:

$$\begin{aligned} C[f(\vec{p})] &= \frac{\pi}{2m_e p} \int \frac{d^3 q}{(2\pi)^3 2m_e} \int \frac{d^3 p'}{(2\pi)^3 2p'} \delta_D^{(1)}(p + E_e(q) - p' - E_e(|\vec{q} + \vec{p} - \vec{p}'|)) \\ &\quad \times \sum_{\text{spins}} |\mathcal{M}|^2 (f_e(\vec{q} + \vec{p} - \vec{p}') f(\vec{p}') - f_e(\vec{q}) f(\vec{p})). \end{aligned} \quad (2.62)$$

Now, we expand $\delta_D^{(1)}(p - p' - E_e(q') + E_e(q))$ at $E_e(q')$ around $E_e(q)$:

$$\begin{aligned} \delta_D^{(1)}(p - p' - E_e(q') + E_e(q)) &\simeq \delta_D^{(1)}(p - p') \\ &+ \frac{\partial \delta_D^{(1)}(p - p' - E_e(q') + E_e(q))}{\partial E_e(q')} \Big|_{E_e(q')=E_e(q)} (E_e(q') - E_e(q)) \\ &= \delta_D^{(1)}(p - p') + \frac{\partial \delta_D^{(1)}(p - p')}{\partial p'} (E_e(q') - E_e(q)), \end{aligned} \quad (2.63)$$

where $E_e(q') - E_e(q)$ is:

$$E_e(q') - E_e(q) \simeq \frac{(\vec{p}' - \vec{p}') \cdot \vec{q}}{m_e}. \quad (2.64)$$

Since the collision is elastic in the non-relativistic Compton scattering, we ignore the first term, which means $\vec{p}' \simeq \vec{p}$. In addition, $f_e(\vec{q} + \vec{p}' - \vec{p}')$ becomes $f_e(\vec{q})$. Substituting Eqs (2.63) and (2.64) into Eq. (2.62), and integrating with respect to q , we obtain

$$\begin{aligned} C[f(\vec{p})] &= \frac{n_e}{2} \frac{\pi}{8m_e^2 p} \int \frac{d^3 p'}{(2\pi)^3 p'} \sum_{\text{spins}} |\mathcal{M}|^2 \\ &\times \left(\delta^{(1)}(p - p') + (\vec{p}' - \vec{p}') \cdot \vec{v}_b \frac{\partial \delta_D^{(1)}(p - p')}{\partial p'} \right) (f(\vec{p}') - f(\vec{p})), \end{aligned} \quad (2.65)$$

where \vec{v}_b is the bulk velocity of the electrons. We expand photon distribution as in Eq. (2.57):

$$\begin{aligned} C[f(\vec{p})] &= \frac{n_e \pi}{16m_e^2 p} \int \frac{d^3 p'}{(2\pi)^3 p'} \sum_{\text{spins}} |\mathcal{M}|^2 \left(\delta_D^{(1)}(p - p') + (\vec{p}' - \vec{p}') \cdot \vec{v}_b \frac{\partial \delta_D^{(1)}(p - p')}{\partial p'} \right) \\ &\times \left(\left(f(p', T) - p' \frac{\partial f}{\partial p'} \Theta \right) - \left(f(p, T) - p \frac{\partial f}{\partial p} \Theta \right) \right) \\ &\simeq \frac{n_e}{96\pi^2 m_e^2 p} \int_0^\infty dp' p' \int d\Omega' \sum_{\text{spins}} |\mathcal{M}|^2 \left(\delta_D^{(1)}(p - p') \left(-p' \frac{\partial f}{\partial p'} \Theta + p \frac{\partial f}{\partial p} \Theta \right) \right. \\ &\left. + (\vec{p}' - \vec{p}') \cdot \vec{v}_b \frac{\partial \delta_D^{(1)}(p - p')}{\partial p'} (f(p', T) - f(p, T)) \right). \end{aligned} \quad (2.66)$$

To describe the solid angle, we need to define the angle between the wavenumber \vec{k} and the photon direction \hat{p} :

$$\mu \equiv \frac{\vec{k} \cdot \hat{p}}{k}, \quad (2.67)$$

where the wavenumber \vec{k} comes from the Fourier transform of the photon's spatial position:

$$f(\vec{x}) = \int \frac{d^3 k}{(2\pi)^3} e^{i\vec{k} \cdot \vec{x}} f(\vec{k}) \quad (2.68)$$

Usually, we assume that the velocities are longitudinal ($\nabla \times \vec{v}_b = 0$):

$$\vec{v}_b(\vec{k}) = \frac{\vec{k}}{k} v_b(\vec{k}) \quad (2.69)$$

The amplitude squared for Compton scattering is:

$$\sum_{\text{spins}} |\mathcal{M}|^2 = 24\pi\sigma_{\text{T}}m_e^2 \left(1 + [\hat{p} \cdot \hat{p}']^2\right) \quad (2.70)$$

We expand the amplitude by the Legendre polynomial $P_l(\mu)$ and integrate with respect to p' , leading the collision term to (Dodelson & Schmidt, 2020):

$$C[f(\vec{p})] = -p \frac{\partial f}{\partial p} n_e \sigma_{\text{T}} \left(\Theta_0 - \Theta + \mu v_b - \frac{1}{2} P_2(\mu) \Theta_2 \right) \quad (2.71)$$

We define the multipole moment of the temperature field as:

$$\Theta_l(k) \equiv \frac{1}{(-i)^l} \int_{-1}^1 \frac{d\mu}{2} P_l(\mu) \Theta(\mu, k), \quad (2.72)$$

In addition, we define the optical depth as (Fukugita, 2003):

$$\tau(\eta) \equiv \int_{\eta}^{\eta_0} d\eta n_e \sigma_{\text{T}} a, \quad (2.73)$$

where η is the conformal time. Using the Fourier transform of Eq. (2.59), and changing t to η , we obtain the Boltzmann equation for photons:

$$\Theta' = -ik\mu(\Theta + \Psi) - \Phi' - \tau' \left(\Theta_0 - \Theta + \mu v_b - \frac{1}{2} P_2(\mu) \Theta_2 \right), \quad (2.74)$$

where $' \equiv d/d\eta$. Besides, if we consider the contribution from polarization, then Eq. (2.74) becomes (Dodelson & Schmidt, 2020):

$$\Theta' = -ik\mu(\Theta + \Psi) - \Phi' - \tau' \left(\Theta_0 - \Theta + \mu v_b - \frac{1}{2} P_2(\mu) \Pi \right), \quad (2.75)$$

where

$$\Pi = \Theta_2 + \Theta_{P2} + \Theta_{P0} \quad (2.76)$$

2.2.3 CMB anisotropy

Line-of-sight integral

To get the presently observed anisotropy, we perform the line-of-sight integration over Eq. (2.74):

$$\Theta(\vec{k}, \eta_0) = \int_0^{\eta_0} e^{-\tau + ik\mu(\eta - \eta_0)} S d\eta, \quad (2.77)$$

where S is the source function:

$$S(\vec{k}, \eta) \equiv -\Phi' - ik\mu\Psi - \tau' \left(\Theta_0 + \mu v_b - \frac{1}{2} P_2(\mu) \Theta_2 \right) \quad (2.78)$$

By using the spherical harmonics to decompose Eq. (2.77), we obtain (Lyth & Liddle, 2009):

$$\begin{aligned} \Theta_l(\vec{k}, \eta_0) &= \int_0^{\eta_0} d\eta g(\eta) \left((\Theta_0 + \Psi) j_l(k(\eta_0 - \eta)) - i v_b \frac{d j_l(k(\eta_0 - \eta))}{d(k\eta)} \right. \\ &\quad \left. + \frac{\Theta_2}{4} \left(3 \frac{d^2 j_l(k(\eta_0 - \eta))}{d(k\eta)^2} + j_l(k(\eta_0 - \eta)) \right) \right) \\ &\quad + \int_0^{\eta_0} d\eta e^{-\tau} (\Psi' - \Phi') j_l(k(\eta_0 - \eta)), \end{aligned} \quad (2.79)$$

where j_l is the spherical Bessel function:

$$j_l(k(\eta - \eta_0)) = (-i)^l \int_{-1}^1 \frac{d\mu}{2} P_l(\mu) e^{ik\mu(\eta - \eta_0)}. \quad (2.80)$$

In addition, we define the visibility function $g(\eta)$:

$$g(\eta) \equiv -\tau' e^{-\tau}. \quad (2.81)$$

CMB angular power spectrum

We use the spherical harmonics to expand Θ :

$$\Theta(\vec{x}, \hat{p}, \eta) = \sum_{l=0}^{\infty} \sum_{m=-l}^l a_{lm}(\vec{x}, \eta) Y_{lm}(\hat{p}) \quad (2.82)$$

Due to the stochastic properties of CMB, a_{lm} follows the Gaussian distribution whose variance is C_l :

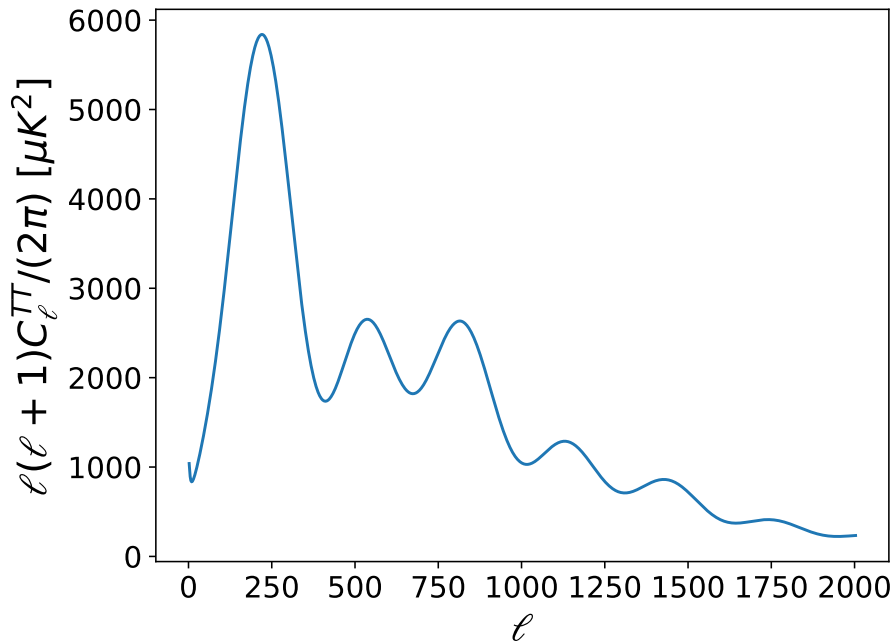
$$\begin{aligned} \langle a_{lm} \rangle &= 0, \\ \langle a_{lm} a_{l'm'}^* \rangle &= \delta_{ll'} \delta_{mm'} C_l. \end{aligned} \quad (2.83)$$

From Eq. (2.82), the two point correlation becomes (Baumann, 2022):

$$\begin{aligned} \langle \Theta(\hat{p}) \Theta(\hat{p}') \rangle &= \sum_{lm} \sum_{l'm'} \langle a_{lm} a_{l'm'}^* \rangle Y_{lm}(\hat{p}) Y_{l'm'}^*(\hat{p}') \\ &= \sum_l \frac{2l+1}{4\pi} C_l P_l(\hat{p} \cdot \hat{p}'). \end{aligned} \quad (2.84)$$

If we set $\hat{p} \cdot \hat{p}' = \theta$, we can write C_l as:

$$C_l = 2\pi \int_{-1}^1 d\theta \langle \Theta(\hat{p}) \Theta(\hat{p}') \rangle P_l(\theta). \quad (2.85)$$

Figure 2.1: One example of C_l .

We define T as (Dodelson & Schmidt, 2020):

$$T \equiv \frac{\Theta(\vec{k}, \hat{p}, \eta_0)}{R(\vec{k})}, \quad (2.86)$$

where R is the curvature perturbation, representing the initial condition given by the inflation:

$$\langle R(\vec{k})R^*(\vec{k}') \rangle = P_R(\vec{k})(2\pi)^3 \delta_D^{(3)}(\vec{k} - \vec{k}') \quad (2.87)$$

Therefore, C_l can be written:

$$C_l = \frac{2}{\pi} \int_0^\infty dk k^2 P_R(k) |T_l(k)|^2, \quad (2.88)$$

where $T_l(k)$ is T decomposed by the Legendre polynomial. One example of C_l is shown in Fig. 2.1.

2.3 Polarization

2.3.1 CMB E mode and B mode

The polarization is usually described by the Stokes parameters (Komatsu, 2022):

$$\begin{aligned} Q &= |E_x|^2 - |E_y|^2 \\ U &= 2\text{Re}(E_x^* E_y), \end{aligned} \quad (2.89)$$

where E_x and E_y are components of an electric field \vec{E} . If we rotate the x- and y-axes counter-clockwise by an angle ϕ , the Stokes parameters will be come (Baumann, 2022):

$$\begin{bmatrix} Q' \\ U' \end{bmatrix} = \begin{bmatrix} \cos 2\phi & \sin 2\phi \\ -\sin 2\phi & \cos 2\phi \end{bmatrix} \begin{bmatrix} Q \\ U \end{bmatrix}, \quad (2.90)$$

and it can be written in a compact form:

$$Q' \pm iU' = e^{\mp 2i\phi}(Q \pm iU), \quad (2.91)$$

showing that polarization transforms like a spin-2 field. Therefore, we can use spin-weighted spherical harmonics to describe its decomposition into multipole moments (Zaldarriaga & Seljak, 1997; Kamionkowski et al., 1997b):

$$Q(\hat{n}) \pm iU(\hat{n}) = \sum_{lm} a_{\pm 2, lm} {}_{\pm 2}Y_{lm}(\hat{n}), \quad (2.92)$$

where \hat{n} is the observed direction and $\hat{n} = (\sin \theta \cos \phi, \sin \theta \sin \phi, \cos \theta)$. The relationship between ${}_{\pm 2}Y_{lm}$ and Y_{lm} is (Hu & White, 1997)

$${}_{\pm 2}Y_{lm} = \left(\frac{(l-2)!}{(l+2)!} \right)^{1/2} \left(\partial_\theta^2 - \cot \theta \partial_\theta \pm \frac{2i}{\sin \theta} (\partial_\theta - \cot \theta) \partial_\phi - \frac{1}{\sin^2 \theta} \partial_\phi^2 \right) Y_{lm} \quad (2.93)$$

To derive this, we need a pair of operators, \eth and $\bar{\eth}$. They are spin raising and lowering operators (Zaldarriaga & Seljak, 1997; Lin & Wandelt, 2006):

$$\begin{aligned} (\eth_s f)' &= \exp(-i(s+1)\phi) (\eth_s f) \\ (\bar{\eth}_s f)' &= \exp(-i(s-1)\phi) (\bar{\eth}_s f) \end{aligned} \quad (2.94)$$

In addition, the form of operators is:

$$\begin{aligned} \eth_s f(\theta, \phi) &= -\sin^s \theta \left(\partial_\theta + \frac{i}{\sin \theta} \partial_\phi \right) \sin^{-s} \theta_s f(\theta, \phi) \\ \bar{\eth}_s f(\theta, \phi) &= -\sin^{-s} \theta \left(\partial_\theta - \frac{i}{\sin \theta} \partial_\phi \right) \sin^s \theta_s f(\theta, \phi) \end{aligned} \quad (2.95)$$

We define CMB E and B modes as:

$$a_{\pm 2, lm} \equiv -(E_{lm} \pm iB_{lm}), \quad (2.96)$$

and thus:

$$\begin{aligned} E_{lm} &= -(a_{2, lm} + a_{-2, lm})/2 \\ B_{lm} &= -(a_{2, lm} - a_{-2, lm})/2i, \end{aligned} \quad (2.97)$$

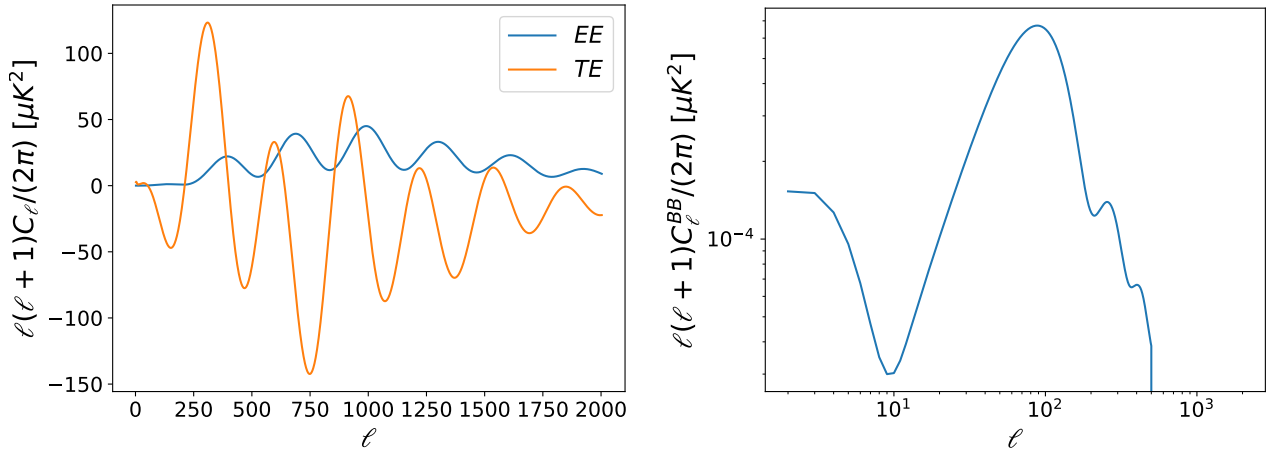


Figure 2.2: Examples of C_l^{EE} , C_l^{TE} (left) and C_l^{BB} (right). Here we set $r = 0.01$.

which shows E -mode is parity-even and B -mode is parity-odd. The polarization power spectra are written as:

$$\begin{aligned}
 \langle a_{lm} E_{l'm'}^* \rangle &= C_l^{TE} \delta_{ll'} \delta_{mm'} \\
 \langle E_{lm} E_{l'm'}^* \rangle &= C_l^{EE} \delta_{ll'} \delta_{mm'} \\
 \langle B_{lm} B_{l'm'}^* \rangle &= C_l^{BB} \delta_{ll'} \delta_{mm'} \\
 \langle a_{lm} B_{l'm'}^* \rangle &= C_l^{TB} \delta_{ll'} \delta_{mm'} \\
 \langle E_{lm} B_{l'm'}^* \rangle &= C_l^{EB} \delta_{ll'} \delta_{mm'}
 \end{aligned} \tag{2.98}$$

If the primordial universe is parity conserving, then $C_l^{TB} = C_l^{EB} = 0$. We show examples for C_l^{TE} , C_l^{EE} and C_l^{BB} in Fig. 2.2. We use two spin-0 quantities $\tilde{E}(\hat{n})$ and $\tilde{B}(\hat{n})$ (Zaldarriaga & Seljak, 1997; Lin & Wandelt, 2006):

$$\begin{aligned}
 \tilde{E}(\hat{n}) &\equiv \frac{-1}{2} (\bar{\partial}^2 (Q + iU)(\hat{n}) + \partial^2 (Q - iU)(\hat{n})) \\
 &= \sum_{l,m} \left(\frac{(l+2)!}{(l-2)!} \right)^{1/2} a_{E,lm} Y_{lm}(\hat{n})
 \end{aligned} \tag{2.99}$$

$$\begin{aligned}
 \tilde{B}(\hat{n}) &\equiv \frac{-1}{2i} (\bar{\partial}^2 (Q + iU)(\hat{n}) - \partial^2 (Q - iU)(\hat{n})) \\
 &= \sum_{l,m} \left(\frac{(l+2)!}{(l-2)!} \right)^{1/2} a_{B,lm} Y_{lm}(\hat{n})
 \end{aligned} \tag{2.100}$$

2.3.2 Generation of CMB polarization

Scalar perturbation

The polarization generated from the scalar perturbation has a similar form to Eq. (2.74), which can be written as

$$\Theta_P^{\prime s} + ik\mu\Theta_P^s = C, \quad (2.101)$$

where Θ_P^s is the anisotropy of polarization distribution from scalar perturbation and $\Theta_P^s \equiv \Theta_Q^s + i\Theta_U^s$. The only difference is that the gravitational potentials do not appear here because gravity cannot directly generate the polarization and the gravitational effects are all in the collision term.

The Boltzmann equation for the polarization generated by scalar perturbation is given by (Bond & Efstathiou, 1984; Ma & Bertschinger, 1995):

$$\Theta_P^{\prime s} + ik\mu\Theta_P^s = -\tau' \left(-\Theta_P^s + \frac{3}{4} (1 - \mu^2) \Pi \right), \quad (2.102)$$

where

$$\Pi \equiv \Theta_2 + \Theta_{P2}^s + \Theta_{P0}^s. \quad (2.103)$$

Then the line-of-sight integration is:

$$\Theta_P^s(k, \mu) = \int_0^{\eta_0} d\eta e^{ik\mu(\eta-\eta_0)-\tau(\eta)} \left(-\frac{3}{4}\tau' (1 - \mu^2) \Pi \right) \quad (2.104)$$

Then we use the visibility function to write this equation:

$$\Theta_P^s(k, \mu) = \frac{3}{4}(1 - \mu^2) \int_0^{\eta_0} d\eta g(\eta) e^{ik\mu(\eta-\eta_0)} \Pi \quad (2.105)$$

Therefore, from Eq. (2.99), we derive Θ_E^s (Zaldarriaga & Seljak, 1997; Lin & Wandelt, 2006):

$$\begin{aligned} \Theta_E^s(k, \mu) &= \frac{-1}{2} (\bar{\partial}\Theta_P^s(k, \mu) + \bar{\partial}\Theta_P^{s*}(k, \mu)) \\ &= \frac{-3}{4} \int_0^{\eta_0} d\eta g(\eta) \Pi \partial_\mu^2 \left((1 - \mu^2)^2 e^{ik\mu(\eta-\eta_0)} \right), \end{aligned} \quad (2.106)$$

and Θ_B^s :

$$\begin{aligned} \Theta_B^s(k, \mu) &= \frac{-1}{2i} (\bar{\partial}\Theta_P^s(k, \mu) - \bar{\partial}\Theta_P^{s*}(k, \mu)) \\ &= 0, \end{aligned} \quad (2.107)$$

which means the scalar perturbation only generates E-mode polarization. Similar to Eq. (2.86), we define T^E as:

$$T^E \equiv \frac{\Theta_E^s(k)}{R(\vec{k})}. \quad (2.108)$$

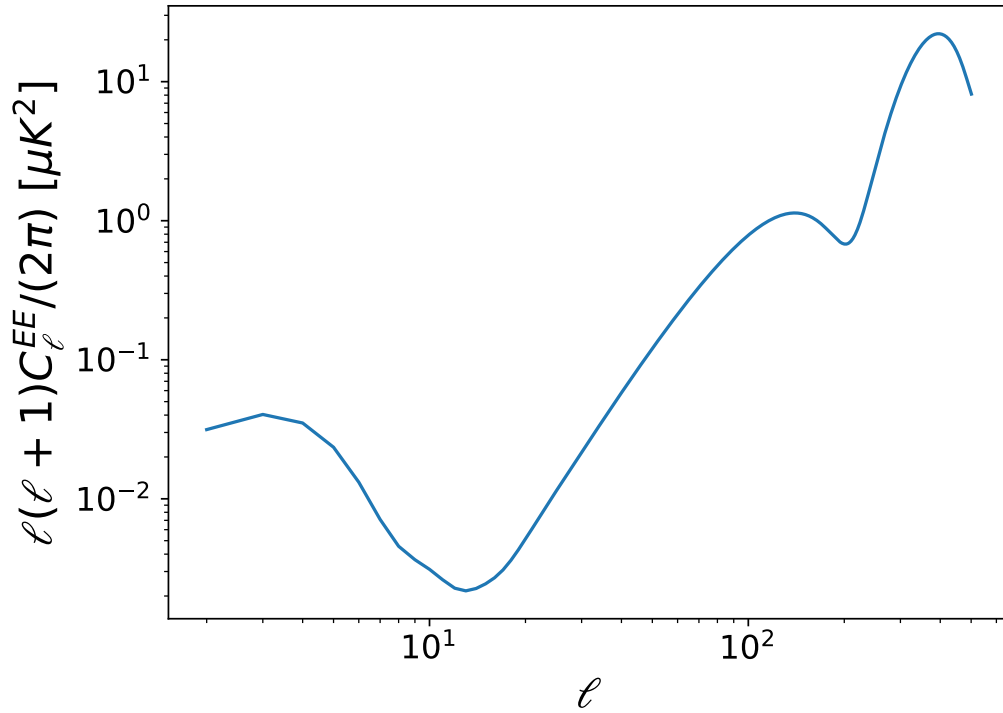


Figure 2.3: One example of the polarization generated by the scalar perturbation. The scalar perturbation only generates the E-mode polarization.

Therefore the EE power spectrum from scalar perturbation becomes:

$$C_l^{EE,s} = \frac{2}{\pi} \int_0^\infty dk k^2 |T_l^E(k)|^2 P_R(k) \quad (2.109)$$

One example of the polarization generated by the scalar perturbation is shown in Fig. 2.3.

Tensor perturbation

Tensor perturbations can be written as a divergenceless, traceless, symmetric matrix:

$$h_{ij}^{TT} = \begin{bmatrix} h_+ & h_\times & 0 \\ h_\times & -h_+ & 0 \\ 0 & 0 & 0 \end{bmatrix}, \quad (2.110)$$

where we choose the perturbations to be in the $x - y$ plane. According to Zaldarriaga & Seljak (1997), we define:

$$\begin{aligned} h_1 &= (h_+ - ih_\times)/\sqrt{2} \\ h_2 &= (h_+ + ih_\times)/\sqrt{2} \end{aligned} \quad (2.111)$$

The temperature and polarization from the tensor perturbation are written by (Polnarev, 1985; Crittenden et al., 1993; Zaldarriaga & Seljak, 1997; Lin & Wandelt, 2006):

$$\begin{aligned}\Theta_T^t(\vec{k}, \mu) &= \left((1 - \mu^2) e^{2i\phi} h_1(\vec{k}) + (1 - \mu^2) e^{-2i\phi} h_2(\vec{k}) \right) \tilde{\Theta}_T^t(k, \mu) \\ \Theta_P^t(\vec{k}, \mu) &= \left((1 - \mu)^2 e^{2i\phi} h_1(\vec{k}) + (1 + \mu)^2 e^{-2i\phi} h_2(\vec{k}) \right) \tilde{\Theta}_P^t(k, \mu),\end{aligned}\quad (2.112)$$

where $\vec{k} \parallel \hat{z}$. $\tilde{\Theta}_T^t$ and $\tilde{\Theta}_P^t$ satisfies the Boltzmann equation (Crittenden et al., 1993):

$$\begin{aligned}\tilde{\Theta}_T^t + ik\mu\tilde{\Theta}_T^t &= -h' - \tau' \left(\tilde{\Theta}_T^t - \frac{1}{10}\tilde{\Theta}_{T0}^t - \frac{1}{7}\tilde{\Theta}_{T2}^t - \frac{3}{70}\tilde{\Theta}_{T4}^t + \frac{3}{5}\tilde{\Theta}_{P0}^t - \frac{6}{7}\tilde{\Theta}_{P2}^t + \frac{3}{70}\tilde{\Theta}_{P4}^t \right) \\ \tilde{\Theta}_P^t + ik\mu\tilde{\Theta}_P^t &= -\tau' \left(\tilde{\Theta}_P^t + \frac{1}{10}\tilde{\Theta}_{T0}^t + \frac{1}{7}\tilde{\Theta}_{T2}^t + \frac{3}{70}\tilde{\Theta}_{T4}^t - \frac{3}{5}\tilde{\Theta}_{P0}^t + \frac{6}{7}\tilde{\Theta}_{P2}^t - \frac{3}{70}\tilde{\Theta}_{P4}^t \right),\end{aligned}\quad (2.113)$$

where we assume unpolarized gravitational waves and h is given by

$$\dot{h} = \frac{\dot{h}_+}{\sqrt{2}h_+} = \frac{\dot{h}_-}{\sqrt{2}h_-} \quad (2.114)$$

Then, the line-of-sight integration becomes (Zaldarriaga & Seljak, 1997; Lin & Wandelt, 2006):

$$\begin{aligned}\Theta_T^t(\vec{k}, \mu) &= \left((1 - \mu^2) e^{2i\phi} h_1(\vec{k}) + (1 - \mu^2) e^{-2i\phi} h_2(\vec{k}) \right) \int_0^{\eta_0} d\eta e^{ik\mu(\eta-\eta_0)} S_T^t(\eta, k) \\ \Theta_P^t(\vec{k}, \mu) &= \left((1 - \mu)^2 e^{2i\phi} h_1(\vec{k}) + (1 + \mu)^2 e^{-2i\phi} h_2(\vec{k}) \right) \int_0^{\eta_0} d\eta e^{ik\mu(\eta-\eta_0)} S_P^t(\eta, k),\end{aligned}\quad (2.115)$$

where

$$\begin{aligned}S_T^t(\eta, k) &= -h'e^{-\tau} + g \left(\frac{1}{10}\tilde{\Theta}_{T0}^t + \frac{1}{7}\tilde{\Theta}_{T2}^t + \frac{3}{70}\tilde{\Theta}_{T4}^t - \frac{3}{5}\tilde{\Theta}_{P0}^t + \frac{6}{7}\tilde{\Theta}_{P2}^t - \frac{3}{70}\tilde{\Theta}_{P4}^t \right), \\ S_P^t(\eta, k) &= -g \left(\frac{1}{10}\tilde{\Theta}_{T0}^t + \frac{1}{7}\tilde{\Theta}_{T2}^t + \frac{3}{70}\tilde{\Theta}_{T4}^t - \frac{3}{5}\tilde{\Theta}_{P0}^t + \frac{6}{7}\tilde{\Theta}_{P2}^t - \frac{3}{70}\tilde{\Theta}_{P4}^t \right).\end{aligned}\quad (2.116)$$

Substituting Eq. (2.116) into Eqs. (2.99) and (2.100), we find (Zaldarriaga & Seljak, 1997; Lin & Wandelt, 2006):

$$\begin{aligned}\Theta_E^t(\vec{k}, \mu) &= \frac{-1}{2} \left(\tilde{\partial}\Theta_P^s(k, \mu) + \tilde{\partial}\Theta_P^{s*}(k, \mu) \right) \\ &= (1 - \mu^2) \left(e^{2i\phi} h_1(\vec{k}) + e^{-2i\phi} h_2(\vec{k}) \right) \left(-12 + x^2(1 - \partial_x^2) - 8x\partial_x \right) \int_0^{\eta_0} d\eta e^{-ix\mu} S_P^t(\eta, k) \\ \Theta_B^t(\vec{k}, \mu) &= \frac{-1}{2i} \left(\tilde{\partial}\Theta_P^s(k, \mu) - \tilde{\partial}\Theta_P^{s*}(k, \mu) \right) \\ &= -(1 - \mu^2) \left(e^{2i\phi} h_1(\vec{k}) - e^{-2i\phi} h_2(\vec{k}) \right) \left(8x + 2x^2\partial_x \right) \int_0^{\eta_0} d\eta e^{-ix\mu} S_P^t(\eta, k),\end{aligned}\quad (2.117)$$

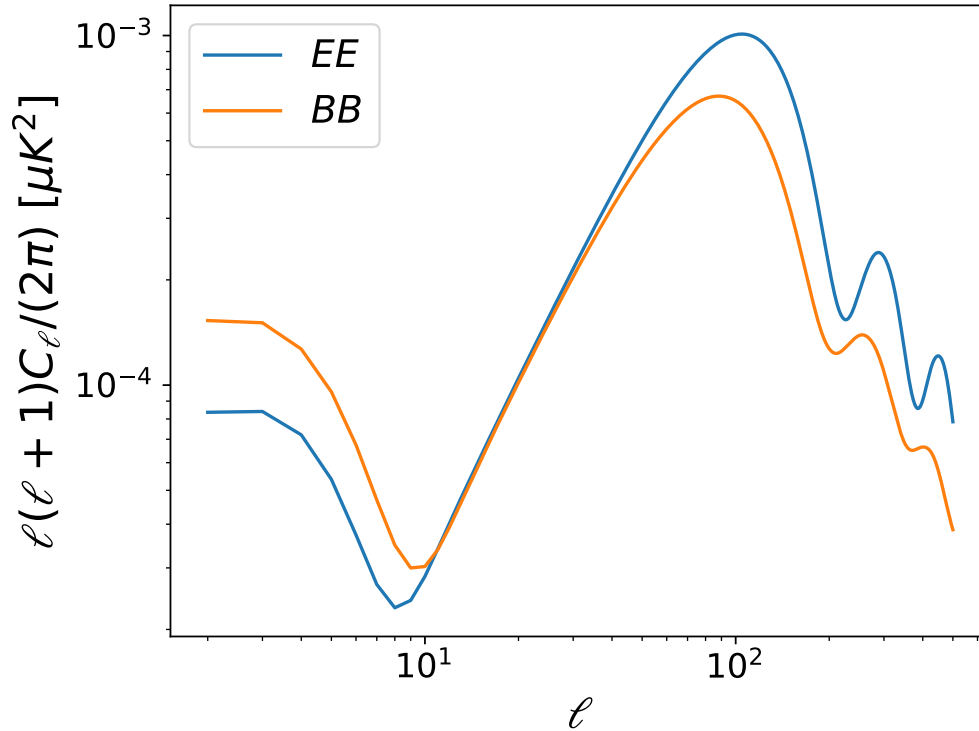


Figure 2.4: One example of the polarization generated by the tensor perturbation. Here we assume $r = 0.01$.

where $x = -k(\eta - \eta_0)$. Similar to Eq. (2.109), the power spectra for tensor perturbation are:

$$C_l^{EE,t} = \frac{2}{\pi} \int_0^\infty dk k^2 |T_l^{E,t}(k)|^2 P_T(k) \quad (2.118)$$

$$C_l^{BB,t} = \frac{2}{\pi} \int_0^\infty dk k^2 |T_l^{B,t}(k)|^2 P_T(k), \quad (2.119)$$

where T^t is the transfer function for tensor perturbation

$$T^{E,t} \equiv \frac{\Theta_E^t(k)}{2h_1} \quad (2.120)$$

$$T^{B,t} \equiv \frac{\Theta_B^t(k)}{2h_1}, \quad (2.121)$$

and P_T is the total tensor power spectrum which will be discussed later. One example of the polarization generated by the tensor perturbation is shown in Fig. 2.4.

2.3.3 Inflationary gravitational waves

The evolution of gravitational waves

To solve Eq. (2.113), we need to derive the evolution of gravitational waves. To get it, we need to substitute the metric perturbation (2.110) into Eq. (2.1). Under this situation, the

Christoffel symbol is (Dodelson & Schmidt, 2020):

$$\begin{aligned}
\Gamma_{00}^0 &= \Gamma_{i0}^0 = 0 \\
\Gamma_{ij}^0 &= Hg_{ij} + \frac{a^2 h_{ij,0}^{TT}}{2} \\
\Gamma_{0j}^i &= H\delta_{ij} + \frac{1}{2} h_{ij,0}^{TT} \\
\Gamma_{jk}^i &= \frac{i}{2} (k_k h_{ij}^{TT} + k_j h_{ij}^{TT} - k_i h_{jk}^{TT})
\end{aligned} \tag{2.122}$$

Then the Ricci tensor becomes (Dodelson & Schmidt, 2020):

$$\begin{aligned}
R_{ij} &= \Gamma_{ij,\alpha}^\alpha - \Gamma_{i\alpha,j}^\alpha + \Gamma_{\alpha\beta}^\alpha \Gamma_{ij}^\beta - \Gamma_{\beta j}^\alpha \Gamma_{i\alpha}^\beta \\
&= g_{ij} \left(\frac{\ddot{a}}{a} + 2H^2 \right) + \frac{3}{2} a^2 H h_{ij,0}^{TT} + a^2 \frac{h_{ij,00}^{TT}}{2} + \frac{k^2}{2} h_{ij}^{TT}.
\end{aligned} \tag{2.123}$$

From $R = g^{00} R_{00} + G^{ij} R_{ij}$, and the equation above, we know that the first-order Ricci scalar is 0. Therefore, the first-order Einstein equation for gravitational waves is:

$$a^2 \square h_{ij}^{TT} = -16\pi G T_{ij}^{GW}, \tag{2.124}$$

where \square is:

$$\square = -\frac{\partial^2}{\partial t^2} - 3\frac{\dot{a}}{a} \frac{\partial}{\partial t} + \frac{1}{a^2} \nabla^2, \tag{2.125}$$

and T_{ij}^{GW} is the traceless and transverse part of the anisotropic stress.

Inflation

At the time of CMB ($z \simeq 1100$), the observable universe was remarkably uniform. The problem is that different regions of the universe observed in the map of CMB were too distant from each other to have been in causal contact by the time of recombination. If our entire observable universe originated from a single early causal patch and experienced an epoch of early acceleration, this would resolve the issue. This epoch is called inflation.

The comoving Hubble radius decreased while the universe underwent accelerated expansion:

$$\frac{d}{dt} (aH)^{-1} = -\frac{\ddot{a}}{(\dot{a})^2} < 0 \tag{2.126}$$

Here we define the slow-roll parameter as (Baumann, 2022):

$$\frac{d}{dt} (aH)^{-1} = -\frac{\dot{a}H + a\dot{H}}{(aH)^2} = -\frac{1}{a}(1 - \epsilon), \tag{2.127}$$

where

$$\epsilon \equiv -\frac{\dot{H}}{H^2} \tag{2.128}$$

From Eq. (2.126), ϵ satisfies:

$$\epsilon = -\frac{\dot{H}}{H^2} < 1 \quad (2.129)$$

In the limit $\epsilon \rightarrow 0$, the scale factor evolves exponentially:

$$a(t) = a_e e^{H(t-t_e)}, \quad t < t_e, \quad (2.130)$$

where t_e denotes the time at the end of inflation and a_e is the scale factor at that point.

To end inflation and transition to a radiation-dominated universe, the simplest approach is to introduce a scalar field ϕ to govern the inflation process. The energy-momentum tensor for ϕ is (Dodelson & Schmidt, 2020):

$$T_{\beta}^{\alpha} = g^{\alpha\nu} \frac{\partial\phi}{\partial x^{\nu}} \frac{\partial\phi}{\partial x^{\beta}} - \delta_{\beta}^{\alpha} \left(\frac{1}{2} g^{\mu\nu} \frac{\partial\phi}{\partial x^{\mu}} \frac{\partial\phi}{\partial x^{\nu}} + V(\phi) \right) \quad (2.131)$$

Therefore, ρ and P are obtained as:

$$\rho = T_0^0 = \frac{1}{2} \dot{\phi}^2 + V(\phi) \quad (2.132)$$

$$P = T_i^i = \frac{1}{2} \dot{\phi}^2 - V(\phi) \quad (2.133)$$

By substituting them into Eq. (2.23), we obtain

$$\ddot{\phi} + 3H\dot{\phi} + V_{,\phi} = 0, \quad (2.134)$$

which is called the Klein-Gordon equation. $V_{,\phi}$ is $\partial V / \partial \phi$. By putting ρ and P into Eq. (2.20), we obtain:

$$H^2 = \frac{8\pi G}{3} \left(\frac{1}{2} \dot{\phi}^2 + V \right) \quad (2.135)$$

Therefore,

$$\dot{H} = -4\pi G \dot{\phi}^2 \quad (2.136)$$

In the slow-roll approximation (Baumann, 2022):

$$\frac{1}{2} \dot{\phi}^2 \ll V \quad (2.137)$$

$$|\ddot{\phi}| \ll |H\dot{\phi}| \quad (2.138)$$

Then the Friedmann equation (2.135) is:

$$H \approx \frac{8\pi G}{3} V, \quad (2.139)$$

and the Klein-Gordon equation (2.134) is:

$$3H\dot{\phi} \approx -V_{,\phi} \quad (2.140)$$

Therefore, the slow-roll parameter is:

$$\epsilon = -\frac{\dot{H}}{H^2} = \frac{4\pi G \dot{\phi}^2}{H^2} \approx \frac{1}{16\pi G} \left(\frac{V_{,\phi}}{V} \right)^2 \quad (2.141)$$

Gravitational wave production

During inflation, the perturbation is generated by the quantum fluctuation, which means the average fluctuation is zero but the average square of the fluctuations is not zero and it is called variance. The variance sets the initial conditions.

For gravitational waves, well before horizon entry, the traceless and transverse part of the anisotropic stress, T_{ij}^{GW} , is supposed to vanish. Therefore the right-hand-side of Eq. (2.124) is equal to 0. In addition, we transform the derivative with respect to t to the derivative with respect to η so that Eq. (2.124) becomes:

$$h'' + 2\frac{a'}{a}h' + k^2h = 0, \quad (2.142)$$

where h is h_+ or h_\times . According to Dodelson & Schmidt (2020), we define:

$$\mathfrak{h} \equiv \frac{ah}{\sqrt{16\pi G}} \quad (2.143)$$

By substituting it Eq. (2.142), we get (Dodelson & Schmidt, 2020):

$$\frac{1}{a} \left(\mathfrak{h}'' + \left(k^2 - \frac{a''}{a} \right) \mathfrak{h} \right) = 0 \quad (2.144)$$

This form is similar to the evolution of a harmonic oscillator so that we can quantize it as (Dodelson & Schmidt, 2020):

$$\hat{\mathfrak{h}}(\vec{k}, \eta) = v(k, \eta)\hat{a}_{\vec{k}} + v^*(k, \eta)\hat{a}_{\vec{k}}^\dagger, \quad (2.145)$$

where v satisfies:

$$v'' + \left(k^2 - \frac{a''}{a} \right) v = 0 \quad (2.146)$$

Since

$$\frac{a''}{a} \simeq -\frac{1}{a} \frac{d}{d\eta} \left(\frac{a}{\eta} \right) \simeq \frac{2}{\eta^2}, \quad (2.147)$$

Eq. (2.146) becomes:

$$v'' + \left(k^2 - \frac{2}{\eta} \right) v = 0 \quad (2.148)$$

The solution is (Dodelson & Schmidt, 2020):

$$v = \frac{e^{-ik\eta}}{\sqrt{2k}} \left(1 - \frac{i}{k\eta} \right). \quad (2.149)$$

The variance is

$$\begin{aligned}\langle \hat{h}^\dagger(\vec{k}, \eta) \hat{h}(\vec{k}', \eta) \rangle &= \frac{16\pi G}{a^2} |v(k, \eta)|^2 (2\pi)^3 \delta_D^3(\vec{k} - \vec{k}') \\ &= \frac{16\pi G}{a^2} \frac{1}{2k^3 \eta^2} (2\pi)^3 \delta_D^3(\vec{k} - \vec{k}')\end{aligned}\quad (2.150)$$

We define the tensor power spectrum as:

$$\langle \hat{h}^\dagger(\vec{k}, \eta) \hat{h}(\vec{k}', \eta) \rangle \equiv P_h(k, \eta) (2\pi)^3 \delta_D^3(\vec{k} - \vec{k}') \quad (2.151)$$

and dimensionless power spectrum as:

$$\Delta_h^2(k, \eta) \equiv \frac{k^3}{2\pi^2} P_h(k, \eta) \quad (2.152)$$

We define the total power spectrum as:

$$\langle h_{ij}^{TT}(\vec{k}, \eta) (h_{ij}^{TT})^*(\vec{k}', \eta) \rangle \equiv (2\pi)^3 \delta_D^3(\vec{k} - \vec{k}') P_T(k) \quad (2.153)$$

Since

$$\langle h_{ij}^{TT}(\vec{k}, \eta) (h_{ij}^{TT})^*(\vec{k}', \eta) \rangle = 2\langle h_+(\vec{k}, \eta) h_+(\vec{k}', \eta) \rangle + 2\langle h_\times(\vec{k}, \eta) h_\times(\vec{k}', \eta) \rangle, \quad (2.154)$$

P_T is then equal to $4P_h$. We can write it as the power law form:

$$P_T(k) \equiv 2\pi^2 A_T k^{-3} \left(\frac{k}{k_p} \right)^{n_T}, \quad (2.155)$$

where A_T is the tensor amplitude, n_T is the spectral index and k_p is the pivot scale.

Tensor-to-scalar ratio

For the scalar perturbation, the power spectrum of the gauge-invariant curvature perturbation R is given as (Dodelson & Schmidt, 2020):

$$P_R(k) = \frac{8\pi G H^2}{9k^3 \epsilon}, \quad (2.156)$$

and the dimensionless version is:

$$\Delta_R^2(k, \eta) \equiv \frac{k^3}{2\pi^2} P_R(k, \eta) \quad (2.157)$$

In addition, it can also be written in the power law form:

$$P_R(k) \equiv 2\pi^2 A_s k^{-3} \left(\frac{k}{k_p} \right)^{n_s - 1}. \quad (2.158)$$

Here, A_s represents the variance of curvature perturbations within a logarithmic interval of wavenumbers centered around the pivot scale k_p and n_s is the scalar spectral index. Then we

define the tensor-to-scalar ratio r as (Kamionkowski & Kovetz, 2016):

$$r \equiv \frac{\Delta_T^2}{\Delta_R^2} = \frac{A_T}{A_s} = 16\epsilon \quad (2.159)$$

By using Eq. (2.141),

$$r = \frac{1}{\pi G} \left(\frac{V_{,\phi}}{V} \right)^2 \quad (2.160)$$

Therefore, the observation of r can provide a constraint on the energy density of inflation.

2.4 Reionization

During the reionization epoch, since the UV light emitted by the first stars and galaxies ionized the neutral hydrogen in the IGM, a large number of free electrons were generated. Free electrons released during this epoch scatter CMB photons again.

Since the probability per unit time for a photon to scatter with an electron is $n_e\sigma_T$, the optical depth τ defined in Eq. (2.73) is the photon was scattered between η and η_0 . Because during dt , the probability that the photon was not scattered is $1 - \sigma_T n_e dt$, the photon traveled freely since time t is $P(t)$ which satisfies (Lyth & Liddle, 2009):

$$P(t) = \exp \left(- \int_t^{t_0} n_e \sigma_T dt \right) = e^{-\tau(t)}, \quad (2.161)$$

and

$$\frac{dP}{dt} = - \frac{d\tau}{dt} P = - \frac{d\tau}{dt} e^{-\tau} \equiv g(t) \quad (2.162)$$

Comparing with Eq. (2.81), we find

$$g(\eta) = ag(t), \quad (2.163)$$

and $g(t)$ is the visibility function with the variable t . From Eq. (2.162), we know that $g(t)dt$ is the probability that a CMB photon observed is currently scattered in the time interval dt at time t and has traveled freely since then. One example is shown in Fig. 2.5, where we can see two peaks. One peak is the hydrogen recombination and another corresponds to the time of reionization. Therefore, during the reionization epoch, fraction $e^{-\tau_{\text{re}}}$ of photons were not scattered and from the last scattering surface, while fraction $1 - e^{-\tau_{\text{re}}}$ of photons were from other direction and scattered into the line of sight, where τ_{re} is defined at the time of the end of the reionization. Therefore the temperature we observed is (Dodelson & Schmidt, 2020):

$$T(1 + \Theta)e^{-\tau_{\text{re}}} + T(1 - e^{-\tau_{\text{re}}}) = T(1 + \Theta e^{-\tau_{\text{re}}}), \quad (2.164)$$

where Θ is the temperature anisotropy. This only affects the small-scale temperature anisotropy (within the horizon size at rescattering). However, for the polarization, it is not the same. The polarization spectra are sensitive to the epoch of the last scattering (Hu & White, 1997). The location of the peak depends on the horizon size at the last scattering (Efstathiou, 1988). This

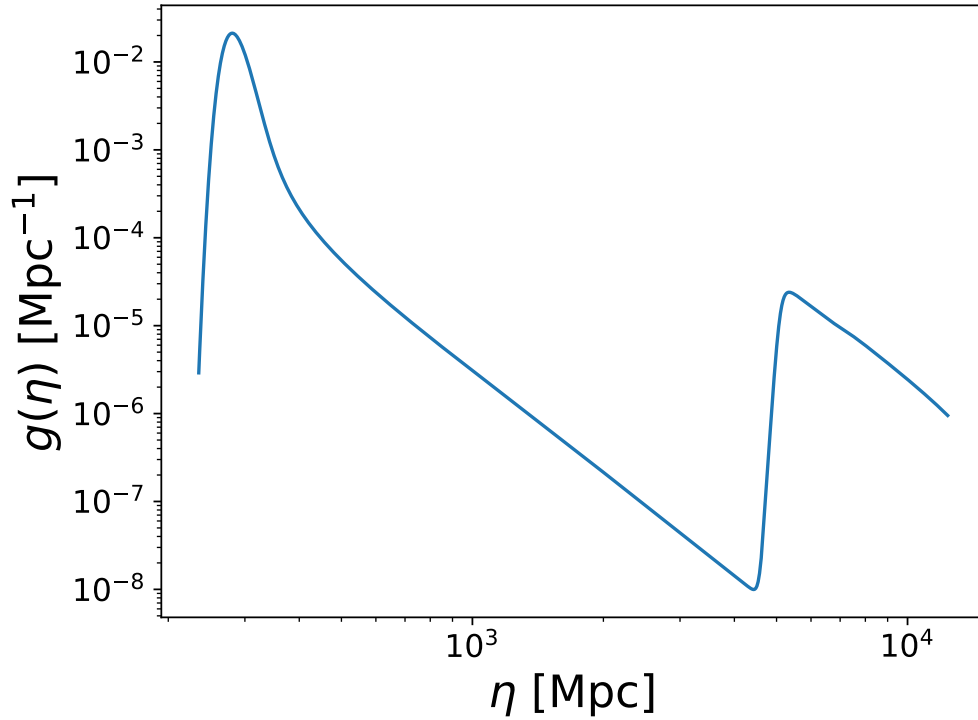


Figure 2.5: One example of the visibility function. The first peak is at the recombination epoch and the second peak is at the reionization epoch.

is because we can write Eq. (2.105) as (Zaldarriaga, 1997):

$$\Theta_P^s = \frac{3}{4}(1 - \mu^2) \left(\int_{\eta_{\text{reio}}}^{\eta_0} d\eta g(\eta) e^{ik\mu(\eta - \eta_0)} \Pi + \int_0^{\eta_{\text{reio}}} d\eta g(\eta) e^{ik\mu(\eta - \eta_0)} \Pi \right), \quad (2.165)$$

where η_{reio} is the conformal time of the start of reionization. Since $g(\eta)$ is a function with two peaks, we simplify Eq. (2.165) as:

$$\Theta_P^s \approx \frac{3}{4}(1 - \mu^2) \left(g(\eta_{\text{reio}}) e^{ik\mu(\eta_{\text{reio}} - \eta_0)} \Pi + g(\eta_{\text{rec}}) e^{ik\mu(\eta_{\text{rec}} - \eta_0)} \Pi \right). \quad (2.166)$$

In Π , defined in Eq. (2.76), the biggest contribution is from the quadrupole of the temperature anisotropy Θ_2 . For the electron, on a scale $\theta \sim 1/l$ is mainly from $k^{-1} \sim \theta \times (\text{distance to last scattering surface})$ (Dodelson & Schmidt, 2020). Therefore, at η_{reio} , the quadrupole ($l = 2$) observed by an electron is mainly contributed by $k^{-1} \sim 1/2(\eta_{\text{reio}} - \eta_{\text{rec}})$. Then the polarization we observe now generated from reionization is the scale $\theta \sim k^{-1}/(\eta_0 - \eta_{\text{reio}})$, so the position of the peak is:

$$l \sim 2 \frac{\eta_0 - \eta_{\text{reio}}}{\eta_{\text{reio}} - \eta_{\text{rec}}}, \quad (2.167)$$

which corresponds to the large scale. The case of the polarization generated by tensor perturbation is similar to the scalar perturbation case. Θ_P^t is mainly contributed by Θ_{T2}^t , so the position of the peak is similar to Eq. (2.167). On the other hand, the amplitude of the reionization depends on τ which is shown in Fig. 2.6. From them, we observe that higher τ makes the reionization bump much larger but only suppresses other bumps slightly.

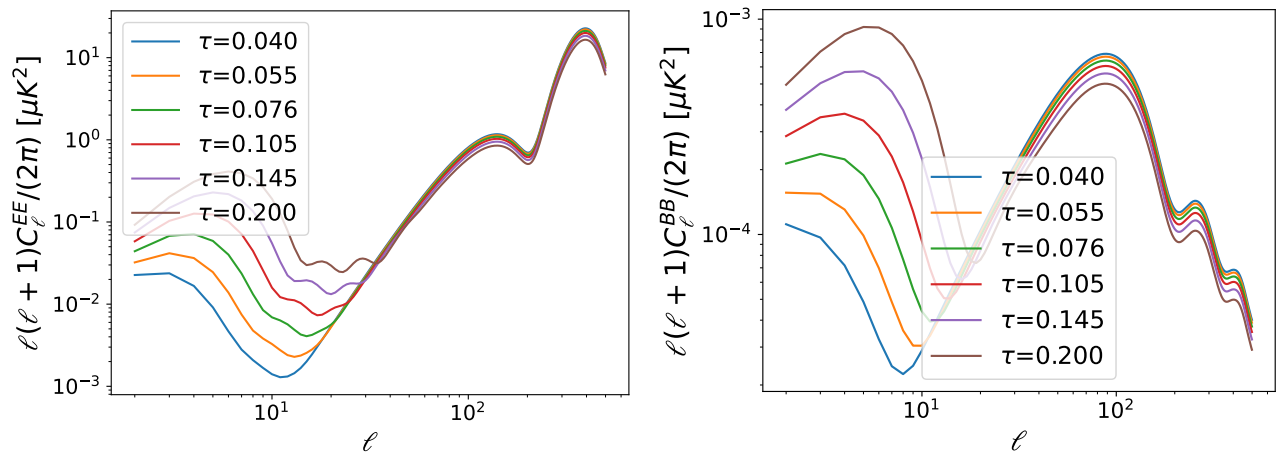


Figure 2.6: The dependence of reionization bump height on τ . The left figure is EE power spectra and the right figure is BB power spectra (assuming $r = 0.01$).

Chapter 3

Forecasting method and reionization models

3.1 Forecast method

3.1.1 χ^2

In this study, we want to use the maximum likelihood estimation method to estimate the best fit and the uncertainty of parameters we are interested in: the tensor-to-scalar ratio (r), representing the energy scale of the inflation models, and the z_{reio} measuring where the reionization fraction is half of its maximum. We fix other parameters based on the results from the Planck collaboration ¹. The likelihood $L(\hat{C}_l|C_l)$ follows the Wishart distribution (Katayama & Komatsu, 2011):

$$\chi_l^2 \equiv -2 \ln L(\hat{C}_l|C_l) = (2l + 1) \left(\frac{\hat{C}_l}{C_l} + \ln(C_l) - \frac{2l - 1}{2l + 1} \ln(\hat{C}_l) \right), \quad (3.1)$$

where \hat{C}_l is the power spectrum derived from the observation data, we used the CLASS package to simulate it here. The $C_l(r, z_{\text{reio}})$ is the power spectrum from the theory, parameterized by r and z_{reio} .

3.1.2 Fisher

Before calculating the uncertainty by χ^2 , we first estimate the uncertainty by the Fisher information matrix. The Fisher matrix is the curvature of the likelihood:

$$F_{ij} \equiv - \left\langle \frac{\partial^2 \ln L}{\partial p_i \partial p_j} \right\rangle \Big|_{\text{best fit}}, \quad (3.2)$$

¹https://wiki.cosmos.esa.int/planck-legacy-archive/images/b/be/Baseline_params_table_2018_68pc.pdf

Parameter	Description	Fiducial Value
r	Tensor-to-scalar ratio	0.01, 0.001
$\tau (z_{\text{reio}})$	Optical depth (Redshift at $x_e = 0.5$)	0.054 ($z_{\text{reio}} = 7.249$), 0.08 ($z_{\text{reio}} = 9.367$)

Table 3.1: Free parameters in the analysis

where $\langle \cdot \rangle$ means the ensemble average, and $\langle \hat{C}_l \rangle = \langle C_l \rangle$. By substituting Eq. (3.1) into Eq. (3.2) and assuming the power spectra are parametrized by a set of parameters \vec{p} (in this study, $\vec{p} = (r, z_{\text{reio}})$), the cosmological information on these parameters is quantified by the Fisher matrix (Namikawa et al., 2010):

$$F_{ij} = \sum_{l=2}^{l_{\text{max}}} \frac{2l+1}{2} f_{\text{sky}} \text{Tr} \left(C_l^{-1}(\vec{p}) \frac{\partial C_l}{\partial p_i}(\vec{p}) C_l^{-1}(\vec{p}) \frac{\partial C_l}{\partial p_j}(\vec{p}) \right), \quad (3.3)$$

where the quantity C_l is the covariance matrix:

$$C_l = \begin{bmatrix} C_l^{BB} & C_l^{EB} \\ C_l^{EB} & C_l^{EE} \end{bmatrix}. \quad (3.4)$$

We assume the standard cosmology where $C_l^{EB} = 0$. In Eq. (3.3), we replace the derivatives of the C_l with a finite difference:

$$\frac{\partial C_l}{\partial p_i}(\vec{p}) \simeq \frac{C_l(p_i + \Delta p_i) - C_l(p_i - \Delta p_i)}{2\Delta p_i}. \quad (3.5)$$

3.2 Experimental model

We use the CLASS package (Blas et al., 2011) to simulate observation data \hat{C}_l in Eq. (3.1). We generate different kinds of simulated data by using various models. Here we call them fiducial models. To simulate observation data \hat{C}_l which can be used to study the uncertainty of tensor-to-scalar ratio (r) and reionization history (described by $x_e(z)$), we vary r and modify the shape of x_e . As for the theory model (C_l), we assume the shape of x_e as the tanh shape and vary r and z_{reio} to fit the fiducial model. Table 3.1 describes the parameters we used. An example of the tanh shape reionization history is shown as the blue line in Fig. 3.2. This section will list the noise for the LiteBIRD telescope and the fiducial models we used in this study. We will start from the exponential model, which is most similar to the tanh shape, and gradually make the shape of the reionization history more and more different from the tanh shape.

3.2.1 Noise

The noise angular power spectra is described as (Namikawa et al., 2010):

$$N_l \equiv \left(\frac{\sigma}{T_{\text{CMB}}} \frac{\pi}{10800} \right)^2 \exp \left[\frac{l(l+1)}{8 \ln 2} \left(\theta \frac{\pi}{10800} \right)^2 \right], \quad (3.6)$$

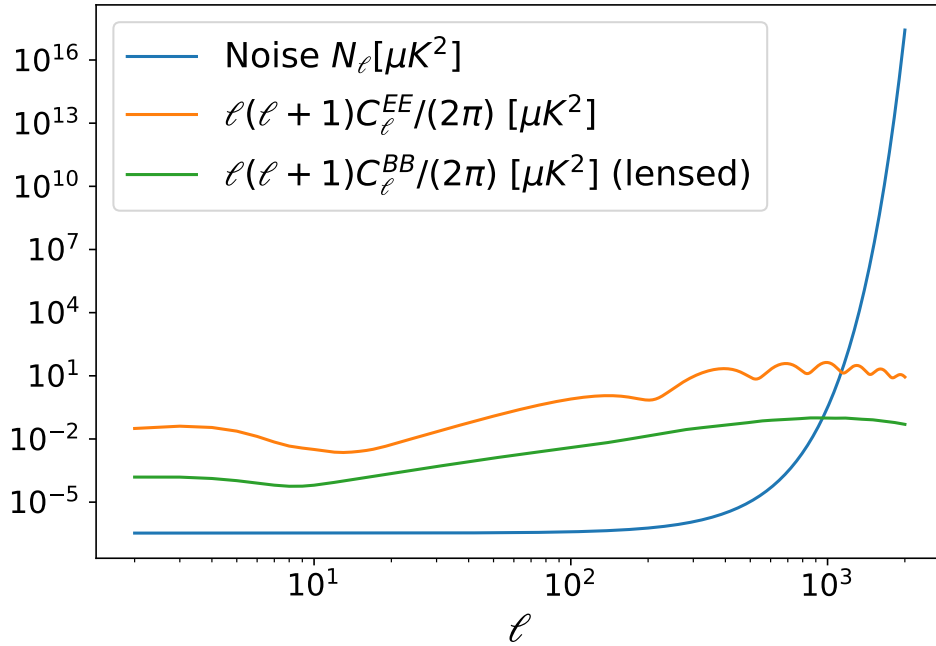


Figure 3.1: Noise power spectrum. We also plot the EE and BB power spectra here. The noise power spectrum increases quickly on a small scale and becomes much larger than the EE and BB power spectra.

where the quantity θ is the beam size in unit of arcmin, σ is the noise level in polarization map in unit of $\mu\text{K}\text{-arcmin}$, and $T_{\text{CMB}} = 2.725 \times 10^6 \mu\text{K}$ is the CMB black-body temperature. We assume a LiteBIRD-like experiment where $\theta = 30$ arcmin and $\sigma = 2\mu\text{K}\text{-arcmin}$. The noise power spectrum for $l \leq 2000$ is shown in Fig. 3.1. Due to the effect of the beam, noise increases rapidly at small scales.

3.3 Reionization model

3.3.1 Exponential model

First, we set the exponential model as the fiducial model from the CAMB package (Lewis et al., 2000), and it can be described as ²:

$$x_e(z) = \begin{cases} x_{e,\text{before}} & z > z_{\text{start}}, \\ f \exp\left(-\lambda \frac{(z - z_c)^{3/2}}{1 + \frac{\Delta z}{(z - z_c)^2}}\right) + x_{e,\text{before}} + x_{e,\text{He}} & z_c < z < z_{\text{start}}, \\ x_{e,\text{after}} + x_{e,\text{He}} & z < z_c, \end{cases} \quad (3.7)$$

²The definition can be found from the source code of the CAMB package: <https://github.com/cmbant/CAMB/blob/master/fortran/reionization.f90> (line 380-403)

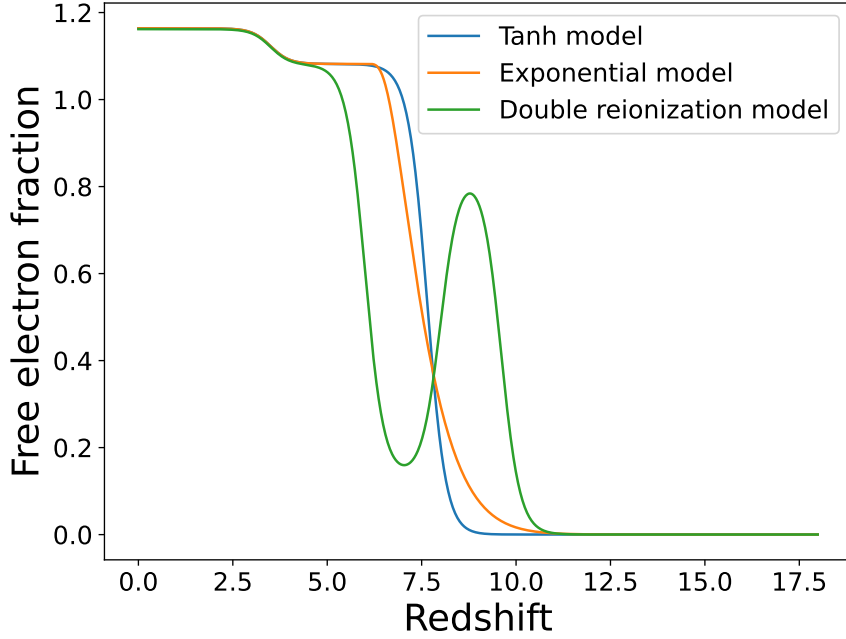


Figure 3.2: Free electron fraction (x_e) as the function of redshift (z), for the tanh model (blue line), exponential model (orange line), and double reionization model (green line). We set $z_{\text{reio}} = 7.6711$ for the tanh model and $z_{\text{reio}} = 7.29$ for the exponential model to keep the optical depth (τ) as 0.054 matching the result from the Planck collaboration. For the double reionization model, we set three points $(z, x_e) = \{(6, 1.08), (8, 0.13), (9.6, 0.845)\}$ to make $\tau = 0.054$.

where the z_c is the redshift that the reionization completed, we fix it as 6.1. The evolution rate in the exponential λ is:

$$\lambda = \frac{-\ln 0.5}{(z_{\text{reio}} - z_c)^{2/3}}. \quad (3.8)$$

f is:

$$f = x_{e,\text{after}} - x_{e,\text{before}}. \quad (3.9)$$

$x_{e,\text{He}}$ is:

$$x_{e,\text{He}} = \frac{1}{2} \left(1 + \tanh \left(\frac{z_{\text{He}} - z}{\Delta z_{\text{He}}} \right) \right) \times f_{\text{He}}. \quad (3.10)$$

In the CLASS package, f_{He} is defined as:

$$f_{\text{He}} = \frac{Y_{\text{He}}}{\frac{m_{\text{He}}}{m_{\text{H}}} \times (1 - Y_{\text{He}})}, \quad (3.11)$$

where Y_{He} is the Helium fraction, which is 0.25 according to the observation of primordial Helium abundance. Here, Δz and Δz_{He} are the widths of the Hydrogen and Helium reionization. z_{He} is similar to the z_{reio} in the Hydrogen reionization. We fix them here for simplicity.

In summary, the exponential model is described from Eq. (3.7) to Eq. (3.11). We only vary the z_{reio} among them to modify the shape of the exponential reionization history and fix cosmological parameters are Planck results and other free parameters as the default value in the

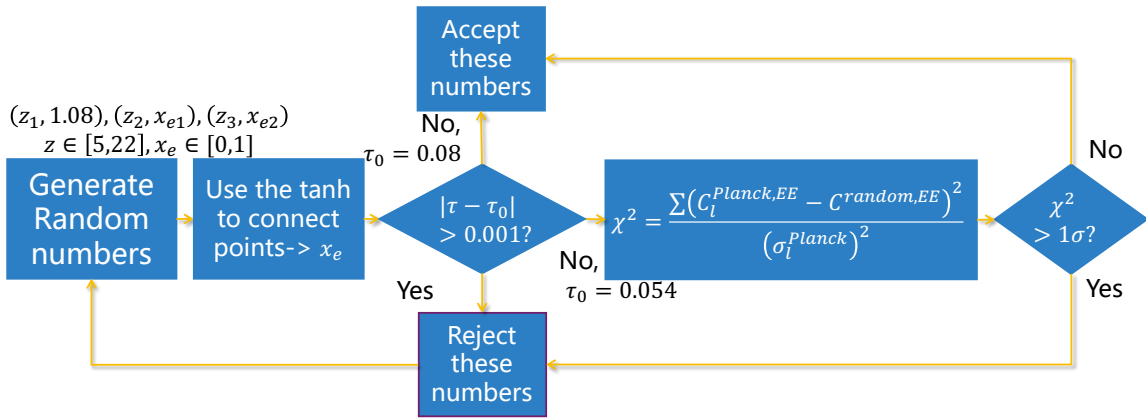


Figure 3.3: The process to generate random x_e model. We generate three random redshift points within $5 \sim 22$, among them z_1 is the end of the reionization and $x_e(z_1)$ is 1.08 which corresponds to the Helium reionization. We also generate two random numbers $x_e(z_2)$ and $x_e(z_3)$ within $0 \sim 1$. After that, we use the tanh function to connect them. We consider two cases: $\tau_0 = 0.054$ and $\tau_0 = 0.08$. To generate a reionization history with $\tau = 0.08$, we will accept these numbers if $|\tau - \tau_0| < 0.001$. For $\tau = 0.054$, we will also verify this model consistent with Planck's result (Tristram et al., 2024).

CLASS package. The orange line in Fig. 3.2 shows an example of exponential reionization.

3.3.2 Double reionization model

Another model we want to check is the double reionization model from Cen (2003). We set three points (z, x_e) and use the tanh function to connect them. The green line in Fig. 3.2 shows an example of double reionization.

3.3.3 Random x_e model

As shown in Fig. 3.3, to test whether the exotic reionization history will affect the constraints on r , we generate the parametrized reionization history as a function of z using random points. We generated 20 random x_e models for $\tau = 0.054$ and $\tau = 0.08$ respectively.

Chapter 4

Results

4.1 Fisher analysis results

For the fiducial exponential model, we estimate the uncertainties of the tensor-to-scalar ratio (r) and the redshift at the free electron fraction $x_e=0.5$, marked as z_{reio} . We consider the $\tau = 0.054$ ($z_{\text{reio}} = 7.249$) consistent with the Planck result, and higher τ set as 0.08 ($z_{\text{reio}} = 9.367$). Besides, we set r as 0.01 and 0.001. These parameters are summarized in Table 3.1. We use the full power spectra (here we set $l < 2002$), and we have σ_r and $\sigma_{z_{\text{reio}}}$ in Table 4.1 from the Fisher analysis. We find that σ_r increases as r or z_{reio} increases since the power spectra for higher r or higher z_{reio} are larger.

4.2 χ^2 results

In this section, we show the best fit and the uncertainties of the parameters by maximizing the likelihood $L(\tilde{C}_l|C_l)$, i.e. minimizing χ^2 in equation 3.1.

4.2.1 The exponential model

We set the exponential model described in Eq. (3.7) as our fiducial model. Its shape is shown as the orange line in Fig. 3.2. The fiducial values, the best-fit parameters, and their uncertainties are summarized in Table 4.2. The best-fit values are from the point (r, z_{reio}) with the maximum posterior value. We fit the marginalized 1D posterior with the Gaussian distribution to obtain the uncertainty σ . The posterior distribution for the baseline case with $r = 0.01$ and $\tau = 0.054$ is shown in Fig. 4.1. The posterior distributions for r and z_{reio} can be fitted well by Gaussian distribution. For comparison, we show the posterior distributions with $r = 0.001$ in Fig. 4.2 and $\tau = 0.08$ in Fig. 4.3. The case with $r = 0.001$ and z_{reio} is shown in Fig. A.1. We found that the uncertainties are closed with the uncertainties by the Fisher analysis in Table 4.1. In addition, the bias to r is very small. Only when $r = 0.001$ and $\tau = 0.08$, the bias to r will be around $0.25\sigma_r$. In other cases, the bias to r is less than $0.1\sigma_r$. The bias to r when $r = 0.01$ is smaller than $r = 0.001$, and when $\tau = 0.054$ is smaller than $\tau = 0.08$. Besides, the shape of

		σ_r		σ_{reio}	
		7.25	9.37	7.25	9.37
r	z_{reio}				
	0.01	3.41×10^{-4}	3.37×10^{-4}	3.49×10^{-2}	2.95×10^{-2}
0.001		1.83×10^{-4}	1.61×10^{-4}	3.50×10^{-2}	2.95×10^{-2}

Table 4.1: The prediction of the 1σ uncertainties on r and z_{reio} from the Fisher matrix using the full power spectra.

τ	r	Best-fit r	Best-fit z_{reio}	σ_r	$\sigma_{z_{\text{reio}}}$
0.054	0.01	1.00×10^{-2}	7.64	4.18×10^{-4}	4.88×10^{-2}
0.054	0.001	0.991×10^{-3}	7.64	2.22×10^{-4}	4.88×10^{-2}
0.080	0.01	0.997×10^{-2}	10.1	4.14×10^{-4}	4.35×10^{-2}
0.080	0.001	0.952×10^{-3}	10.1	1.93×10^{-4}	4.35×10^{-2}

Table 4.2: Summary of the best-fit parameters and uncertainties for the exponential model.

τ	r	Best-fit r	Best-fit z_{reio}	σ_r	σ_{reio}
0.054	0.01	0.998×10^{-2}	7.64	4.19×10^{-4}	4.88×10^{-2}
0.054	0.001	0.952×10^{-3}	7.64	2.23×10^{-4}	4.88×10^{-2}
0.080	0.01	1.00×10^{-2}	10.1	4.15×10^{-4}	4.34×10^{-2}
0.080	0.001	0.942×10^{-3}	10.1	1.94×10^{-4}	4.34×10^{-2}

Table 4.3: Same as Table 4.2 but for the double reionization model.

τ	r	Best-fit r	Best-fit z_{reio}	σ_r	σ_{reio}
0.080	0.001	0.778×10^{-3}	10.1	1.93×10^{-4}	4.31×10^{-2}

Table 4.4: Same as Table 4.2 but for the random x_e model which introduces a non-negligible bias.

the posterior distribution of r for $r = 0.001$ is different from the Gaussian distribution shown in Fig. 4.2.

We also compare the shape of x_e and power spectra with the fiducial and best-fit models. x_e is shown in Fig. 4.4, and power spectra are shown in Fig. 4.5 and Fig. 4.6 (for the $\tau = 0.08$ and $r = 0.001$ case, their power spectra are shown in Fig. A.2). Given the same τ , the x_e and EE power spectra shapes in the best-fit models remain almost the same across different r values. From Fig. 4.4, in the exponential model, the reionization process occurs earlier and is relatively smoother. When $\tau = 0.054$, there is a slight difference between the exponential model and the tanh model; however, at $\tau = 0.08$, the distinction between the two models becomes apparent. As a result, the difference in EE and BB power spectra is smaller when $\tau = 0.054$ than when $\tau = 0.08$. As for BB power spectra, since the lensing effect dominates on the small scale, the reionization bump is small when $r = 0.001$, making it harder to distinguish two models in the lowest lines in Fig. 4.5 and 4.6.

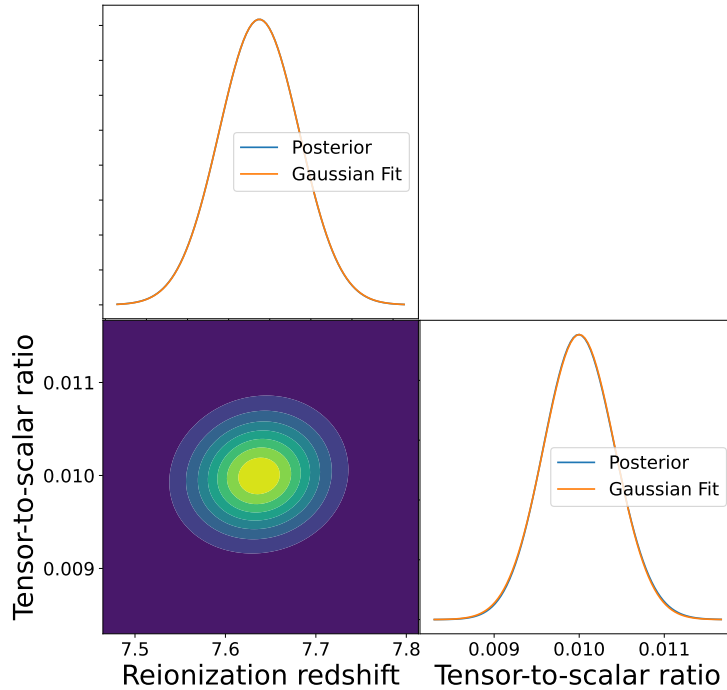


Figure 4.1: The posterior distribution of r and z_{reio} for the exponential model with $r = 0.01$ and $\tau = 0.054$. The blue lines represent the posterior distribution, while the orange lines represent the Gaussian fit. In the contour plot, yellow indicates high probability and blue indicates low probability.

4.2.2 The double reionization model

We use the double reionization model described in the previous chapter. We fix three points $(z, x_e) = \{(6, 1.08), (8, 0.13), (9.6, 0.845)\}$ to set $\tau = 0.054$ and $(z, x_e) = \{(6.8, 1.08), (9.5, 0.31), (12.2, 0.92)\}$ to set $\tau = 0.08$. The fiducial values, their best-fit parameters, and uncertainties are summarized in Table 4.3. To compare with the baseline case, we show the posterior distribution with $r = 0.01$ and $\tau = 0.054$ for the double reionization model in Fig. 4.7, and other cases are shown in the Fig. A.3, Fig. A.4 and Fig. A.5. We can find that the biases to r are still small, which are $O(0.01) \times \sigma_r$ for $r = 0.01$ and $O(0.1) \times \sigma_r$ for $r = 0.001$. Interestingly, compared to the results for the exponential model shown in table 4.2, the values of σ_r are smaller, while the values of $\sigma_{z_{\text{reio}}}$ are larger in every case. The posterior distributions are similar to that for the exponential models, where the posterior distribution of r is different from the Gaussian distribution when $r = 0.001$.

x_e for the double reionization model is shown in Fig. 4.8 and power spectra are shown in Fig. 4.9. Power spectra with $r = 0.001$ and $\tau = 0.08$ are shown in Fig. A.6 and Fig. A.7, respectively. We find that as previously noted, for the same τ , the shapes of the x_e and EE power spectra in the best-fit models show little variation across different r values. By comparing Fig. 4.5 and Fig. 4.9, we find that the best-fit power spectra for the double reionization model deviate more from the fiducial model compared to the exponential model. This deviation is particularly pronounced in the reionization bump of the EE and BB power spectra, as well as in the trough of the EE

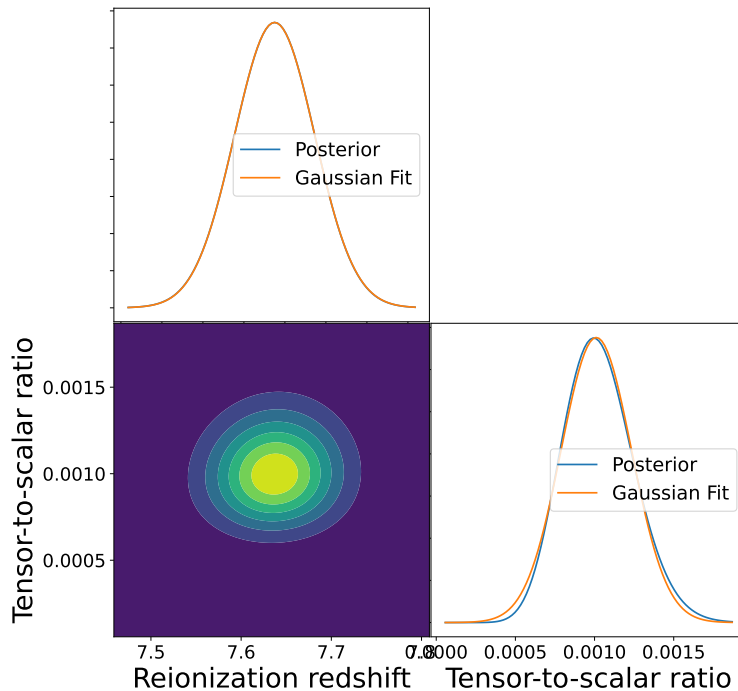


Figure 4.2: Same as Fig. 4.1 but with $r = 0.001$.

power spectra, especially when $\tau = 0.08$ in Fig. A.7. However, these deviations are all within the error bars. For the reionization bump, the scale corresponding to the peak is slightly larger in the tanh and exponential models compared to the double reionization model. This difference might be attributed to the earlier occurrence of reionization in the double reionization model, related to the distance between CMB photons and the electrons ionized during the reionization epoch shown in Eq. (2.167).

4.2.3 Random x_e model

The random x_e models that we generated are shown in Fig. C.1, and power spectra are shown in Fig. C.2. We show the distribution of the Euclidean distance in Fig. 4.10, defined as:

$$d = \sqrt{\sum_{i=1}^{1500} (x_{e,\text{model}}(z_i) - x_{e,\text{tanh}}(z_i))^2}, \quad (4.1)$$

where z is from 0 to 22.3, divided into 1500 redshift bins. The Euclidean distance serves as a quantitative measure of the similarity between the random models and the tanh model, allowing us to evaluate how closely the random models approximate the behavior of the tanh function. Fig. 4.10 provides a view of how the Euclidean distances between random models and the tanh model vary under two different parameter settings of τ . It shows that the distances tend to be higher and more variable when $\tau = 0.08$ compared to $\tau = 0.054$. Fig. 4.11 shows the distribution of biases introduced by fitting with the wrong theory model. For both $\tau = 0.054$ and $\tau = 0.08$,

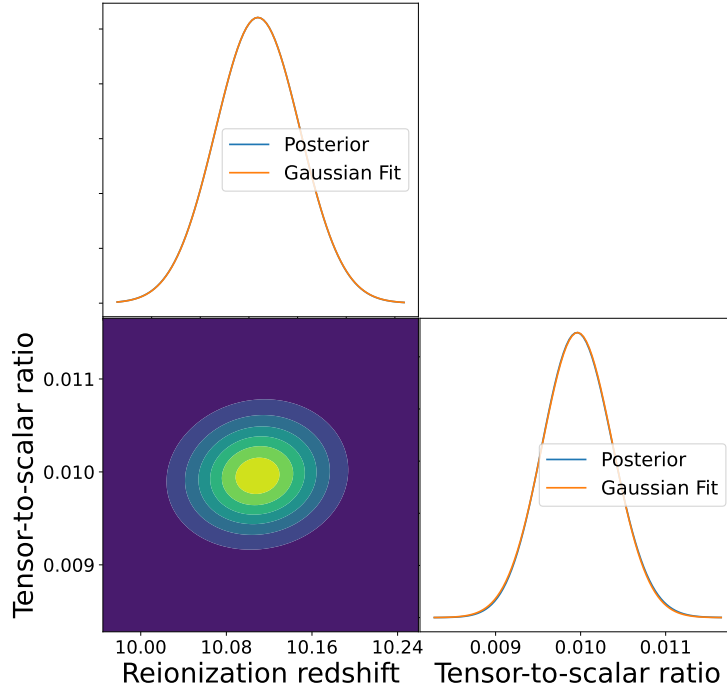


Figure 4.3: Same as Fig. 4.1 but with $\tau = 0.08$.

when $r = 0.01$, the distribution is tightly clustered with a low median and interquartile range. However, when $r = 0.001$, the distribution broadens with a higher median compared to $r = 0.01$. Notably, for $\tau = 0.08$ and $r = 0.001$, the distribution becomes significantly broader, exhibiting a higher median and greater variability, with a prominent outlier. The most striking finding is that the largest bias Δr can exceed $1\sigma_r$, a deviation that is far from negligible and demands serious attention. Its shape is shown in Fig. 4.12, and the posterior distribution and power spectra for this case are shown in Fig. 4.13 and Fig. 4.14. The best-fit values and uncertainties are summarized in Table 4.4. From Fig. 4.12, we see that the random x_e model started the reionization epoch much earlier than the best-fit tanh model, and we can also see the smaller-scale reionization peak in Fig. 4.14. Fortunately, despite introducing a non-negligible bias to r , the EE power spectrum, especially the trough in it, provides a clear distinction between the models. The best-fit EE power spectrum significantly deviates from the fiducial EE power spectrum, allowing for effective differentiation.

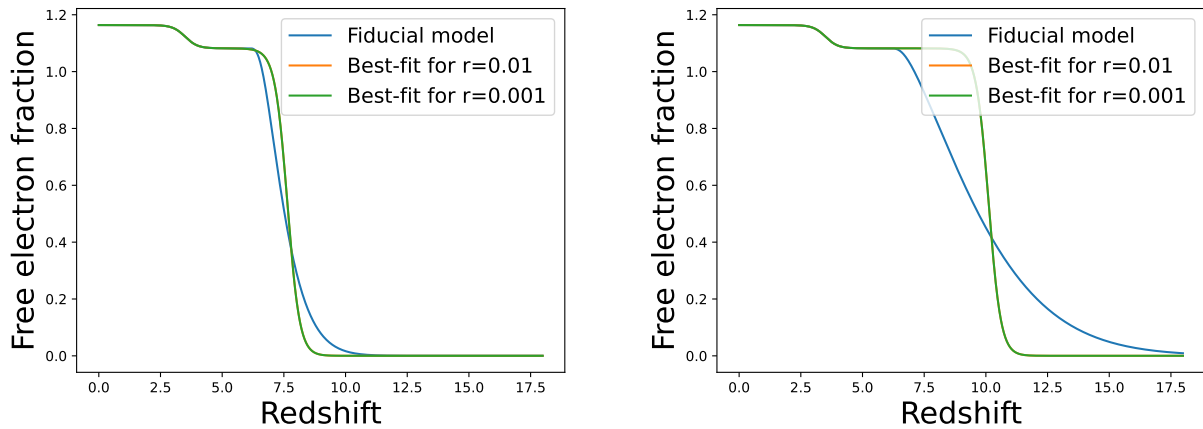


Figure 4.4: The free electron fraction x_e for the exponential model with $\tau = 0.054$ (left) and $\tau = 0.08$ (right). The blue lines represent x_e for the fiducial models, the orange lines represent x_e for the best-fit model with $r = 0.01$, and the green lines represent x_e with $r = 0.001$. The orange lines and green lines are almost overlapping.

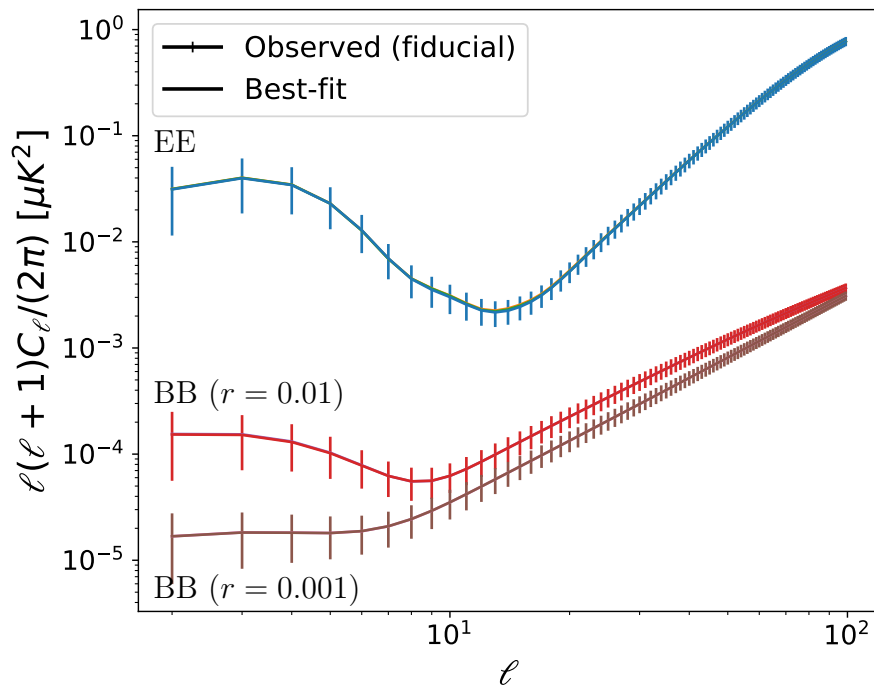


Figure 4.5: EE and BB power spectra with $\tau = 0.054$ for the exponential model. The blue line is the fiducial EE power spectrum, the red line is the fiducial BB power spectrum with $r = 0.01$ and the brown line is the fiducial BB power spectrum with $r = 0.001$. The orange line and the green line are the best-fit EE power spectra, and they are almost overlapping. The purple and pink lines are the best-fit BB power spectra with $r = 0.01$ and $r = 0.001$, respectively.

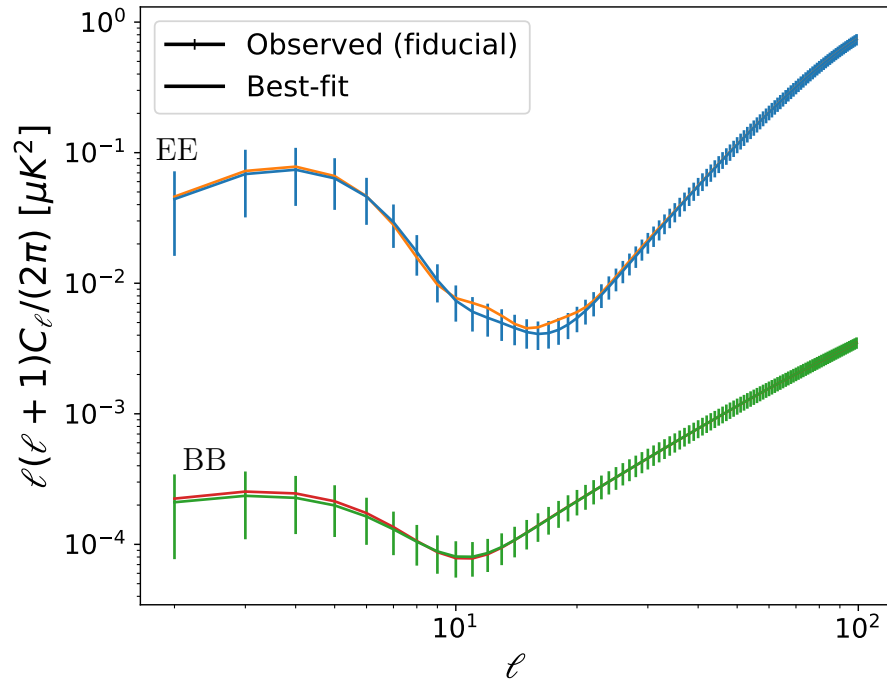


Figure 4.6: EE and BB power spectra with $\tau = 0.08$ and $r = 0.01$ for the exponential model. Blue and green lines are the fiducial EE and BB power spectra, while orange and red lines are the best-fit power spectra.

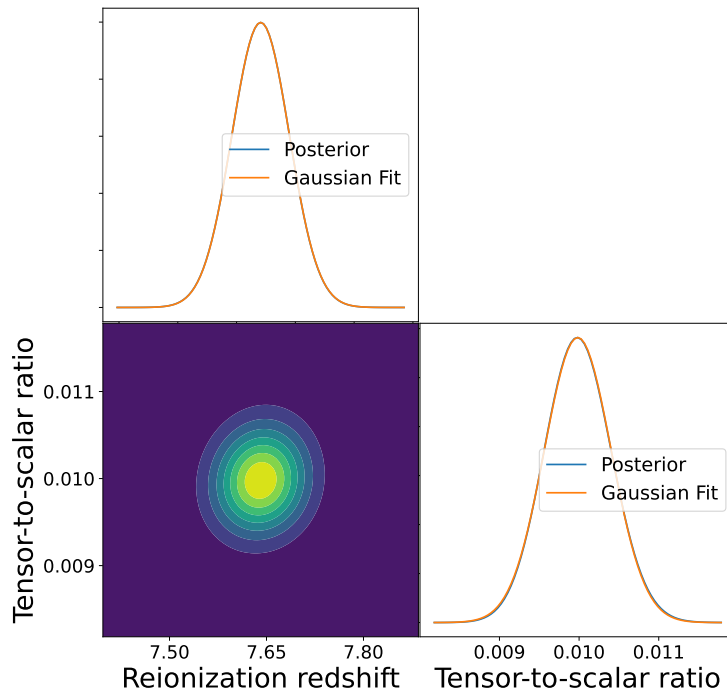


Figure 4.7: Same as Fig. 4.1 but for the double reionization model.

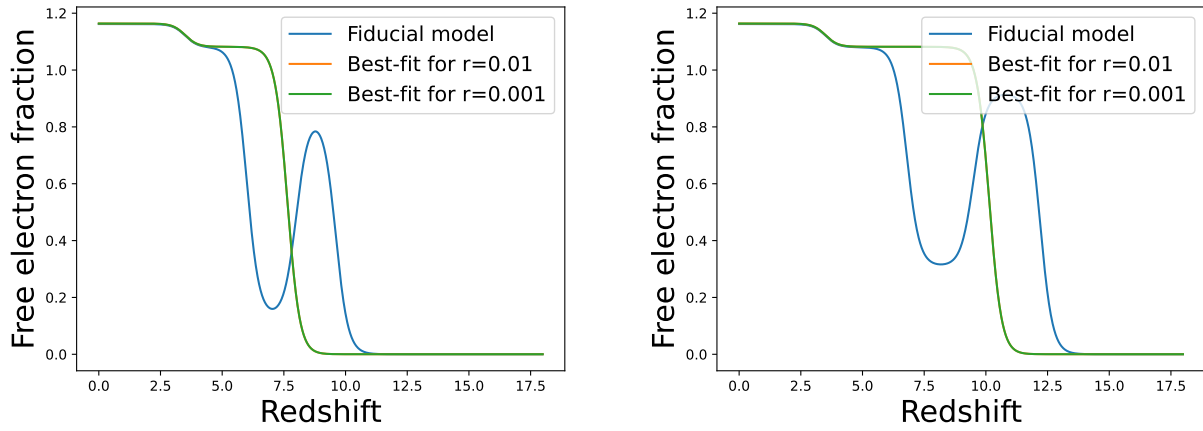


Figure 4.8: Same as Fig. 4.1 but for the double reionization model.

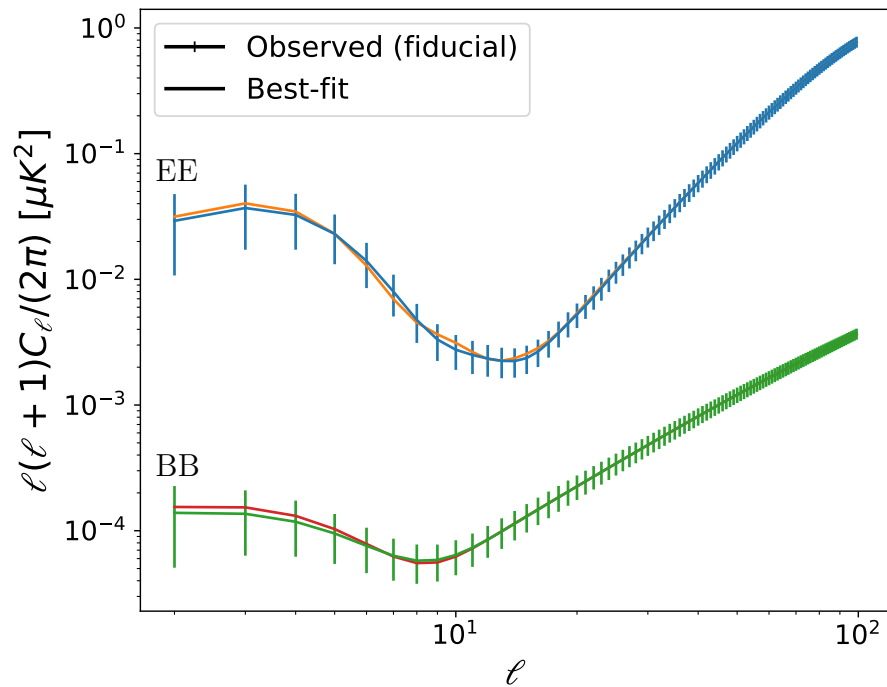


Figure 4.9: Same as Fig. 4.6 but for the double reionization model and $\tau = 0.054$.

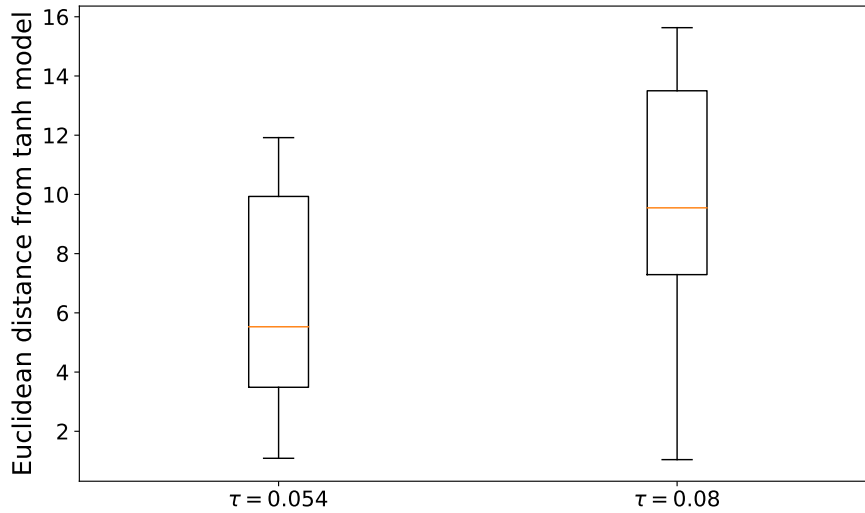


Figure 4.10: This box plot illustrates the distribution of Euclidean distance between random x_e models and the tanh model with $\tau = 0.054$ (left) and $\tau = 0.08$ (right). The orange line within each box represents the median Euclidean distance. The boxes represent the interquartile range (IQR), which contains the middle 50% of the data. The whiskers extend to the minimum and maximum values within 1.5 times the IQR from the first and third quartiles, respectively.

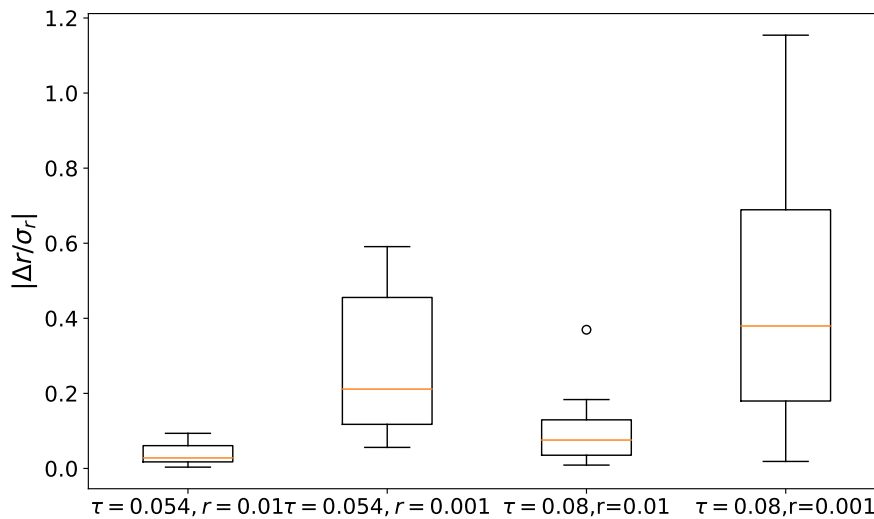


Figure 4.11: This box plot illustrates the distribution of the normalized absolute biases $|\Delta r/\sigma_r|$ for different combinations of the parameters τ and r . The four groups on the x-axis represent the parameter settings: $\tau = 0.054, r = 0.01$, $\tau = 0.054, r = 0.001$, $\tau = 0.08, r = 0.01$, and $\tau = 0.08, r = 0.001$.

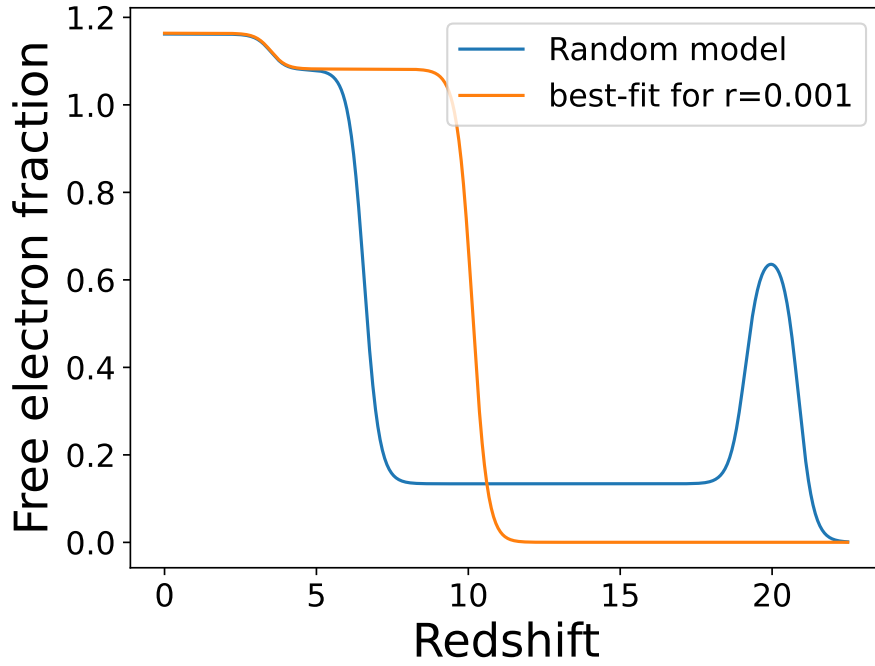


Figure 4.12: The free electron fraction x_e for the random x_e model which introduces a non-negligible bias with $r = 0.001$ and $\tau = 0.08$. The blue lines represent x_e for the fiducial models, the orange lines represent x_e for the best-fit model.

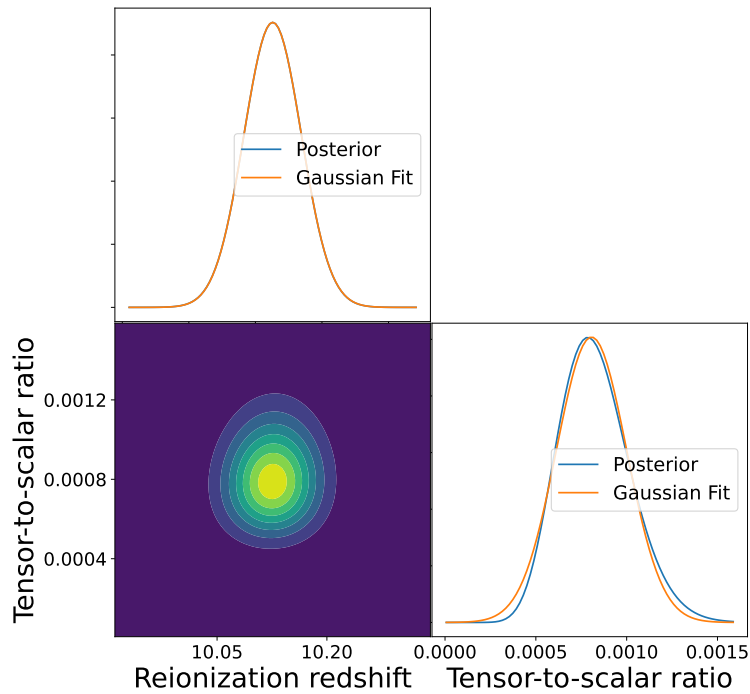


Figure 4.13: Same as Fig. 4.4 but for the random x_e model which introduces a non-negligible bias with $r = 0.001$ and $\tau = 0.08$.

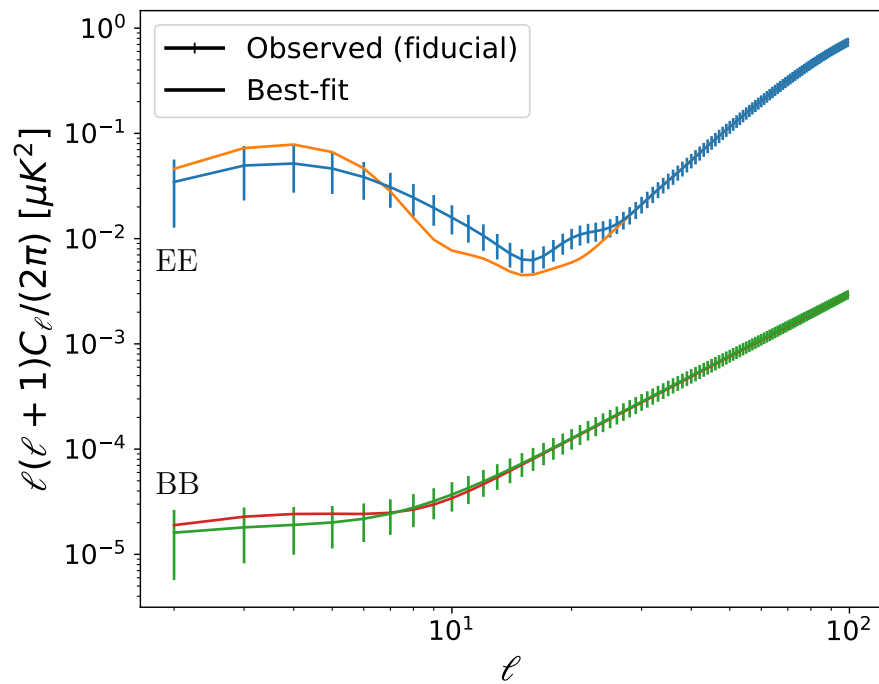


Figure 4.14: EE and BB power spectra with $\tau = 0.08$ and $r = 0.001$ for the random x_e model which introduces a non-negligible bias. Blue and green lines are the fiducial EE and BB power spectra, while orange and red lines are the best-fit power spectra.

Chapter 5

Discussion

5.1 Compare the role of different angular scales in constraining the tensor-to-scalar ratio

5.1.1 Exponential model

To discuss the role of the large-scale power spectra, we consider only using the large scale of the power spectra ($\ell < 10$). First, we calculate the uncertainties by only the Fisher analysis. The values of σ_r are given in Table 5.1, and $\sigma_{z_{\text{reio}}}$ in Table 5.2. Then, we also use the maximum likelihood estimate to get the best-fit parameters and their uncertainties. They are summarized in Table 5.3. To compare with the baseline case, we show the posterior distribution with $r = 0.01$ and $\tau = 0.054$ in Fig. 5.1, and other cases are shown in Fig. B.2, Fig. B.1, and Fig. B.3, respectively. We find that the uncertainties are consistent with the Fisher analysis. Without the small scales, the uncertainties in z_{reio} increase by an order of magnitude in every case. Additionally, the uncertainties in r increase by an order of magnitude when $r = 0.01$. Furthermore, the shapes of the 1D posterior distribution for all parameters are non-Gaussian, and all have a long tail toward large values of r or z_{reio} . Furthermore, the shapes of the 1D posterior distributions for all parameters are non-Gaussian, exhibiting long tails toward larger values of r or z_{reio} . When using only very large scales ($\ell < 10$), the parameters exhibit significant degeneracy. This is evident from the elongated shape of the contour in the joint posterior plot, indicating a strong correlation between z_{reio} and r . Interestingly, although the uncertainties increase by an order of magnitude, the biases change only slightly. In addition, the best-fit value of r is smaller than when using the full power spectra.

EE and BB power spectra are almost the same as the results when using full power spectra.

$r \backslash z_{\text{reio}}$	7.249	9.367
0.01	1.5113×10^{-3}	1.3366×10^{-3}
0.001	2.7342×10^{-4}	2.1365×10^{-4}

Table 5.1: The prediction of σ_r from the Fisher matrix using only the large-scale power spectra.

$r \backslash z_{\text{reio}}$	7.249	9.367
0.01	1.8764×10^{-1}	2.0105×10^{-1}
0.001	2.0551×10^{-1}	2.2101×10^{-1}

Table 5.2: The prediction of $\sigma_{z_{\text{reio}}}$ from the Fisher matrix using only the large-scale power spectra.

τ	r	Best-fit r	Best-fit z_{reio}	σ_r	σ_{reio}
0.054	0.01	1.00×10^{-2}	7.63	2.10×10^{-3}	2.86×10^{-1}
0.054	0.001	0.986×10^{-3}	7.63	3.45×10^{-4}	2.87×10^{-1}
0.080	0.01	0.920×10^{-2}	10.2	1.78×10^{-3}	3.48×10^{-1}
0.080	0.001	0.904×10^{-3}	10.2	2.53×10^{-4}	3.50×10^{-1}

Table 5.3: Summary of best-fit parameters and uncertainties ($\ell < 10$) for the exponential model.

τ	r	Best-fit r	Best-fit z_{reio}	σ_r	σ_{reio}
0.054	0.01	0.966×10^{-2}	7.64	1.84×10^{-3}	6.22×10^{-2}
0.054	0.001	0.894×10^{-3}	7.64	3.24×10^{-4}	6.22×10^{-2}
0.080	0.01	0.959×10^{-2}	10.14	1.61×10^{-3}	5.55×10^{-2}
0.080	0.001	0.904×10^{-3}	10.14	2.46×10^{-4}	5.55×10^{-2}

Table 5.4: Summary of best-fit parameters and uncertainties when cutting only BB power spectrum for the double reionization model.

τ	r	Best-fit r	Best-fit z_{reio}	σ_r	σ_{reio}
0.054	0.01	0.945×10^{-2}	7.70	2.02×10^{-3}	2.90×10^{-1}
0.054	0.001	0.907×10^{-3}	7.70	3.24×10^{-4}	2.90×10^{-1}
0.080	0.01	0.875×10^{-2}	10.4	1.69×10^{-3}	3.56×10^{-1}
0.080	0.001	0.843×10^{-3}	10.4	2.35×10^{-4}	3.56×10^{-1}

Table 5.5: Summary of best-fit parameters and uncertainties ($\ell < 10$) for the double reionization model.

For $\tau = 0.054$ and $r = 0.01$, they are shown in Fig. 5.2, while other cases are shown in Fig. B.4 and Fig. B.5, respectively.

Double reionization model

For the double reionization model, we consider two scenarios for comparison: cutting only the BB power spectra (keeping $\ell < 10$ for BB power spectra) and cutting both the EE and BB power spectra (keeping $\ell < 10$ for both EE and BB power spectra). The results of the former are presented in Table 5.4, and the latter are presented in Table 5.5. To compare with the baseline, we show the posterior distribution with $\tau = 0.054$ and $r = 0.01$ for the former in Fig. 5.3, and the latter in Fig. 5.4. We observe that the uncertainties in z_{reio} increase only slightly when we cut the BB power spectra, but increase significantly when we cut both BB and EE power spectra. Besides, the 1D posterior distribution of z_{reio} becomes non-Gaussian after cutting both

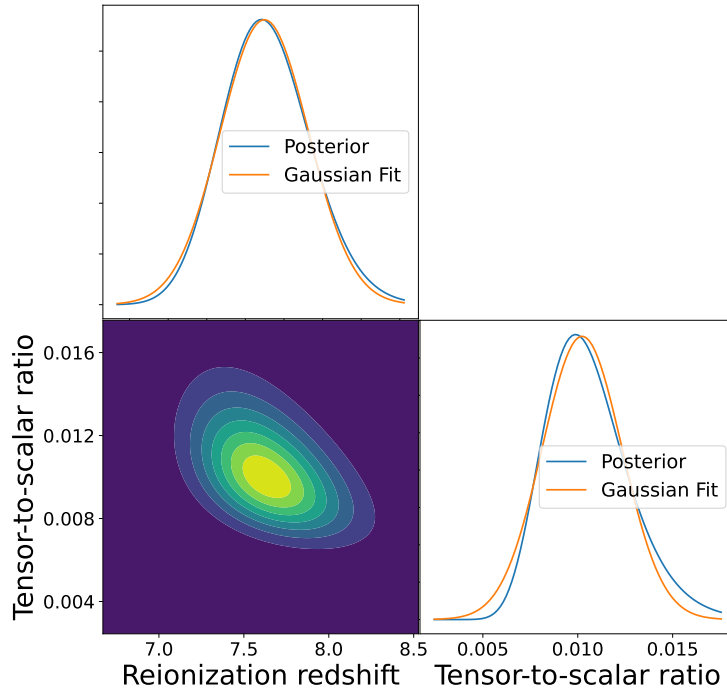


Figure 5.1: Same as Fig. 4.1 but only using very large scales ($\ell < 10$).

BB and EE power spectra. This indicates that z_{reio} is primarily constrained by the EE power spectra. Conversely, when only the BB power spectra are cut, σ_r increases substantially for $r = 0.01$, and the bias in r increases significantly for $r = 0.001$. This suggests that the BB power spectra play a crucial role in constraining r . The best-fit value of r generally decreases as fewer power spectra are used to constrain it. Similar to when we use the full power spectra, using only the large scale power spectra results in a larger σ_r compared to the exponential case, while $\sigma_{z_{\text{reio}}}$ is smaller.

EE power spectra and BB power spectra for $\tau = 0.054$ and $r = 0.01$ are shown in Fig. 5.5 (cutting only BB power spectrum) and Fig. 5.6 (cutting both EE and BB power spectra). Other cases are shown in Fig. B.9, Fig. B.10, Fig. B.14, and Fig. B.15. Compared to using the full power spectra, constraining r and z_{reio} with only large-scale BB power spectra (keeping $\ell < 10$ for BB power spectra) results in a smaller best-fit r . After also cutting the small-scale EE power spectra, the best-fit r decreases further, while the best-fit z_{reio} increases. Similar to using the full power spectra, when using only large-scale power spectra, the best-fit r is smaller for the double reionization model than for the exponential model. Figures 5.7, 5.8, and 5.9 illustrate this. In each figure, the τ values for the three models are the same. For all of them, the tanh model shows the largest bump size, whereas the double reionization model shows the smallest bump size. Consequently, using the tanh model to fit these data typically results in a smaller r to match the lower bump of the tanh model. Moreover, the double reionization model has a lower peak. When fitting with the tanh model, r needs to be decreased more significantly than with the exponential model. Thus, both with the full power spectra and the large-scale power spectra, the best-fit r for the double reionization model is smaller than that for the exponential model. The large-scale BB power spectra are dominated by the reionization bump,

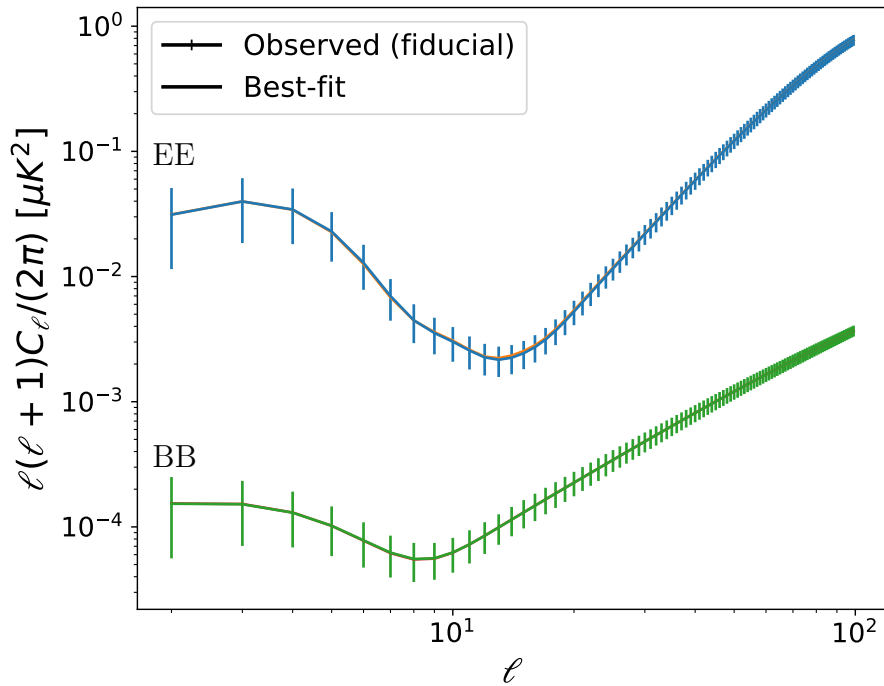


Figure 5.2: Same as Fig. 4.6 but only using very large scales ($\ell < 10$) and $\tau = 0.054$.

so after cutting the BB power spectra, the best-fit r decreases to align with the lower bump by the tanh model. Furthermore, the reionization time for the tanh model is the latest, while for the double reionization model, it is the earliest, corresponding to the peak positions shown in Fig. 5.7. To fit an earlier reionization, the best-fit z_{reio} increases. Therefore, the best-fit z_{reio} for the double reionization model is larger than that for the exponential model, both when using the full power spectra and the large-scale power spectra. Comparing Table 5.4 and Table 5.5, after cutting the EE power spectra, the best-fit r decreases further. This is because, to fit the earlier reionization, z_{reio} increases, causing τ for the tanh function to increase and produce a larger reionization bump. Consequently, to fit the large-scale BB power spectra, the best-fit r decreases again.

5.2 Summary

In this study, we examined how the reionization history influences constraints on the tensor-to-scalar ratio (r), a parameter related to the energy scale of cosmic inflation. Reionization introduces a bump in the large-scale B-mode and E-mode CMB polarization spectra, affecting power spectra shapes. The reionization history can affect the shape of power spectra, but it is poorly constrained. Therefore, We generated mock data using various reionization histories and fitted them with a tanh-shaped reionization model. The posterior distributions were calculated to assess uncertainties and biases, and the contributions of different multipoles to the constraints were analyzed.

Our results indicate that for exponential and double reionization models, the bias is minimal. Even when using only large-scale power spectra, the bias remains low, though the best-fit r tends to be smaller than the fiducial value due to the higher bump in the tanh model. Additionally,

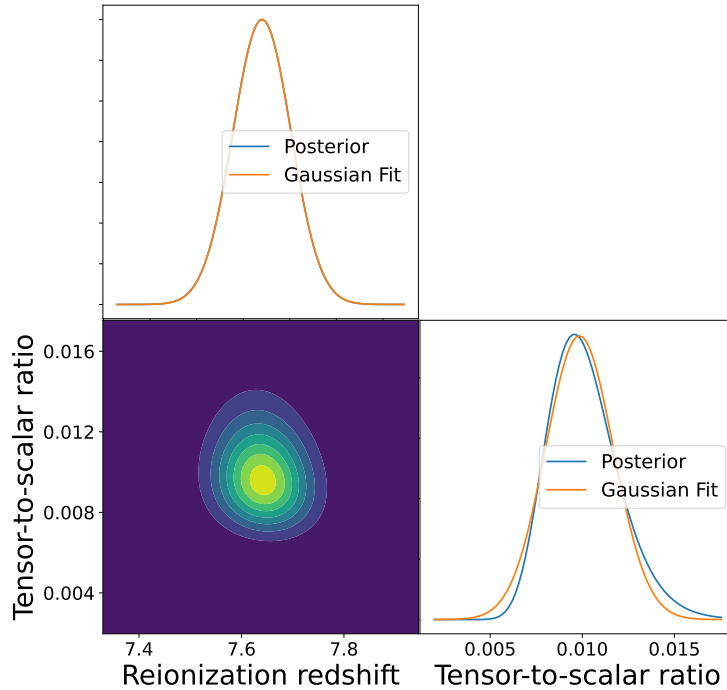


Figure 5.3: Same as Fig. 4.1 but for the double reionization model and cutting only BB power spectrum.

random x_e models showed that an incorrect reionization history could lead to significant bias in r , particularly when r is small and τ is large. However, large-scale EE power spectra can help exclude incorrect models. These findings underscore the importance of accurately modeling reionization history to avoid biases in r estimation. Future research should focus on refining reionization models and exploring their impacts on cosmological parameters further.

5.3 Future Work

While our study has provided significant insights into how reionization history affects constraints on the tensor-to-scalar ratio (r), several areas remain underexplored. Addressing these gaps could significantly advance our understanding of the early universe.

Firstly, although we find that the bias in r can exceed $1\sigma_r$, it remains unclear what specific features in the reionization history contribute to this large bias. To investigate this, we can generate more reionization histories parameterized by additional random points and establish statistical parameters to identify the relationship between these parameters and bias in r . Additionally, dividing x_e into several redshift bins will allow us to study the contributions of x_e at different redshifts to the power spectra more precisely.

Secondly, we find that the large-scale EE power spectra are effective in excluding exotic reionization models. Therefore, the contribution of large-scale EE power spectra warrants further investigation. In this study, we only discussed the role of very large-scale EE power spectra

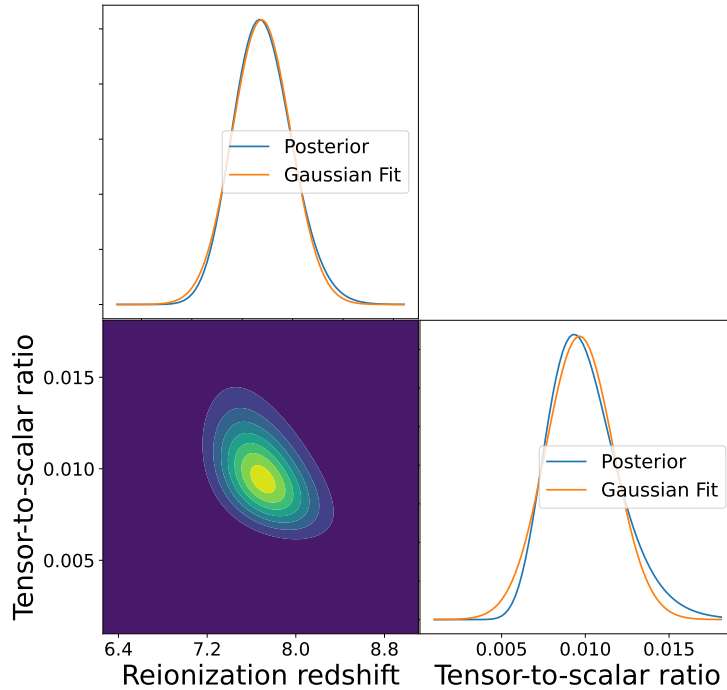


Figure 5.4: Same as Fig. 5.1 but for the double reionization model.

(the reionization bump), but it is also necessary to examine the contribution from the trough at $l \sim 10 - 30$. In our analysis, we fixed cosmological parameters, including the scalar amplitude, A_s . By using the temperature power spectrum, we can tightly constrain a combination of cosmological parameters, such as $A_s e^{-2\tau}$. In future work, we should fix the small-scale power spectrum amplitude, $A_s e^{-2\tau}$.

Thirdly, as mentioned in the introduction, matter-sourced inflation models can also amplify the reionization bump. This amplification increases the uncertainty caused by the reionization history. Therefore, further study of these scenarios is essential.

Lastly, this work did not account for foreground contamination. In practice, results will be influenced by residuals left after foreground cleaning and delensing. The impact of these residuals introduces additional uncertainties that must be studied further. It is essential to assess the magnitude of these effects to ensure that the derived constraints on r remain robust. Future work should include detailed modeling of foreground contamination and its mitigation to refine the accuracy of cosmological parameter estimates.

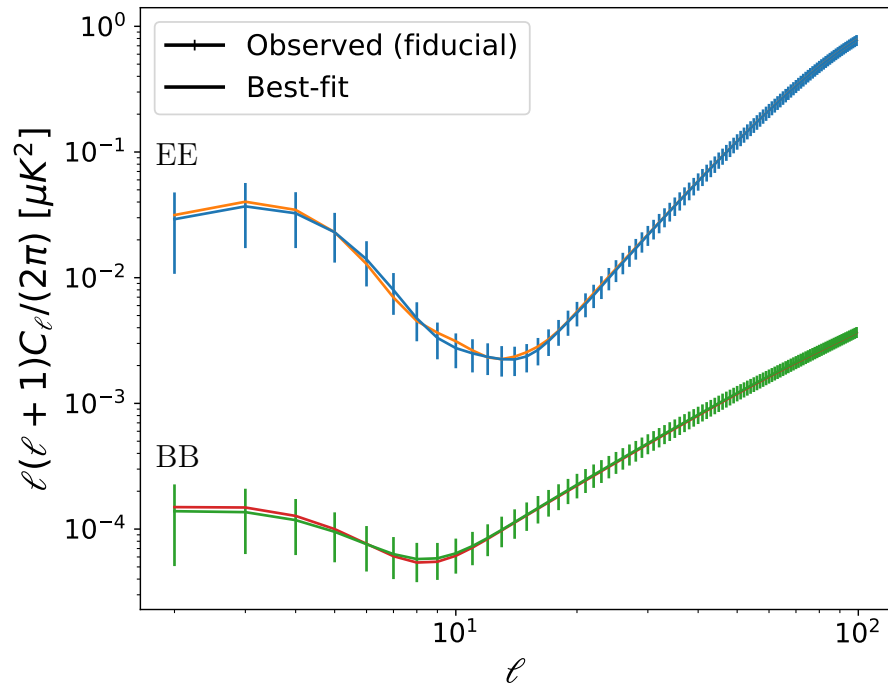


Figure 5.5: Same as Fig. 5.2 but for the double reionization model and cutting only BB power spectrum.

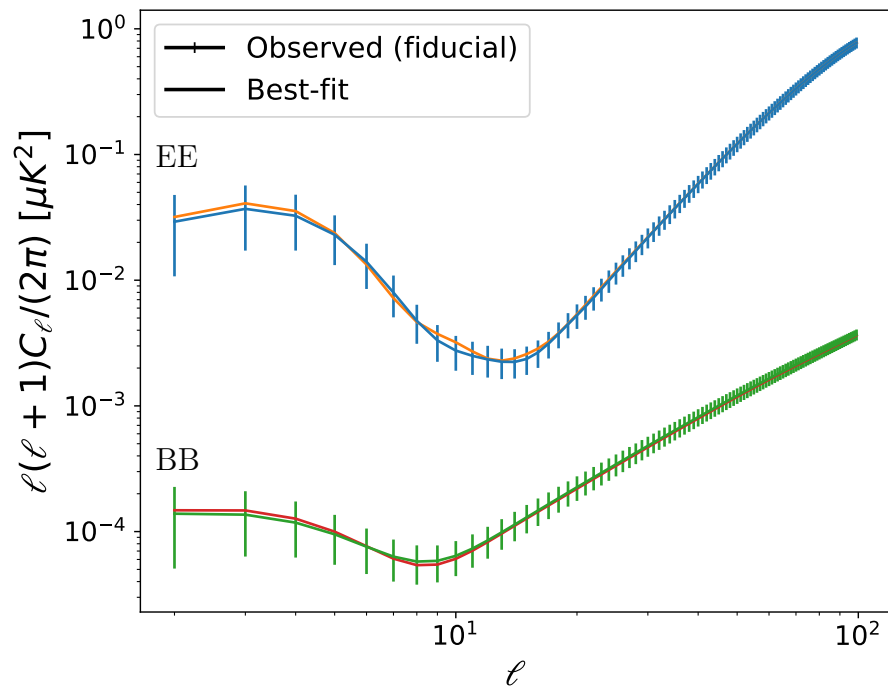


Figure 5.6: Same as Fig. 5.2 but for the double reionization model.

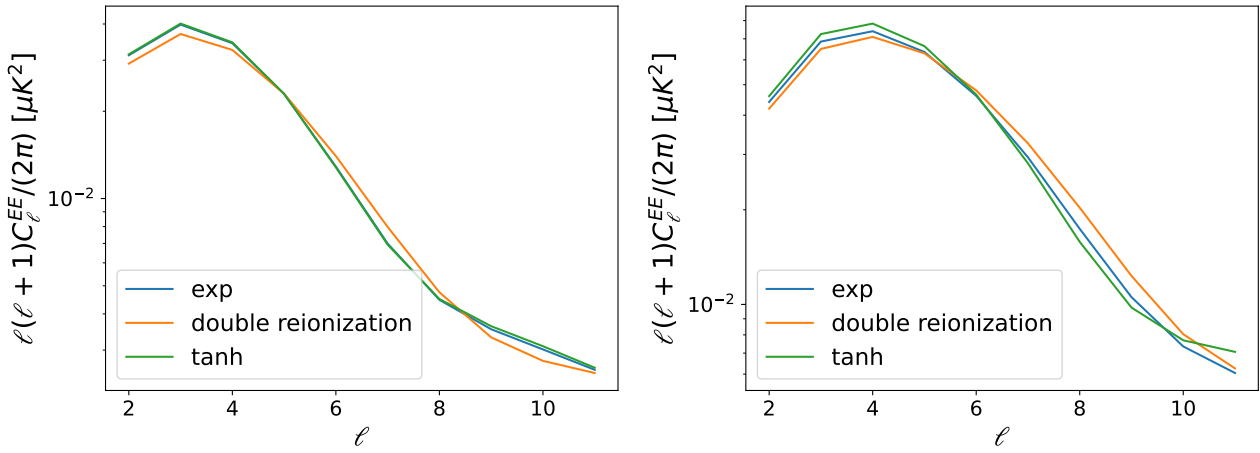


Figure 5.7: The very large-scale EE power spectra for $\tau = 0.054$ (left) and $\tau = 0.08$ (right).

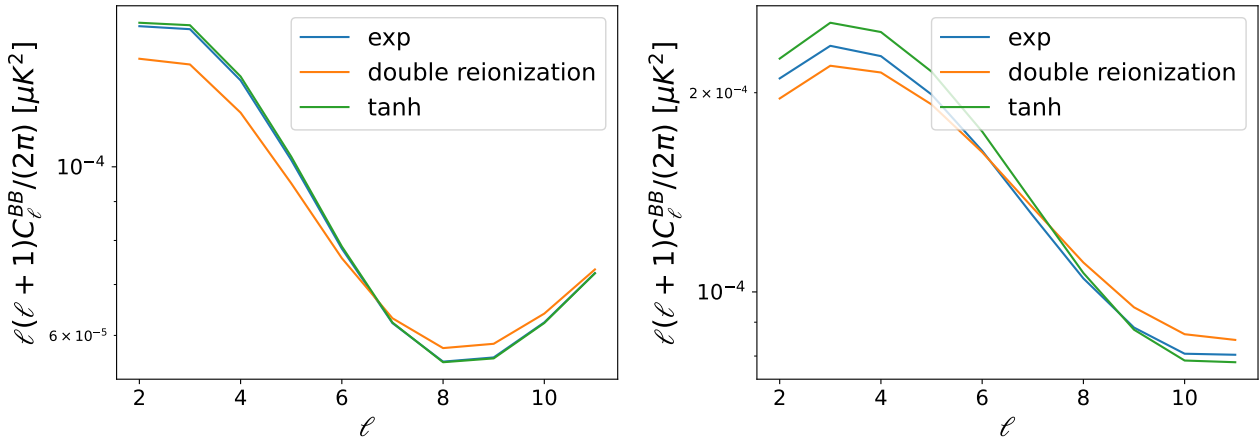


Figure 5.8: The very large-scale power spectra for $\tau = 0.054$ (left) and $\tau = 0.08$ (right) for $r = 0.01$.

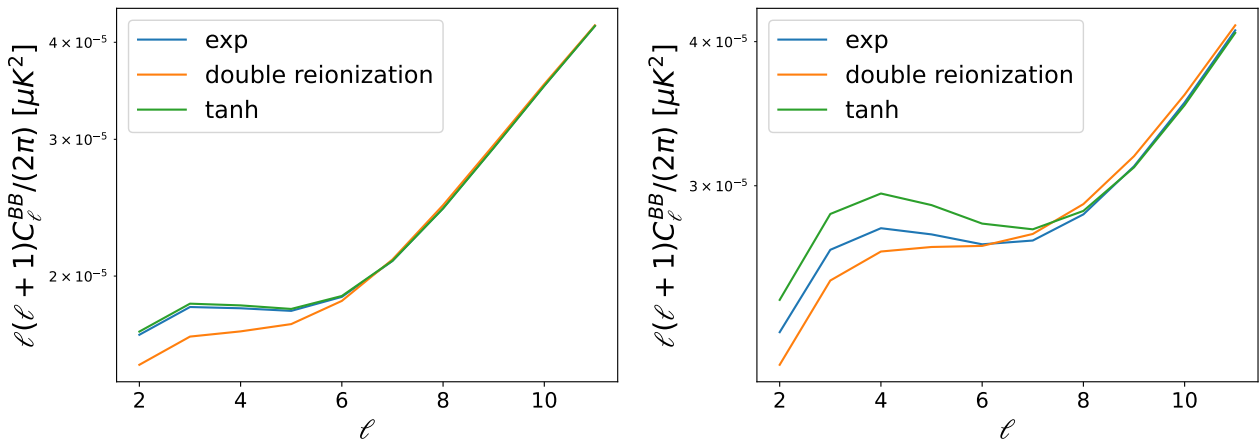


Figure 5.9: The very large-scale power spectra for $\tau = 0.054$ (left) and $\tau = 0.08$ (right) for $r = 0.001$.

Appendix A

Full power spectra analysis results

We include figures not shown in the main text here.

A.1 The exponential model

The posterior distribution for $\tau = 0.08$ and $r = 0.001$ is shown in Fig. A.1. EE and BB power spectra are shown in Fig. A.2.

A.2 The double reionization model

The posterior distributions for $\tau = 0.08, r = 0.01$, $\tau = 0.054, r = 0.001$, $\tau = 0.08, r = 0.001$ are shown in Fig. A.4, Fig. A.3, and Fig. A.5, respectively. EE and BB power spectra with $\tau = 0.054$ and $r = 0.001$ are shown in Fig. A.6 and with $\tau = 0.08$ are shown in Fig. A.7.

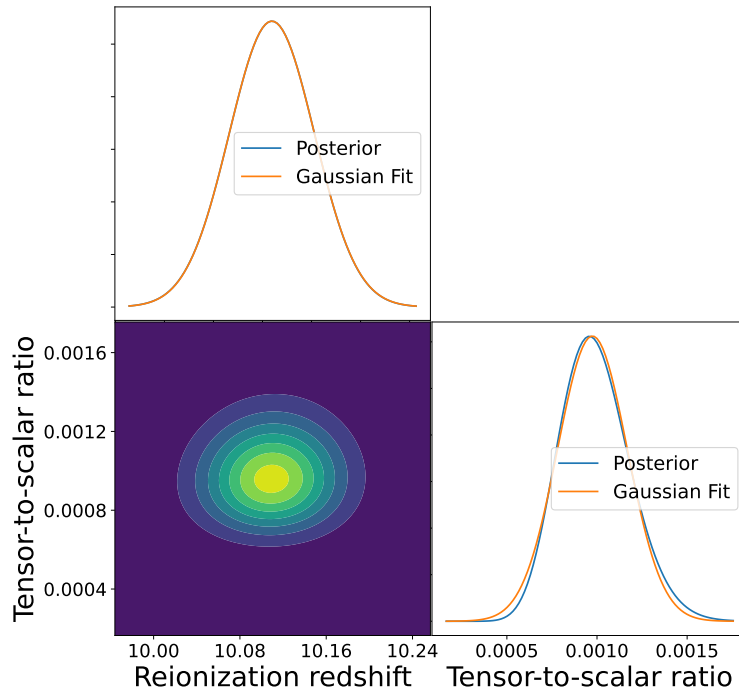


Figure A.1: Same as Fig. 4.1 but with $r = 0.001$ and $\tau = 0.08$.

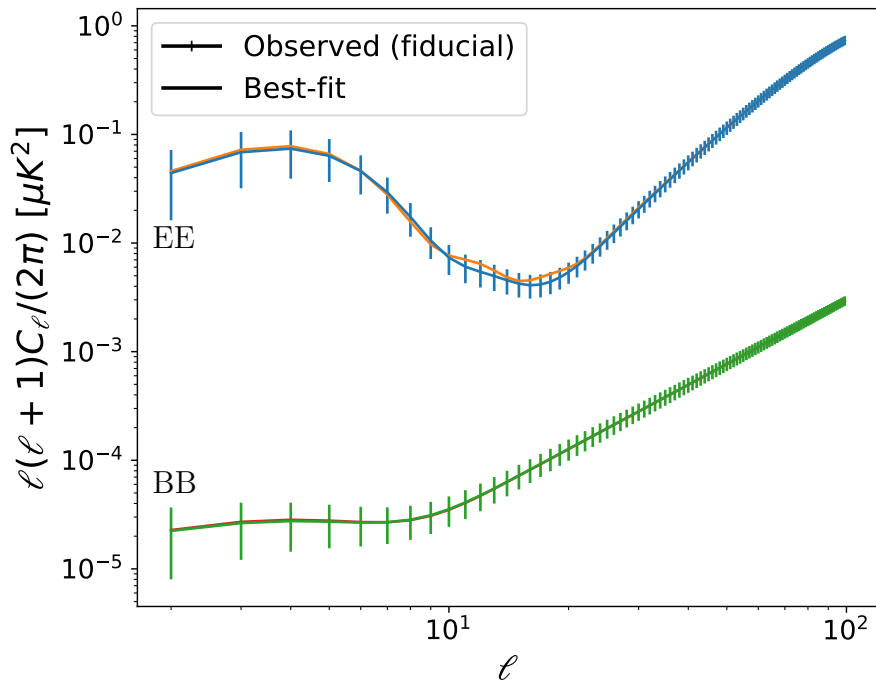
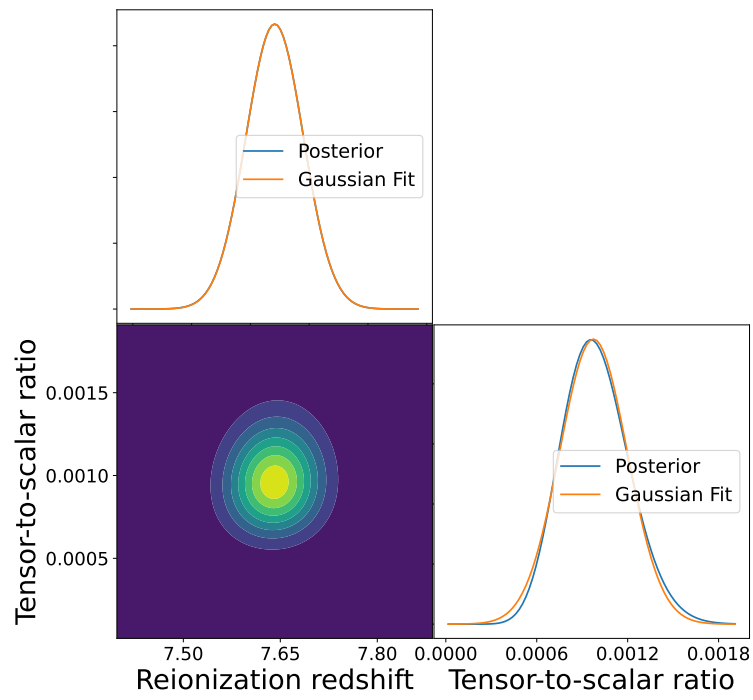
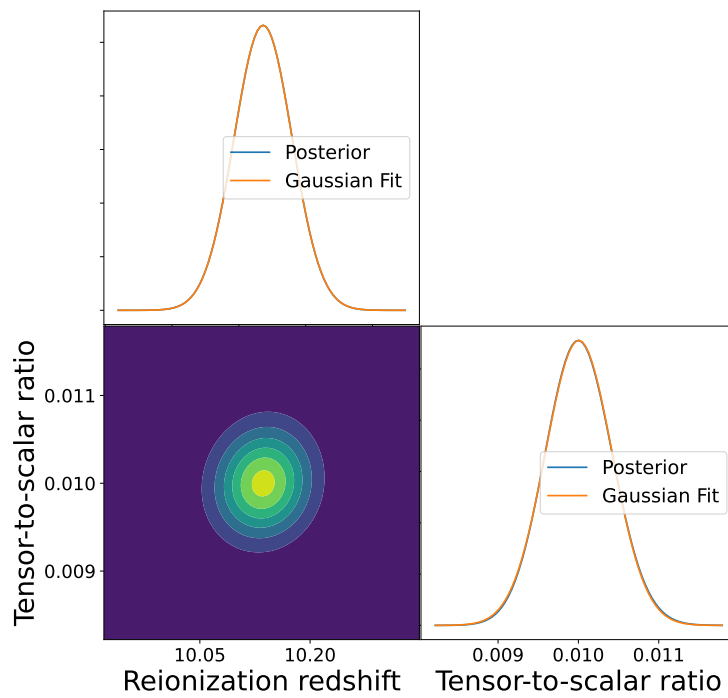


Figure A.2: Same as Fig. 4.6 but with $r = 0.001$.

Figure A.3: Same as Fig. 4.7 but with $r = 0.001$.Figure A.4: Same as Fig. 4.7 but with $\tau = 0.08$.

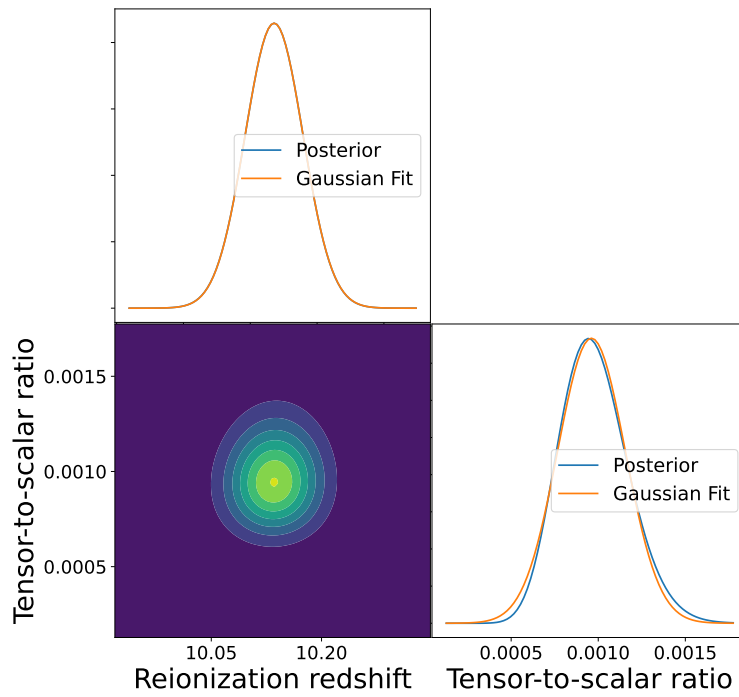


Figure A.5: Same as Fig. 4.7 but with $r = 0.001$ and $\tau = 0.08$.

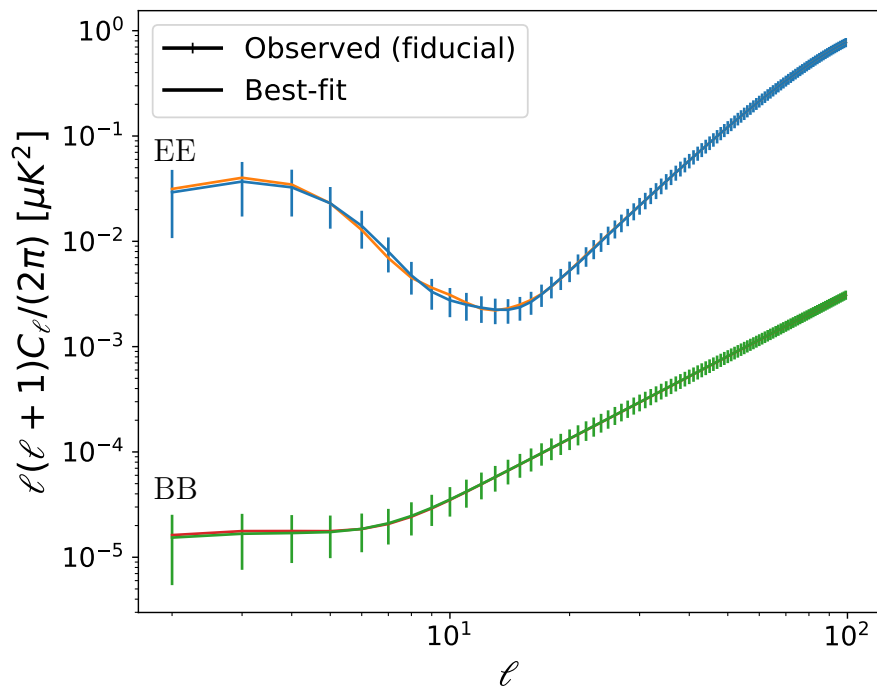
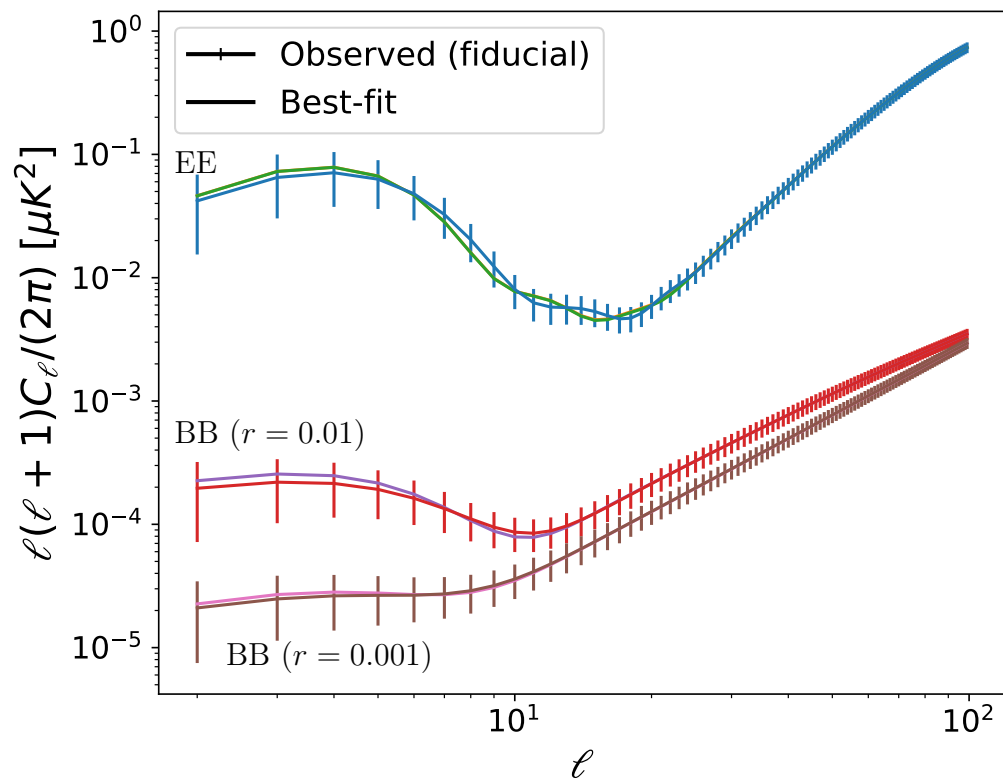


Figure A.6: Same as Fig. 4.9 but with $r = 0.001$.

Figure A.7: Same as Fig. 4.9 but with $\tau = 0.08$.

Appendix B

Large-scale power spectra analysis results

We include figures not shown in the main text here.

B.1 The exponential model

For the results only using large-scale power spectra ($\ell < 10$), we show the posterior distributions for $\tau = 0.08, r = 0.01$, $\tau = 0.054, r = 0.001$, $\tau = 0.08, r = 0.001$ in Fig. B.2, Fig. B.1, and Fig. B.3, respectively. EE and BB power spectra for $r = 0.001$ are shown in Fig. B.4, and $\tau = 0.08$ are shown in Fig. B.5.

B.2 The double reionization model

For the results only cutting the small-scale BB power spectrum but keeping the full EE power spectrum, we show the posterior distributions for $\tau = 0.08, r = 0.01$, $\tau = 0.054, r = 0.001$, $\tau = 0.08, r = 0.001$ in Fig. B.7, Fig. B.6, and Fig. B.8, respectively. EE and BB power spectra for $r = 0.001$ are shown in Fig. B.9, and for $\tau = 0.08$ are shown in Fig. B.10.

For the results only using large-scale power spectra ($\ell < 10$), we show the posterior distributions for $\tau = 0.08, r = 0.01$, $\tau = 0.054, r = 0.001$, $\tau = 0.08, r = 0.001$ in Fig. B.12, Fig. B.11, and Fig. B.13, respectively. EE and BB power spectra for $r = 0.001$ are shown in Fig. B.14, and for $\tau = 0.08$ are shown in Fig. B.15.

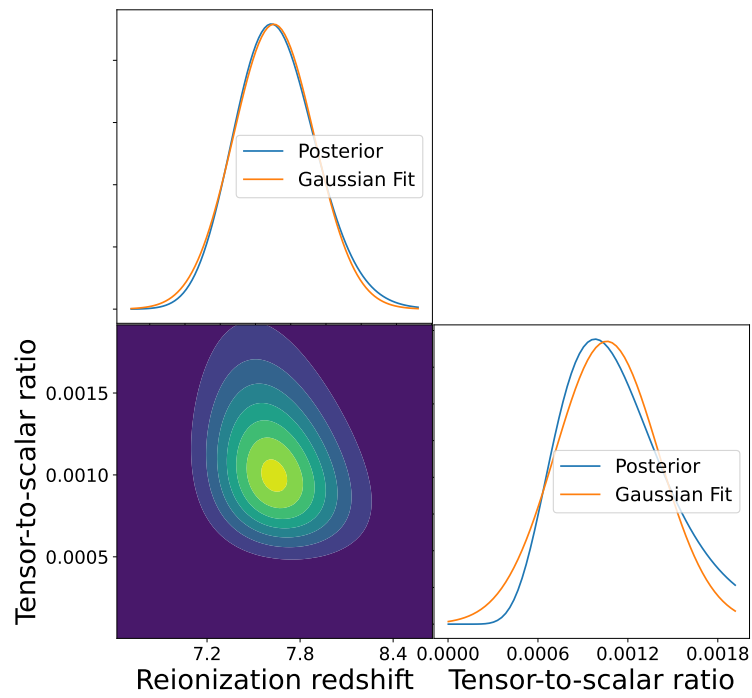


Figure B.1: Same as Fig. 5.1 but with $r = 0.001$.

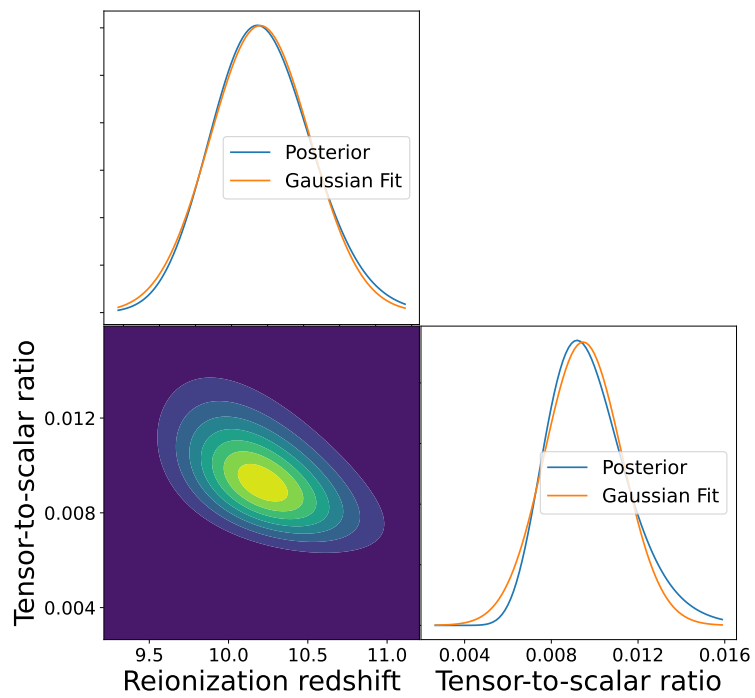


Figure B.2: Same as Fig. 5.1 but with $\tau = 0.08$.

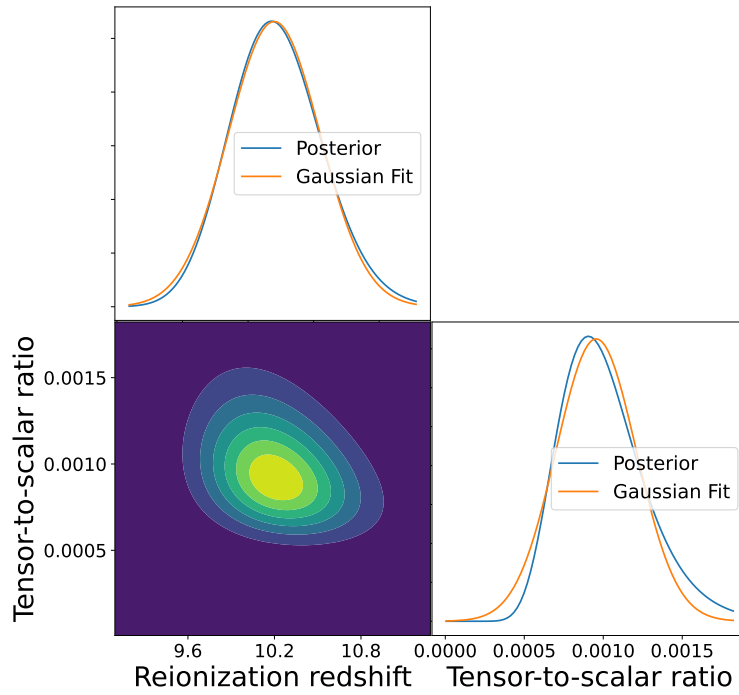


Figure B.3: Same as Fig. 5.1 but with $r = 0.001$ and $\tau = 0.08$.

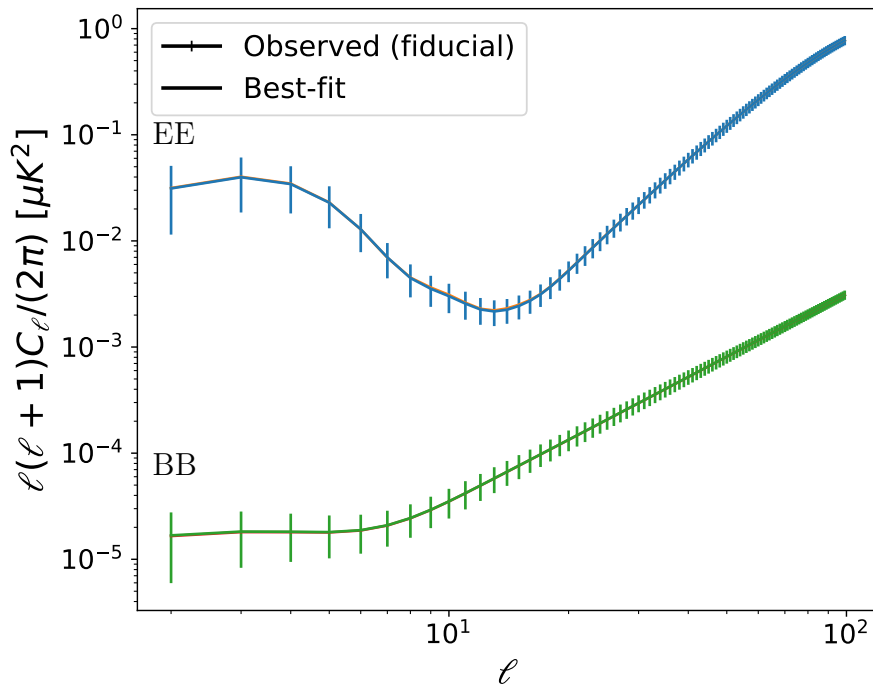


Figure B.4: Same as Fig. 5.2 but with $r = 0.001$.

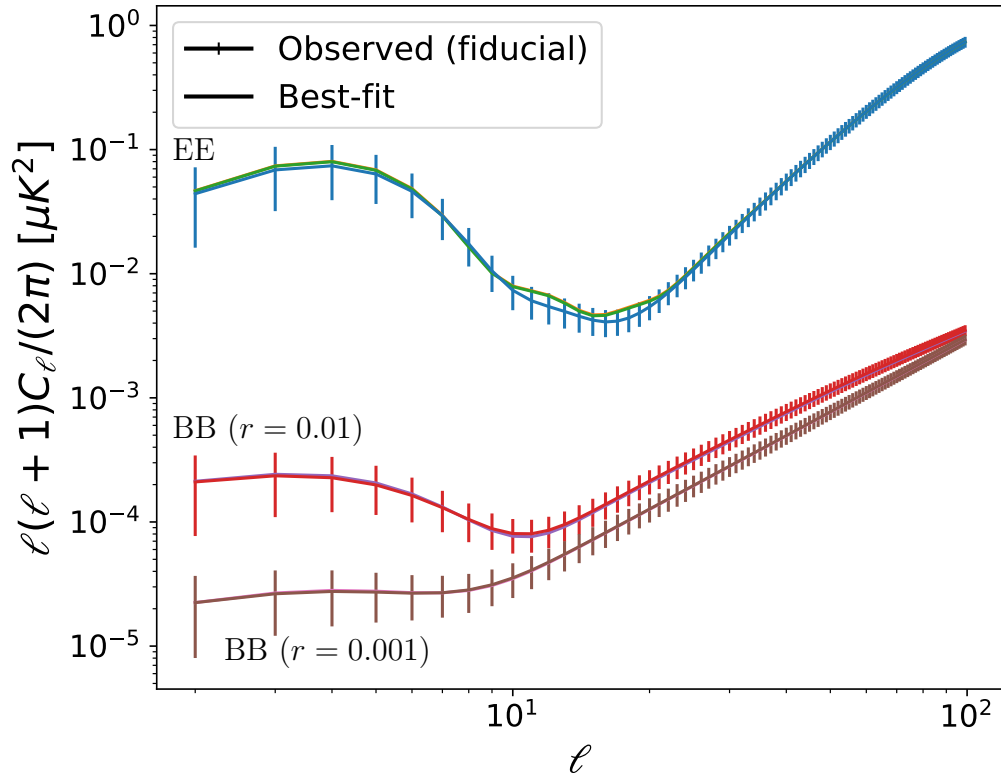


Figure B.5: Same as Fig. 4.5 but with $\tau = 0.08$ and only using very large scales ($\ell < 10$).

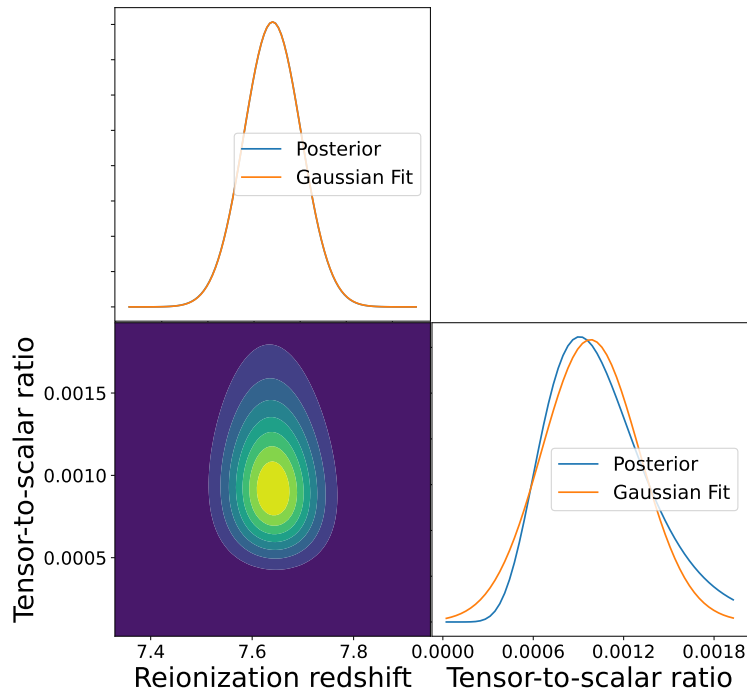
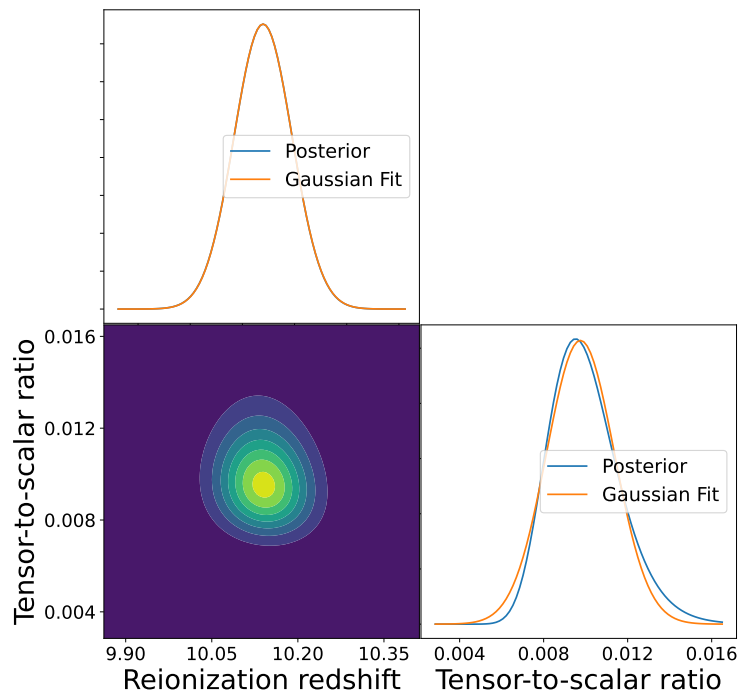
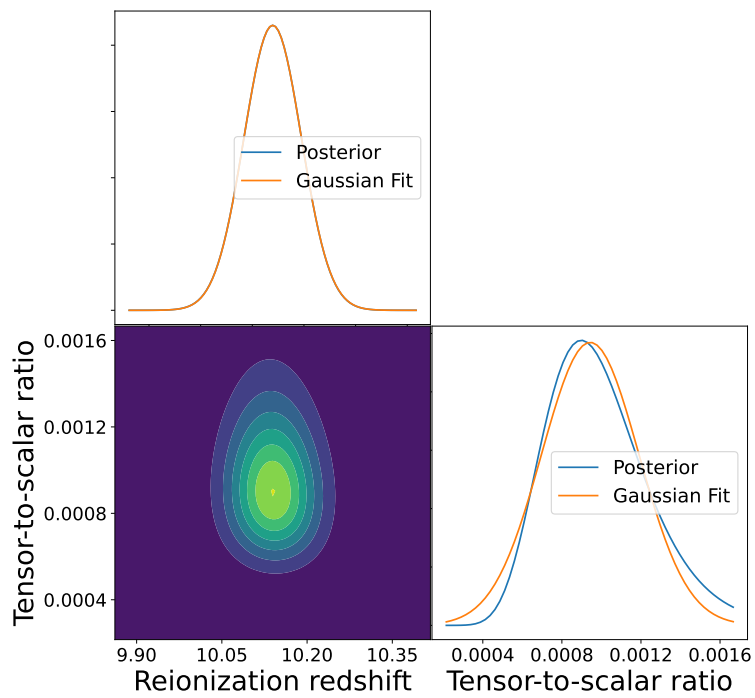


Figure B.6: Same as Fig. 5.3 but with $r = 0.001$.

Figure B.7: Same as Fig. 5.3 but with $\tau = 0.08$.Figure B.8: Same as Fig. 5.3 but with $r = 0.001$ and $\tau = 0.08$.

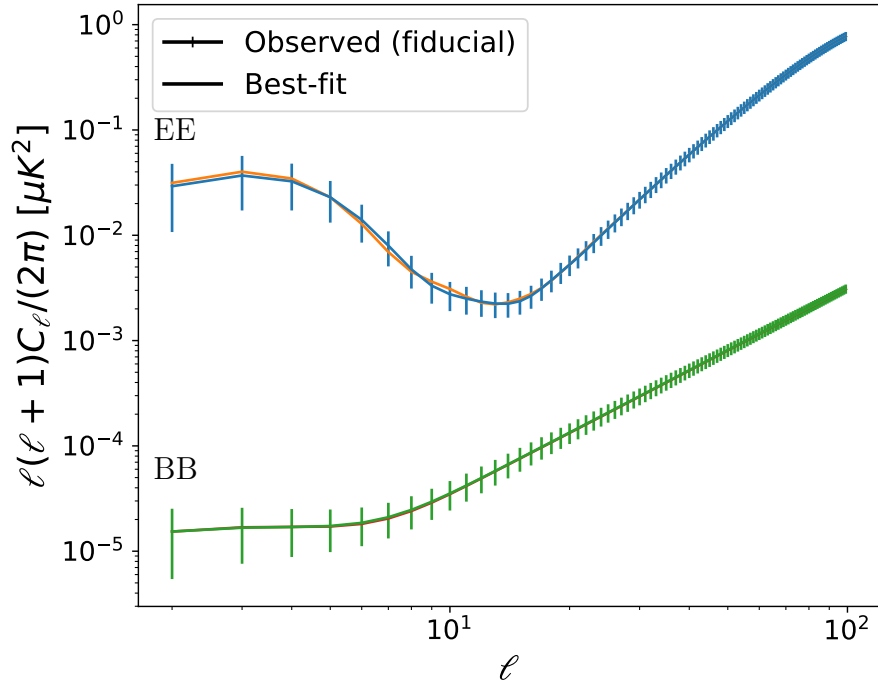


Figure B.9: Same as Fig. 5.5 but with $r = 0.001$.

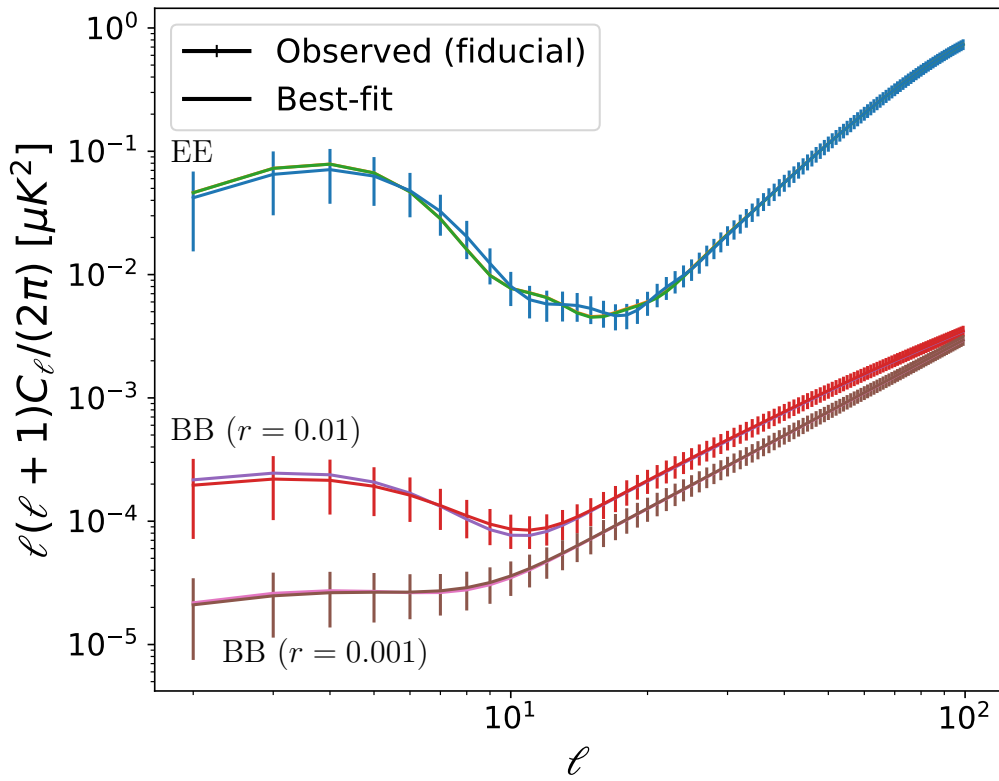
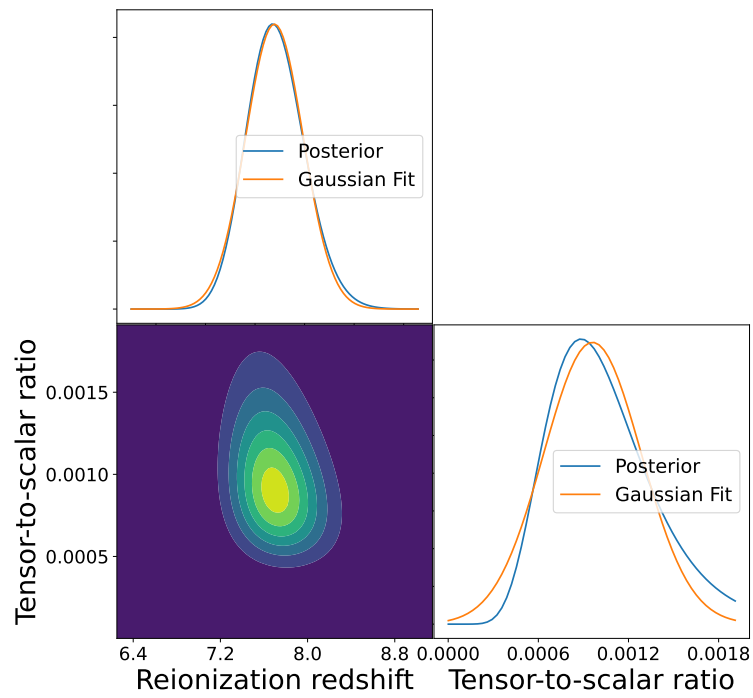
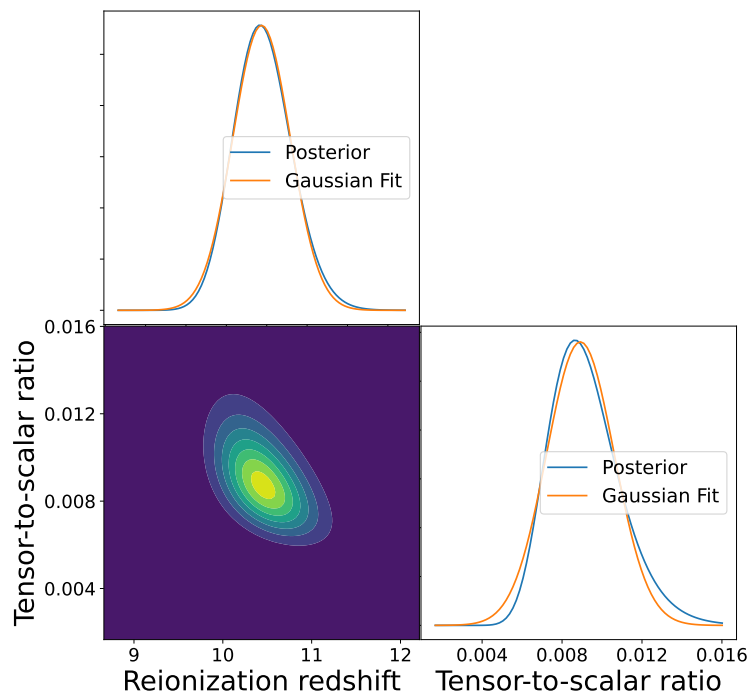


Figure B.10: Same as Fig. 5.5 but with $\tau = 0.08$.

Figure B.11: Same as Fig. 5.4 but with $r = 0.001$.Figure B.12: Same as Fig. 5.4 but with $\tau = 0.08$.

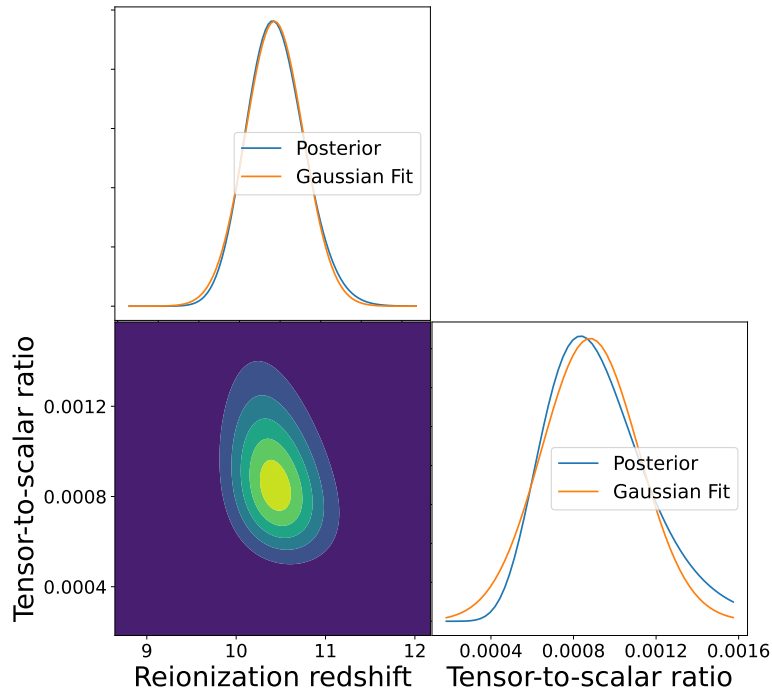


Figure B.13: Same as Fig. 5.4 but with $r = 0.001$ and $\tau = 0.08$.

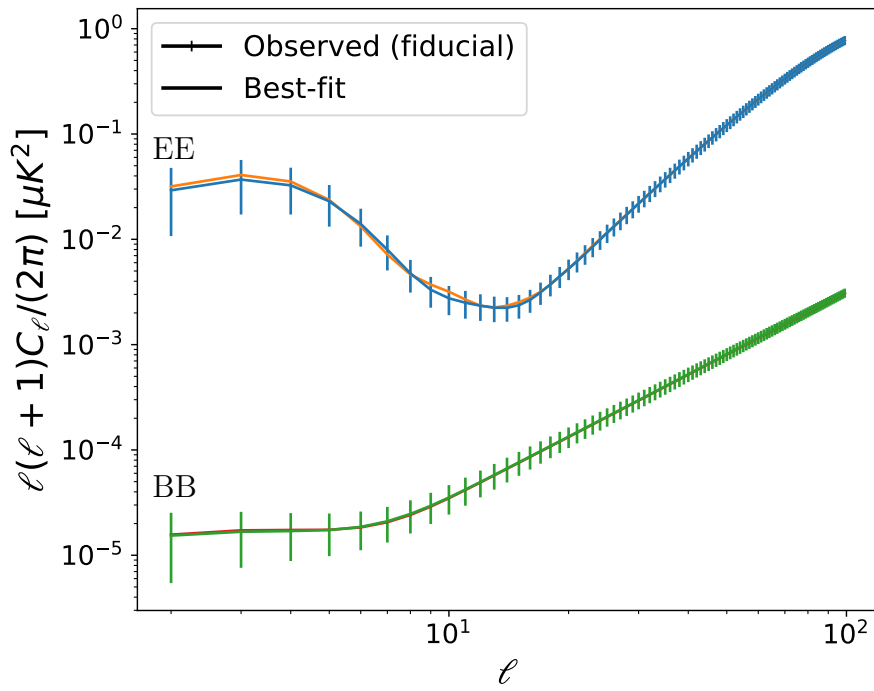


Figure B.14: Same as Fig. 5.6 but with $r = 0.001$.

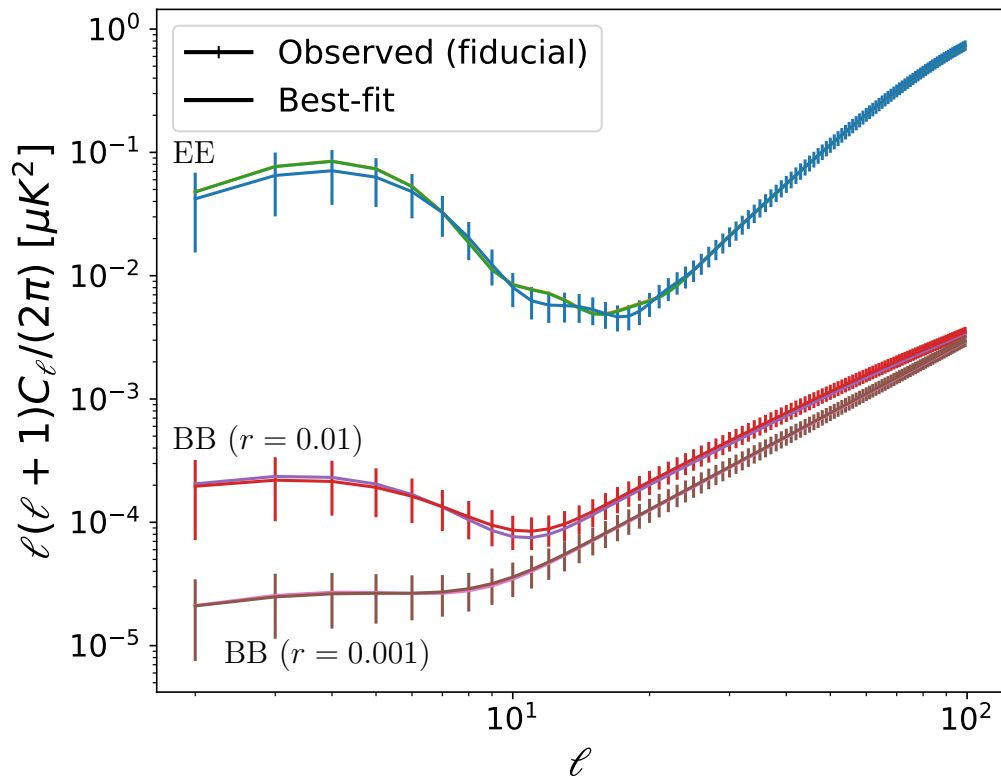


Figure B.15: Same as Fig. 5.6 but with $\tau = 0.08$.

Appendix C

Summary of random x_e models

We summarize random x_e models we generate for this thesis. There are 20 models for $\tau = 0.054$ and 20 models for $\tau = 0.08$. x_e is shown in Fig. C.1 and power spectra are shown in Fig. C.2.

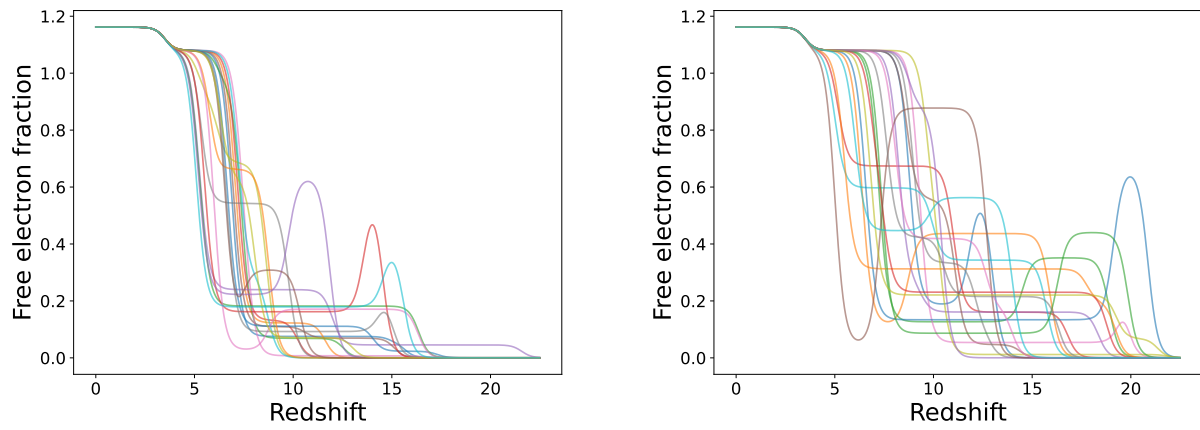
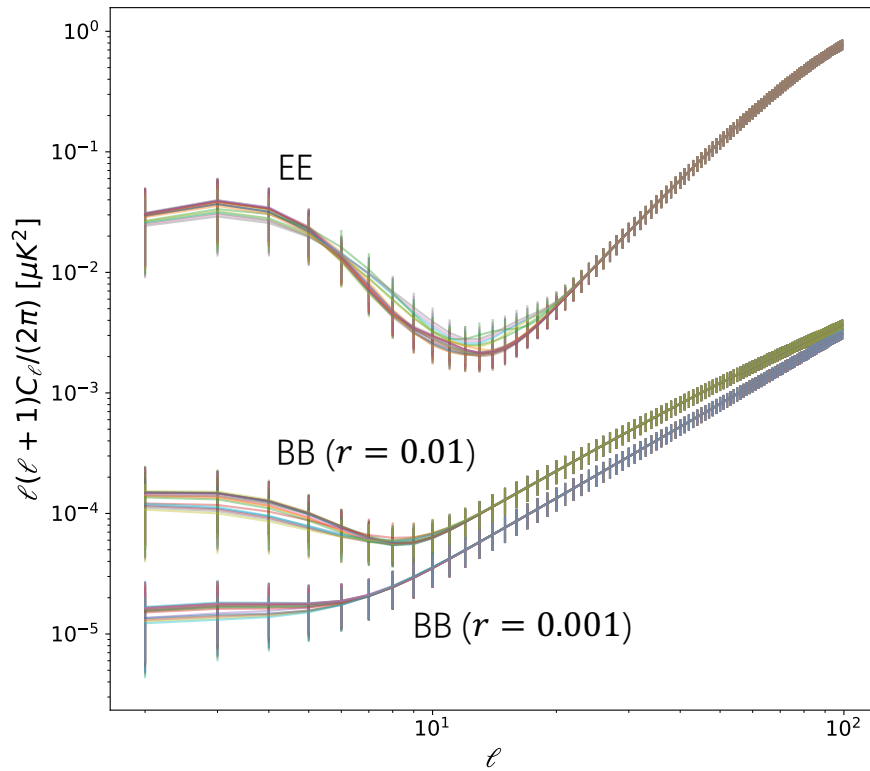
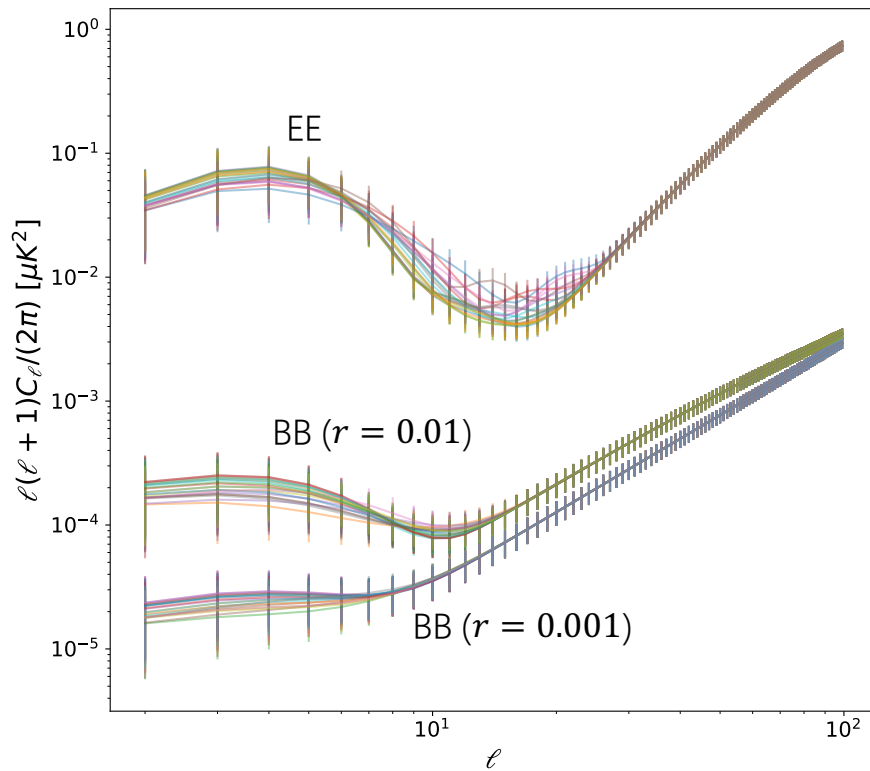


Figure C.1: The free electron fraction x_e for random x_e models with $\tau = 0.054$ (left) and $\tau = 0.08$ (right).



(a) EE and BB power spectra with $\tau = 0.054$ for random x_e models.



(b) EE and BB power spectra with $\tau = 0.08$ for random x_e models.

Figure C.2: EE and BB power spectra with $\tau = 0.054$ (top) and $\tau = 0.08$ (bottom) for random x_e model.

Bibliography

- Abazajian, K., Addison, G., Adshead, P., et al. 2019, arXiv preprint arXiv:1907.04473
- Abbott, L. F., & Wise, M. B. 1984, Nuclear physics B, 244, 541
- Achúcarro, A., Biagetti, M., Braglia, M., et al. 2022, arXiv preprint arXiv:2203.08128
- Adachi, S., Faúndez, M. A., Arnold, K., et al. 2020, The Astrophysical Journal, 897, 55
- Adam, R., Aghanim, N., Ashdown, M., et al. 2016, Astronomy & Astrophysics, 596, A108
- Ade, P., Aguilar, M., Akiba, Y., et al. 2017, The Astrophysical Journal, 848, 121
- Ade, P. A., Aghanim, N., Arnaud, M., et al. 2016, Astronomy & Astrophysics, 594, A13
- Ade, P. A., Ahmed, Z., Amiri, M., et al. 2021, Physical review letters, 127, 151301
- Ade, P. A., Amiri, M., Benton, S., et al. 2022, The Astrophysical Journal, 927, 174
- Aghanim, N., Akrami, Y., Ashdown, M., et al. 2020a, Astronomy & Astrophysics, 641, A6
- Aghanim, N., et al. 2020b, Astron. Astrophys., 641, A6,
- Alam, S., Ata, M., Bailey, S., et al. 2017, Monthly Notices of the Royal Astronomical Society, 470, 2617
- Albrecht, A., & Steinhardt, P. J. 1982, Physical Review Letters, 48, 1220
- Araujo, D., Bischoff, C., Brizius, A., et al. 2012, The Astrophysical Journal, 760, 145
- Bardeen, J. M., Steinhardt, P. J., & Turner, M. S. 1983, Physical Review D, 28, 679
- Barkana, R., & Loeb, A. 2001, Physics reports, 349, 125
- Barkats, D., Aikin, R., Bischoff, C., et al. 2014, The Astrophysical Journal, 783, 67
- Baumann, D. 2022, Cosmology (Cambridge University Press)
- Bennett, C., Hill, R. S., Hinshaw, G., et al. 2003, The Astrophysical Journal Supplement Series, 148, 97
- Bennett, C. L., Larson, D., Weiland, J. L., et al. 2013, The Astrophysical Journal Supplement Series, 208, 20
- Bischoff, C., Hyatt, L., McMahon, J., et al. 2008, The Astrophysical Journal, 684, 771

- Blas, D., Lesgourgues, J., & Tram, T. 2011, *Journal of Cosmology and Astroparticle Physics*, 2011, 034
- Bond, J. R., & Efstathiou, G. 1984, *Astrophysical Journal*, Part 2-Letters to the Editor (ISSN 0004-637X), vol. 285, Oct. 15, 1984, p. L45-L48. Research supported by the Science and Engineering Research Council of England and NASA., 285, L45
- Bosman, S. E., Davies, F. B., Becker, G. D., et al. 2022, *Monthly Notices of the Royal Astronomical Society*, 514, 55
- Brout, R., Englert, F., & Gunzig, E. 1978, *Annals of Physics*, 115, 78
- Brown, M., Ade, P., Bock, J., et al. 2009, *The Astrophysical Journal*, 705, 978
- Bruton, S., Scarlata, C., Haardt, F., et al. 2023, *The Astrophysical Journal*, 953, 29
- Bullock, J. S., & Boylan-Kolchin, M. 2017, *Annual Review of Astronomy and Astrophysics*, 55, 343
- Campeti, P., Komatsu, E., Baccigalupi, C., et al. 2024, *Journal of Cosmology and Astroparticle Physics*, 2024, 008
- Carones, A., Migliaccio, M., Puglisi, G., et al. 2023, *Monthly Notices of the Royal Astronomical Society*, 525, 3117
- Carroll, S. M. 2001, *Living reviews in relativity*, 4, 1
- Carron, J. 2019, *Physical Review D*, 99, 043518
- Cen, R. 2003, *The Astrophysical Journal*, 591, 12
- Choi, S. K., Hasselfield, M., Ho, S.-P. P., et al. 2020, *Journal of Cosmology and Astroparticle Physics*, 2020, 045
- Crittenden, R., Bond, J. R., Davis, R. L., Efstathiou, G., & Steinhardt, P. J. 1993, *Physical Review Letters*, 71, 324
- Curtis-Lake, E., Carniani, S., Cameron, A., et al. 2023, *Nature Astronomy*, 7, 622
- Davies, F. B., Hennawi, J. F., Bañados, E., et al. 2018, *The Astrophysical Journal*, 864, 142
- Davis, R. L., Hodges, H. M., Smoot, G. F., Steinhardt, P. J., & Turner, M. S. 1992, *Physical Review Letters*, 69, 1856
- Delabrouille, J., Cardoso, J.-F., Le Jeune, M., et al. 2009, *Astronomy & Astrophysics*, 493, 835
- Dimastrogiovanni, E., Fasiello, M., & Fujita, T. 2017, *Journal of Cosmology and Astroparticle Physics*, 2017, 019
- Dodelson, S., & Schmidt, F. 2020, *Modern cosmology* (Academic press)
- Efstathiou, G. 1988
- Eisenstein, D. J., Zehavi, I., Hogg, D. W., et al. 2005, *The Astrophysical Journal*, 633, 560

- Eriksen, H., Jewell, J., Dickinson, C., et al. 2008, *The Astrophysical Journal*, 676, 10
- Fabbri, R., & Pollock, M. 1983, *Physics Letters B*, 125, 445
- Fan, X., Carilli, C., & Keating, B. 2006a, *Annu. Rev. Astron. Astrophys.*, 44, 415
- Fan, X., Strauss, M. A., Richards, G. T., et al. 2006b, *The Astronomical Journal*, 131, 1203
- Finkelstein, S. L., D'Aloisio, A., Paardekooper, J.-P., et al. 2019, *The Astrophysical Journal*, 879, 36
- Fukugita, M. 2003, *Monthly Notices of the Royal Astronomical Society*, 343, L25
- Gaikwad, P., Haehnelt, M. G., Davies, F. B., et al. 2023, *Monthly Notices of the Royal Astronomical Society*, 525, 4093
- Giare', W., Di Valentino, E., & Melchiorri, A. 2024, *Physical Review D*, 109, 103519
- Goto, H., Shimasaku, K., Yamanaka, S., et al. 2021, *The Astrophysical Journal*, 923, 229
- Greig, B., Mesinger, A., & Bañados, E. 2019, *Monthly Notices of the Royal Astronomical Society*, 484, 5094
- Gunn, J. E., & Peterson, B. A. 1965, *Astrophysical Journal*, vol. 142, p. 1633-1636, 142, 1633
- Guo, H., Zheng, Z., Behroozi, P. S., et al. 2016, *Monthly Notices of the Royal Astronomical Society*, 459, 3040
- Guth, A. H. 1981, *Physical Review D*, 23, 347
- Guth, A. H., & Pi, S.-Y. 1982, *Physical Review Letters*, 49, 1110
- Hawking, S. W. 1982, *Physics Letters B*, 115, 295
- Hoag, A., Bradač, M., Huang, K., et al. 2019, *The Astrophysical Journal*, 878, 12
- Hsiao, T. Y.-Y., Coe, D., Larson, R. L., et al. 2023, arXiv preprint arXiv:2305.03042
- Hu, W., & Dodelson, S. 2002, *Annual Review of Astronomy and Astrophysics*, 40, 171
- Hu, W., & White, M. 1997, *Physical Review D*, 56, 596
- Inoue, A. K., Hasegawa, K., Ishiyama, T., et al. 2018, *Publications of the Astronomical Society of Japan*, 70, 55
- Ishigaki, M., Kawamata, R., Ouchi, M., et al. 2018, *The Astrophysical Journal*, 854, 73
- Jin, X., Yang, J., Fan, X., et al. 2023, *The Astrophysical Journal*, 942, 59
- Jung, I., Finkelstein, S. L., Dickinson, M., et al. 2020, *The Astrophysical Journal*, 904, 144
- Kamionkowski, M., Kosowsky, A., & Stebbins, A. 1997a, *Physical Review Letters*, 78, 2058
- . 1997b, *Physical Review D*, 55, 7368
- Kamionkowski, M., & Kovetz, E. D. 2016, *Annual Review of Astronomy and Astrophysics*, 54, 227

- Karkare, K. S. 2019, *Physical Review D*, 100, 043529
- Katayama, N., & Komatsu, E. 2011, *The Astrophysical Journal*, 737, 78
- Kazanas, D. 1980, *Astrophysical Journal*, Part 2-Letters to the Editor, vol. 241, Oct. 15, 1980, p. L59-L63., 241, L59
- Komatsu, E. 2022, *Nature Reviews Physics*, 4, 452
- Komatsu, E., Smith, K. M., Dunkley, J., et al. 2011, *The Astrophysical Journal Supplement Series*, 192,
- Konno, A., Ouchi, M., Ono, Y., et al. 2014, *The Astrophysical Journal*, 797, 16
- Kusaka, A., Appel, J., Essinger-Hileman, T., et al. 2018, *Journal of Cosmology and Astroparticle Physics*, 2018, 005
- Leitch, E. M., Kovac, J., Halverson, N., et al. 2005, *The Astrophysical Journal*, 624, 10
- Lewis, A., Challinor, A., & Lasenby, A. 2000, *The Astrophysical Journal*, 538, 473
- Lin, Y.-T., & Wandelt, B. D. 2006, *Astroparticle Physics*, 25, 151
- Linde, A. D. 1982a, *Physics Letters B*, 108, 389
- . 1982b, *Physics Letters B*, 116, 335
- LiteBIRD Collaboration, Allys, E., Arnold, K., et al. 2023, *Progress of Theoretical and Experimental Physics*, 2023, 042F01
- Lizancos, A. B., Challinor, A., & Carron, J. 2021, *Journal of Cosmology and Astroparticle Physics*, 2021, 016
- Lyth, D. H., & Liddle, A. R. 2009, *The primordial density perturbation: Cosmology, inflation and the origin of structure* (Cambridge university press)
- Ma, C.-P., & Bertschinger, E. 1995, arXiv preprint astro-ph/9506072
- Maleknejad, A., & Sheikh-Jabbari, M. 2011, *Physical Review D—Particles, Fields, Gravitation, and Cosmology*, 84, 043515
- . 2013, *Physics Letters B*, 723, 224
- Mason, C. A., Fontana, A., Treu, T., et al. 2019, *Monthly Notices of the Royal Astronomical Society*, 485, 3947
- McGreer, I. D., Mesinger, A., & D’Odorico, V. 2015, *Monthly Notices of the Royal Astronomical Society*, 447, 499
- Montroy, T. E., Ade, P. A., Bock, J. J., et al. 2006, *The Astrophysical Journal*, 647, 813
- Morales, A. M., Mason, C. A., Bruton, S., et al. 2021, *The Astrophysical Journal*, 919, 120
- Morishita, T., Roberts-Borsani, G., Treu, T., et al. 2023, *The Astrophysical Journal Letters*, 947, L24

- Mukhanov, V. F., & Chibisov, G. 1981, *ZhETF Pisma Redaktsiiu*, 33, 549
- Naidu, R. P., Tacchella, S., Mason, C. A., et al. 2020, *The Astrophysical Journal*, 892, 109
- Nakane, M., Ouchi, M., Nakajima, K., et al. 2024, *The Astrophysical Journal*, 967, 28
- Namikawa, T., Saito, S., & Taruya, A. 2010, *Journal of Cosmology and Astroparticle Physics*, 2010, 027
- Namikawa, T., Baleato Lizancos, A., Robertson, N., et al. 2022, *Physical Review D*, 105, 023511
- Ning, Y., Jiang, L., Zheng, Z.-Y., & Wu, J. 2022, *The Astrophysical Journal*, 926, 230
- Ouchi, M., Ono, Y., & Shibuya, T. 2020, *Annual Review of Astronomy and Astrophysics*, 58, 617
- Ouchi, M., Shimasaku, K., Furusawa, H., et al. 2010, *The Astrophysical Journal*, 723, 869
- Ouchi, M., Harikane, Y., Shibuya, T., et al. 2018, *Publications of the Astronomical Society of Japan*, 70, S13
- Peebles, P. 1984, This page is intentionally left blank, 84
- Peebles, P. J. E., & Ratra, B. 2003, *Reviews of modern physics*, 75, 559
- Perivolaropoulos, L., & Skara, F. 2022, *New Astronomy Reviews*, 95, 101659
- Perlmutter, S., Aldering, G., Goldhaber, G., et al. 1999, *The Astrophysical Journal*, 517, 565
- Polnarev, A. 1985, *Soviet Astronomy*, vol. 29, Nov.-Dec. 1985, p. 607-613. Translation *Astronomicheskii Zhurnal*, vol. 62, Nov.-Dec. 1985, p. 1041-1052, 29, 607
- Riess, A. G., Casertano, S., Yuan, W., et al. 2021, *The Astrophysical Journal Letters*, 908, L6
- Riess, A. G., Filippenko, A. V., Challis, P., et al. 1998, *The astronomical journal*, 116, 1009
- Rubakov, V., Sazhin, M. V., & Veryaskin, A. 1982, *Physics Letters B*, 115, 189
- Sato, K. 1981, *Monthly Notices of the Royal Astronomical Society*, 195, 467
- Sayre, J., Reichardt, C., Henning, J., et al. 2020, *Physical Review D*, 101, 122003
- Schroeder, J., Mesinger, A., & Haiman, Z. 2013, *Monthly Notices of the Royal Astronomical Society*, 428, 3058
- Schutz, B. 2022, *A first course in general relativity* (Cambridge university press)
- Seljak, U. 1997, *The Astrophysical Journal*, 482, 6
- Seljak, U., & Zaldarriaga, M. 1997, *Physical Review Letters*, 78, 2054
- Sherwin, B. D., & Schmittfull, M. 2015, *Physical Review D*, 92, 043005
- Sievers, J. L., Achermann, C., Bond, J., et al. 2007, *The Astrophysical Journal*, 660, 976
- Sigurdson, K., & Cooray, A. 2005, *Physical review letters*, 95, 211303

- Simard, G., Hanson, D., & Holder, G. 2015, *The Astrophysical Journal*, 807, 166
- Smith, K. M., Hanson, D., LoVerde, M., Hirata, C. M., & Zahn, O. 2012, *Journal of Cosmology and Astroparticle Physics*, 2012, 014
- Starobinskii, A. 1979, *JETP Letters*, 30, 682
- Starobinsky, A. A. 1980, *Physics Letters B*, 91, 99
- . 1982, *Physics Letters B*, 117, 175
- Stompór, R., Leach, S., Stivoli, F., & Baccigalupi, C. 2009, *Monthly Notices of the Royal Astronomical Society*, 392, 216
- Sunyaev, R., & Zeldovich, Y. B. 1980, *Monthly Notices of the Royal Astronomical Society*, vol. 190, Feb. 1980, p. 413-420., 190, 413
- Tegmark, M., de Oliveira-Costa, A., & Hamilton, A. J. 2003, *Physical Review D*, 68, 123523
- Totani, T., Kawai, N., Kosugi, G., et al. 2006, *Publications of the Astronomical Society of Japan*, 58, 485
- Totani, T., Aoki, K., Hattori, T., et al. 2014, *Publications of the Astronomical Society of Japan*, 66, 63
- Tristram, M., Banday, A. J., Górski, K. M., et al. 2021, *Astronomy & Astrophysics*, 647, A128
- Tristram, M., Banday, A. J., Douspis, M., et al. 2024, *Astronomy & Astrophysics*, 682, A37
- Umeda, H., Ouchi, M., Nakajima, K., et al. 2023, arXiv preprint arXiv:2306.00487
- Wang, F., Davies, F. B., Yang, J., et al. 2020, *The Astrophysical Journal*, 896, 23
- Weinberg, D. H., Mortonson, M. J., Eisenstein, D. J., et al. 2013, *Physics reports*, 530, 87
- Whitler, L. R., Mason, C. A., Ren, K., et al. 2020, *Monthly Notices of the Royal Astronomical Society*, 495, 3602
- Zaldarriaga, M. 1997, *Physical Review D*, 55, 1822
- Zaldarriaga, M., & Seljak, U. 1997, *Physical Review D*, 55, 1830
- Zhu, Y., Becker, G. D., Bosman, S. E., et al. 2022, *The Astrophysical Journal*, 932, 76